INELASTIC ANALYSIS OF BRICK MASONRY:

MESO/MACRO-SCALE APPROACH

INELASTIC ANALYSIS OF BRICK MASONRY: MESO/MACRO-SCALE APPROACH

By

BABAK SHIEH-BEYGI, B.Eng., M.Sc.

A Thesis

Submitted to the School of Graduate Studies

in Partial Fulfillment of the Requirements

for the Degree

Doctor of Philosophy

McMaster University

DOCTOR OF PHILOSOPHY (2007) **McMaster University**

(Engineering) **Hamilton, Ontario**

TITLE: **Inelastic Analysis of Brick Masonry: Meso/Macro-scale Approach**

AUTHOR: **Babak Shieh-Beygi**

B.Eng. (Sharif University of Technology, Tehran, Iran)

M.Sc. (Sharif University of Technology, Tehran, Iran)

SUPERVISOR: **Professor S. Pietruszczak**

NUMBER OF PAGES: **xv, 127**

ABSTRACT

This thesis is focused on modeling of progressive failure in brick masonry structures. Two distinct strategies are examined, namely meso-modeling and macro-modeling approach.

In the first part, an advanced constitutive model capable of addressing both pre and post-localization behavior is developed and implemented in a commercial finite element package. A mesoscopic modeling approach is then adopted, in which the structural behavior is examined at the level of constituents, i.e. brick and mortar. The performance of the model is verified by simulating a series of experimental tests reported in the literature. Those include the tests conducted by van der Pluijm (1993), Atkinson et al. (1989), and Page (1983).

Later, an alternative approach is developed, based on theory of homogenization, in which a lower bound assessment is employed to predict the directional strength characteristics of the brick masonry. The performance of the model is verified using numerical homogenization which involves a finite element analysis of a periodic unit cell. For both these approaches, the failure envelopes for brick masonry at different orientations of the bed joints are obtained.

Finally, a methodology is proposed for a systematic identification of material parameters of a macroscopic failure criterion describing the anisotropic strength characteristics of the brick masonry. This criterion is formulated in the framework of Critical Plane Approach (CPA) and its performance is verified against the experimental data of Page (1981 and 1983).

ACKNOWLEDGEMENTS

I would like to express my sincere and deep appreciation to my supervisor, Professor Stan Pietruszczak, for his excellent guidance, patience, encouragement and support throughout every stage of this work. I would also like to thank Dr. Peijun Guo, Dr. Ahmed Ghobarah and Dr. Mateusz Sklad for their support, valuable comments and feedbacks.

I would like to gratefully acknowledge the financial support from my supervisor, Professor Pietruszczak. Also, the financial assistance of the Department of Civil Engineering and the School of Graduate Studies at McMaster University is deeply appreciated.

I owe a great debt of gratitude to my beloved wife, Yalda. I am deeply grateful for her patience, sacrifice, understanding, encouragement, and for her continuing love and support, without which the completion of this work was impossible. She is, without a doubt, my greatest source of inspiration. Also, I would like to extend my deep appreciation towards my mother-in-law and father-in-law, Rita and Asghar, for their patience, understanding and encouragement. My thanks also go to my only brother, Siamak, who has always been a great source of joy. Finally, I am greatly indebted to my

dear mother and father, Maliheh and Ali, who have always provided me with endless love and support. Without their devotion and sacrifice, I would have never reached this stage in life.

TABLE OF CONTENTS

LIST OF FIGURES

FIGURE

LIST OF TABLES

TABLE

CHAPTER 1

INTRODUCTION

1.1. General Remarks

Masonry has been a primary building material for centuries, the reason being two-fold. Not only is it extremely durable, but it has a distinct appearance. From an engineering perspective, the latter is in fact a disadvantage as the microstructure of typical masonry is difficult to handle. The complex arrangement of masonry units, bed and head joints leads to complex failure mechanisms and a strong anisotropic response on the macroscale. The latter point has held engineers back from using it efficiently in the design process. However, in the last few decades the progress in the area of mechanics of composites and the advent of powerful computers have meant that a lot of effort is now focused on developing a better understanding of the complex behavior of this material. As a result, new methodologies have emerged for efficient and reliable analysis and design procedures, and it is now feasible to more confidently use this material as the main load-bearing component of a structure.

In the realm of numerical modeling of masonry structures, the research is focused mainly on two distinct approaches: mesomodels and macromodels. Mesomodels, also called detailed models or micromodels, can be used to study the interaction of the constituents and the damage propagation pattern under different loading histories. This type of analysis gives the most detailed information about the behavior and response of masonry structures, and is considered to be the ideal approach as a result. However, given the enormity of the generated models emerging in real engineering applications, it is not feasible to implement this approach for real masonry structures. This problem can be addressed using a macro modeling approach, in which the constituents are smeared out within a representative element using homogenization techniques. The equivalent mechanical properties are then established and are explicitly employed in the course of numerical analysis. A major problem with this approach, however, is the identification of material parameters incorporated in this type of description. The latter usually requires a large number of specially designed experiments, which can be quite expensive and are often subject to strong influence of boundary conditions, so that the scatter in data can be significant. In this study, a mesomodeling approach is invoked as an alternative to the experimental procedure. The information extracted from the analysis at the mesoscale is used to identify the material parameters embedded within a macroscopic framework.

1.2. LITERATURE REVIEW

Over the last few decades the engineering analysis of masonry structures has become the main focus of many research programs, leading to a significantly better understanding of the complex behavior of this composite material. This has enabled engineers to devise more rational methods for practical analysis and design. Numerical analysis of masonry using finite elements method, specifically with the advent of powerful computers, has provided the analysts with an inexpensive and reliable tool.

The research on masonry has been mainly focused on two distinct aspects: experimental investigation and numerical modeling. The experimental study of the behavior of brickwork involves mainly the tests performed at the material level, i.e. brick and mortar, as well as those conducted to derive the anisotropic strength characteristics of the brickwork. The former has been pursued by different researchers, including van der Pluijm (1993), who carried out a series of 54 displacement-controlled tests to study the response of the bed joints in a shear test setup. In fact, these tests are one of the most comprehensive studies conducted on the shear behavior of the brick masonry to date. In the experiments, the response of brick masonry under shear displacement loading at different confining pressures was examined with the emphasis on mode II fracture. A similar testing program had been conducted earlier by van der Pluijm (1992) to establish the tensile behavior of small masonry specimens, involving the mode I fracture energy. The latter tests were undertaken to address the tensile behavior of the brick and mortar interface. A number of other investigators conducted extensive experimental tests to establish an appropriate failure criterion for the masonry constituents. For instance, based on a series of tri-axial tests, Bierwirth et al. (1993) found that unlike the nonlinear envelope observed for concrete, the failure surface for mortar had just a subtle curvature. Consequently, the authors concluded that it could be safely approximated with a linear curve, i.e. Mohr-Coulomb criterion. Atkinson et al. (1985) made the same conclusion for the failure envelope of different types of mortar and accordingly fitted a linear surface to their experimental results. As for the bricks, however, they conducted a series of biaxial tests and proposed a polynomial failure surface in tension-compression regime. Their study did not include any failure modes in compression-compression domain. Later, Atkinson et al. (1989) performed a series of tests to study the behavior of a simple brickwork under cyclic loadings. The tests were conducted on a panel constructed of two courses of bricks, reflecting mainly the shear characteristics of the interface rather than the brickwork. They also identified the basic strength characteristics of the brick units and mortar in a series of direct tension and compression tests, while also conducting a series of couplet tests to identify the shear characteristics of the interface.

On the macroscopic level, Samarasinghe and Hendry (1982) tested a series of one-sixth scale brickwork panels, measuring 150mm (height) × 150mm (width) × 18mm (thickness), under uniform biaxial tension-compression. They proposed an equation for the failure surface as a function of the principal stresses and the angle of the inclination of the bed joints. Their work was followed by the study of Page (1983), in which a series of biaxial tension-compression tests were performed to obtain a three dimensional failure envelope for the brick masonry as a function of the same parameters as mentioned before. In an earlier report, Page (1981) had presented the results of a similar study on the biaxial compression-compression response of the brick masonry. Due to the relatively small size of the panels, the tests conducted by both Page and Samarasinghe suffered from the influence of boundary conditions. Based on the Page experiments, Dhanasekar et al. (1985) introduced an alternative representation of the macroscopic failure surface in terms of three alternative parameters, i.e. normal stress, lateral stress, and the shear stress along the bed joints. This study did not shed any light though on the inherent restrictions of the tests, i.e. the size effect and the lack of information with regards to the out-of-plane behavior. Binda et al. (1988) carried out a series of deformation controlled tests on 600mm × 500mm × 250mm masonry prisms, built up with nine courses of 250mm × 120mm × 55 mm solid brick units and 10 mm thick mortar joints. Three different types of mortar were used, and for each one a total of three prisms were tested under uniaxial compressive loading. The complete stress-strain diagrams, including the softening regime, were captured. Although these experiments addressed, to some extent, the size effect limitations encountered in previous studies, they did not provide any insight into the directional strength characteristics of brick masonry. A similar study to that of Page on the directional characteristics of the grouted concrete masonry was conducted by Drysdale and Khattab (1995). It involved a series of biaxial tension-compression tests. The results clearly showed the sensitivity of the failure modes, the strength parameters and the deformation characteristics to the orientation of the bed joints and the principal stress ratio. The specimens were built using full-size hollow concrete blocks. The experimental data obtained from this study provided valuable information which was later used to establish empirical or semi-empirical methodologies for the design of grouted concrete masonry structures. For brick masonry, however, the Page studies seem to provide the most comprehensive data on the in-plane behavior to date.

Another aspect of the masonry research is the numerical modeling. Ideally, the analysis of masonry structures should be conducted at the meso-level and should incorporate the properties of the constituents, e.g. brick and mortar, as well as the details of the architectural arrangement. In this approach, both brick and mortar are discretized separately, and both are described by a different constitutive model. In order to avoid numerical instability, the mesh size for the masonry units should be of the same order as that for the mortar elements (c.f. Zucchini and Lourenço, 2002). As a consequence, the implementation of this approach leads to extremely large numerical models and therefore is not suitable for real engineering applications. This so-called mesoscopic approach is particularly fitting for studying the interaction of different constituents as well as investigating the damage propagation at the constituents' level. This approach can also be implemented to assess the average mechanical properties of masonry, which can later be used in the formulation of macromodels (e.g. Riddington and Gambo, 1991; Anthoine, 1995 and 1997; Zucchini and Lourenço, 2002; Massart et al., 2005).

For most loading histories, the cracks initiate in the joints while the blocks remain intact. Considering this fact, another approach can be introduced in which the masonry units are discretized with continuum elements, whereas the joints are modeled by interface elements. In this approach, joints are usually considered as weakness planes, while blocks are modeled as a set of elastic units. Page (1978) was one of the first to introduce such an approximation. His finite element model was constructed using isotropic, elastic 2D elements for bricks and linkage elements with a brittle response in tension regime accompanied by a bi-linear failure locus for compressive normal stresses ($\tau - \sigma$ space). Lourenço and Rots (1993) employed a similar technique, wherein again the interface elements were used as potential crack paths. In this approach bricks were modeled with continuum elements, while the mortar joints and the potential crack lines inside the units were modeled with zero-thickness interface elements. The main problem with this approach, however, is that it cannot predict more complicated failure modes resulting from the interaction of the brick and mortar due to the fact that the Poisson effect of the mortar is ignored. To obtain a more accurate model, the failure criterion adopted for the joint interface should also be capable of capturing the compressive failure mode of the brick masonry (Lourenço et al., 1994; Lourenço and Rots, 1997). In their refined model, Lourenço and coauthors adopted a constitutive relation for the interface elements that was capable of capturing major failure mechanisms, i.e. tensile cracking associated with Rankine's cut-off for mode I failure, slipping represented by Coulomb friction envelope for mode II failure and crushing mode represented by a cap model for compressive failure. As before, the possibility of tensile fracture along the bricks was accounted for by introducing a vertical interface element in the middle of the bricks.

The model described above was later extended by Oliveira and Lourenço (2001) to deal with cyclic loading. Gambarotta and Lagomarsino (1997) adopted a similar modeling strategy to study the in-plane response of rectangular shear walls subjected to horizontal cyclic loading. Bricks were modeled using four-node isoparametric elements with an elastic-plastic formulation, while mortar joints were represented by interface elements. The concept of damage mechanics was implemented to capture both mode I and mode II fracture mechanisms in the joints. To capture the possible tensile failure of the bricks, a brittle vertical interface was introduced in the middle of each brick unit.

The main limitation of the approach outlined above, as well as other similar methodologies, is the fact that the interaction of the joints with the brick units cannot be properly captured. In fact, due to the noticeable differences between the mechanical properties of bricks and mortar joints, significant lateral stresses will develop in the regions adjacent to the joints, which cannot be described in this formulation. This approach has also difficulties in capturing the out-of-plane effects, which can be of great importance in biaxial compressive loading. Moreover, the size of the generated models for real masonry structures is still extremely large, so that this methodology cannot be considered as a pragmatic approach for real engineering applications.

The analysis of large masonry structures should best be conducted at a macro-level. In this case, the masonry can be described as a continuum whose average properties are identified at the level of constituents taking into account their geometric arrangement. Over the last decade, a number of different approximations have been developed for assessing the homogenized properties of structural masonry. These mainly include the micropolar Cosserat continuum models and theory of homogenization for periodic media.

In micropolar Cosserat continuum approach (e.g. Sulem and Muhlhaus, 1997; Masiani and Trovalusci, 1996), the Cosserat theory of elasticity or micropolar elasticity is employed. In this theory, the translation based equations of traditional elasticity are enriched by incorporating additional equations related to the rotation at each point. As a consequence, couple stress components (torque per unit area) are added to the stress tensor which becomes non-symmetric. In view of this, some additional material parameters appear in the constitutive relation, which is believed to provide a more accurate representation of the material behavior. However, developing a systematic methodology towards the identification of equivalent continuum properties in this approach cannot be easily achieved. Consequently, there have been virtually no attempts to solve practical engineering problems using this methodology.

In recent years the application of theory of homogenization for periodic media in assessing the equivalent properties of brick masonry has been the subject of extensive research. Given the complexity of the problem as well as restrictions imposed by inelastic behavior of constituents, several simplified methodologies have been developed incorporating various explicit kinematic/static constraints. Relying upon these simplifying assumptions, some authors such as Maier et al. (1991) and Pietruszczak and Niu (1992) derived simplified nonlinear constitutive laws for the homogenized material. Pietruszczak and Niu introduced a two-step homogenization approach, in which the bed and head joints were introduced in two successive steps. Pande et al. (1989) derived the equivalent elastic properties of brick masonry in terms of the elastic properties of brick and mortar by introducing a stacked brick-mortar system consisting of a set of parallel layers which behaved elastically. This approach was then extended so that masonry consisting of two sets of bed and head joints could be represented by an equivalent homogeneous orthotropic elastic material.

Even though these methods present an attractive and rather simple methodology for the homogenization process, a more accurate representation may be obtained using numerical homogenization. One of the most rigorous homogenization procedures has been that introduced by Anthoine (1995, 1997), where the global elastic properties of masonry were obtained as a function of elastic properties of both constituents (brick and mortar) as well as the finite thickness of the joints. Here, the solution for the unit cell was obtained numerically using the finite element technique. In a similar attempt, Piszczek et al. (2001) used a 3D numerical homogenization approach to identify the equivalent elastic parameters of homogenized brick masonry. Furthermore, Ma et al. (2001) employed the same strategy to calculate the equivalent elastic constants and failure modes of brick masonry. In their simulations, three distinct failure modes, namely tensile failure, shear failure and compressive failure were considered for the units, whereas the mortar joints were modeled by a Mohr-Coulomb criterion intercepted by Rankine's cut-off in tension regime.

Even though the former methodologies prove to be very useful in the analysis of masonry structures, they are not, in general, applicable in the context of inelastic analysis. The extension to elastoplastic regime can be only achieved by introducing suitably defined macroscopic yield/failure surfaces. For instance, Alpa and Monetto (1994) presented a comprehensive formulation for the constitutive behavior of in-plane loaded dry block masonry walls, with special attention to failure analysis. Also, De Buhan & de Felice (1997) proposed a theoretical framework in the context of a continuum model for assessing the ultimate failure of brick masonry. It was based on the yield design homogenization method which had been developed earlier for the reinforced soils (de Buhan & Salençon, 1990), fiber composite materials (de Buhan and Taliercio, 1991) and jointed rock masses (Bekaert and Maghous, 1996), and had been implemented by de Felice (1994) for the treatment of block masonry.

Other applications of homogenization theory for estimating the conditions at failure as well as macroscopic properties include the works of Luciano & Sacco (1997, 1998), Cluni & Gusella (2003). While the former deals with periodic microstructures, the latter is concerned with non-periodic masonry works.

Finally, significant work has also been undertaken with regards to the development of phenomenologicaly-based macroscopic failure criteria for structural masonry. Examples include the studies of Andreaus (1996), Zhuge et al. (1998), Lourenço et al. (1998), Raffard et al. (2001) and Ushaksaraei and Pietruszczak (2002).

Raffard et al. (2001) used a numerical homogenization approach to derive the anisotropic characteristics of a homogenized stone masonry. In their model, an anisotropic macroscopic failure criterion was assumed for the homogenized media in terms of a modified Drucker-Prager constitutive law. The failure criterion was defined as a function of a generalized deviatoric stress in such a way as to account for the material anisotropy. The results of a tri-axial test for different orientations of bed joints were used in accordance with a curve-fitting procedure to identify the material parameters. However, this model is not suitable, in general, for assessing the failure load of engineering structures, because the adopted approach does not include any information on failure in tension regime.

Ushaksaraei and Pietruszczak (2002) implemented the concept of Critical Plane Approach (Pietruszczak and Mróz, 2001) to formulate an anisotropic failure criterion for brick masonry. This approach involves the notion of a critical (or localization) plane along which the failure function, expressed in terms of normal and tangential components of the traction vector, becomes maximum. A generalized Mohr-Coulomb criterion with the Rankine's cut-off was employed, in which the inherent anisotropy was described by introducing a set of orientation dependent material parameters (Pietruszczak and Mróz, 2000 and 2001). Later, this macroscopic failure criterion was implemented in the context of non-linear FE analysis (Gocevski et al., 2002; Pietruszczak and Ushaksaraei, 2003) to model a brick masonry wall subjected to static as well as seismic loading conditions.

Finally, another innovative approach is the implementation of intelligent constitutive models based on the idea of artificial neural networks. Here, the constitutive model is developed as an independent module trained using the available experimental data and then implemented in a finite element analysis (cf. Shin and Pande, 2001). Although this approach presents an interesting alternative to the conventional formulation, it is still in the early stages of development and has not been applied yet to any large-scale practical problem.

1.3. OUTLINE OF THE RESEARCH

Based on the comments above, it is evident that there is still a need for developing a simple and reliable methodology for assessing the macroscopic properties of brick masonry. This is the primary objective here. In this work, an advanced constitutive model is presented first which is capable of describing three distinct deformation stages in the response of brickwork constituents, i.e. elastic, strain-hardening and strain-softening. This model is subsequently implemented in the context of a user-defined constitutive module, and linked with COSMOS 2.7 Finite Element package. The existing experimental data on the strength characteristics of brick masonry is used for the purpose of verification, and subsequently the model is implemented to study the in-plane behavior of brick masonry panels using a discrete approach. Later, a homogenization scheme is proposed to obtain the average macroscopic, orientation-dependent strength characteristics of brick masonry. The analysis is conducted using two different approaches, a lower bound assessment and numerical homogenization. Following the analysis, a methodology is proposed to identify the material parameters appearing in macroscopic failure criteria. The proposed methodology is verified using the available experimental data.

1.4. ORGANIZATION OF THESIS

The thesis consists of two main parts. The first deals with the mesomodeling approach and its application in studying the behavior of brick masonry panels under different loading histories. Specifically, in Chapter 2 an advanced constitutive model for the brick masonry constituents is introduced. A series of parametric studies are then conducted to assess the reliability and sensitivity of the developed model to different parameters. Later, the proposed model is applied in Chapter 3 to simulate a number of experimental tests available in literature using a meso-scale approach. These include the tests conducted by van der Pluijm (1993), Atkinson et al. (1989), and Page (1983). For the Page's experiments, a full-scale analysis is carried out and the directional characteristics of brick masonry are obtained and compared with the experimental data. Two different loading configurations, namely uniaxial tension and biaxial tension-compression are considered. Chapter 4 is devoted to a continuum approach based on the theory of homogenization for periodic media. Here, a methodology is proposed to obtain a lower bound assessment for the average directional strength characteristics of brick masonry under various loading conditions using a limit state analysis.

The second part is focused on the macro-level approach. Here, a methodology is proposed for identification of material parameters of a macroscopic failure criterion based on the Critical Plane Approach. The experimental data of Page (1981, 1983) is used for the purpose of identification and verification of the performance of this framework.

CHAPTER 2

A MATERIAL MODEL FOR THE CONSTITUENTS OF MASONRY

2.1. INTRODUCTION

A realistic solution to problems involving mechanical response of masonry structures depends to a large extent, on the choice of the adopted constitutive model. In this chapter a material model is proposed which is capable of describing the behavior of brick masonry constituents, i.e. brick and mortar, under different stages of deformation. All three distinctive phases in the material response; namely elastic, elastoplastic and brittle/softening, are invoked in the formulation. The onset of elastoplastic response is defined by introducing the notion of the yield surface, whereas the conditions at failure are described by postulating the existence of a path-independent failure locus. The onset of failure is associated with the formation of macrocrack, the orientation of which is defined based upon the inherent characteristics of the governing failure surface. Implementing a simple homogenization scheme, the influence of macrocrack is smeared out over the Representative Elementary Volume and, as a consequence, the equivalent macroscopic response is defined. The proposed model is then implemented within

COSMOS 2.7 Finite Element package via a user defined constitutive module. Later, an extensive numerical analysis is carried out aimed at the verification of the proposed approach.

2.2. FORMULATION

(i) Pre-Localization Response

The behavior of the masonry constituents prior to cracking is modeled within the context of a rate-independent plasticity, in which the functional form of the yield and failure loci is postulated a priori. In the plasticity framework employed, two distinct loci consistent with Rankine's cut-off and the Mohr-Coulomb criteria are considered to define the elastic domain. Loading/unloading conditions are accounted for using standard Kuhn-Tucker constraints. Upon the inception of yielding, the tangential elastoplastic operator is evaluated using the additivity postulate. A non-associated flow rule is implemented to account for the transition from compaction to dilatancy prior to failure.

Failure Surface

Based on the experimental evidence (cf. Atkinson et al., 1985; Bierwirth et al., 1993), a Mohr-Coulomb criterion with Rankine's cut-off is assumed to govern the conditions at failure for both brick and mortar. Mohr-Coulomb is a generalization of Tresca criterion, and is used for pressure sensitive materials. A graphical representation of this criterion, as developed by Mohr (1900), is a straight line tangential to the largest Mohr circle. In principal stress space, the failure surface represents an irregular hexagonal prism. The Rankine's cut-off criterion postulates that, in the tension regime, the failure takes place as soon as the maximum principle stress exceeds the tensile strength of the material. The abovementioned criteria can be expressed in terms of principle stresses as

$$F_1 = \sigma_1 - \sigma_0 = 0; \quad F_2 = \sigma_1 - \left(\frac{1-\sin\phi}{1+\sin\phi}\right)\sigma_3 - \left(\frac{2c\cos\phi}{1+\sin\phi}\right) = 0 \tag{2.1}$$

Here, σ_1 and σ_3 represent the maximum and minimum principal stress, respectively, whereas σ_0 is the tensile strength of the material. Furthermore, ϕ is referred to as the angle of internal friction, and c denotes the cohesion, i.e. the shear resistance of the material at zero normal stress. A graphical presentation of Equations (2.1) is depicted in Figure 2.1. For the mortar, a tri-linear failure surface is employed to account for the presence of weaker mortar-brick interface (Figure 2.2). Note that this is a simplification introduced in order to avoid the need for employing the interface elements in the context of finite element analysis.

For the numerical implementation, it is convenient to write the criterion in terms of stress invariants. Here, the following set of invariants is employed (after Nayak, 1972)

$$\sigma_m = I_1/3;\ \bar{\sigma} = \sqrt{J_2};\ \theta = \frac{1}{3}\sin^{-1}\left(\frac{-3\sqrt{3}}{2}\frac{J_3}{\bar{\sigma}^3}\right),\ -\frac{\pi}{6} \le \theta \le \frac{\pi}{6} \tag{2.2}$$

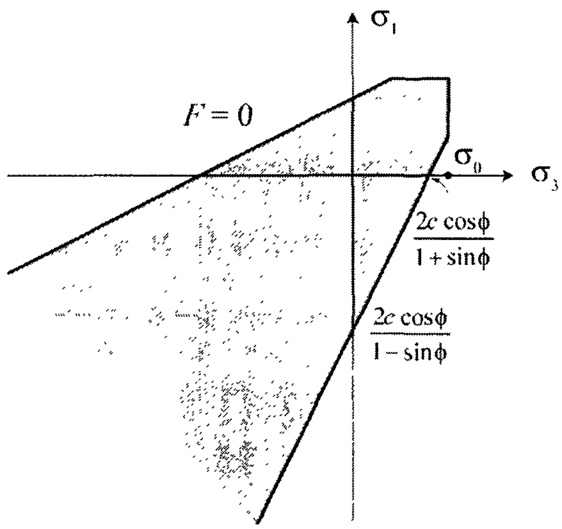

Figure 2.1 – Failure surface in principal stress space

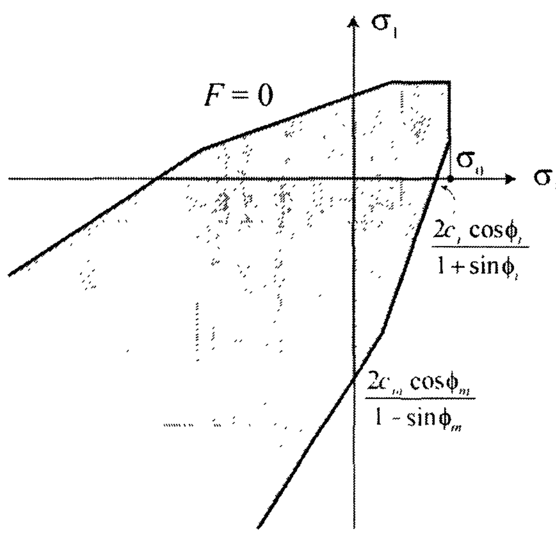

Figure 2.2 – Tri-linear failure surface used for brick-mortar interface

In the above equations, I_1 stands for the first stress invariant, while J_2 and J_3 represent the second and third invariant of the deviatoric part of the stress tensor, respectively. Furthermore, σ_m is the average confining pressure, $\bar{\sigma}$ is a measure of the deviatoric stress and θ is the so-called Lode angle. Using the above definitions, both failure criteria, Equation (2.1), can be expressed in terms of invariants as

$$F_1 = \frac{\bar{\sigma}}{g_1(\theta)} + \sqrt{3}(\sigma_m - \sigma_0) = 0; \qquad F_2 = \frac{\bar{\sigma}}{g_2(\theta)} + \eta_f \sigma_m - \mu = 0 \tag{2.3}$$

where

$$g_1(\theta) = \frac{1}{2\sin(\theta + 2\pi/3)} \tag{2.4}$$

and

$$\eta_f = \frac{2\sqrt{3}\sin\phi}{3-\sin\phi}; \; \mu = \frac{2\sqrt{3}c\cos\phi}{3-\sin\phi}; \; g_2(\theta) = \frac{3-\sin\phi}{2\sqrt{3}\cos\theta - 2\sin\theta\sin\phi} \tag{2.5}$$

In these equations, $g(\theta)$ determines the shape of the deviatoric section, also known as the π plane - section. For a Mohr-Coulomb criterion, for example, it can be shown that the deviatoric section is an irregular hexagon (Figure 2.3). The criteria (2.3) are schematically illustrated in $\bar{\sigma}/g(\theta) - \sigma_m$ space in Figure 2.4.

Yield Surface

The material response is assumed to be ductile-brittle for compressive stress trajectories, while in the tension regime, an elastic-brittle characteristic is employed. As a result, in tension domain the yield and failure surfaces coincide with each other. However, in compression regime a distinct yield surface is introduced a priori. The latter is a function of a damage parameter which is identified with the accumulated plastic distortion. This internal parameter ensures the gradual migration of the yield surface towards the failure locus. Thus,

$$f_1 = F_1; \qquad f_2 = \frac{\bar{\sigma}}{g(\theta)} + \eta(\xi)\sigma_m - \mu = 0 \tag{2.6}$$

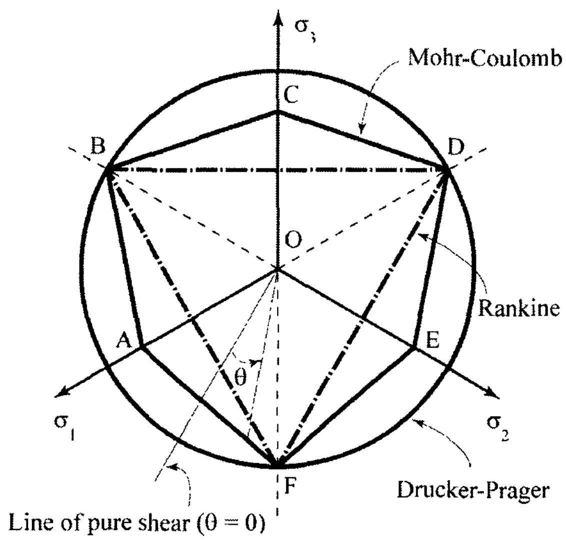

Figure 2.3 – Deviatoric section, Mohr-Coulomb criterion

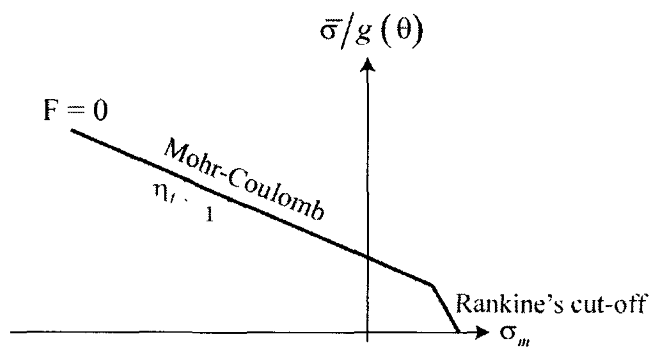

Figure 2.4 – Adopted failure surface for brick and mortar in the meridional plane

In the second equation of (2.6), ξ is the internal variable accounting for the history of the accumulated plastic distortions and is defined as

$$\xi = \bar{\varepsilon}^p = \int \dot{\bar{\varepsilon}}^p dt; \quad \dot{\bar{\varepsilon}}^p = \left(\frac{1}{2}\dot{e}^p_{ij}\dot{e}^p_{ij}\right)^{1/2} \tag{2.7}$$

where, $\dot{e}^p_{ij}$ represents the deviatoric part of the plastic strain rate

$$\dot{e}^p_{ij} = \dot{\varepsilon}^p_{ij} - \frac{1}{3}\delta_{ij}\dot{\varepsilon}^p_{kk} \tag{2.8}$$

The function $\eta(\xi)$ is assumed in such a way as to ensure a smooth transition from the initial slope of the yield surface, η_i, to that of the failure locus, η_f

$$\eta(\xi) = \eta_0 + \frac{\xi}{A+\xi}(\eta_f - \eta_0) \tag{2.9}$$

In the latter equation, A is a material constant which can be defined from standard experimental tests, such as uniaxial or 'tri-axial' compression. Figure 2.5 depicts the employed yield surface for different stress regimes.

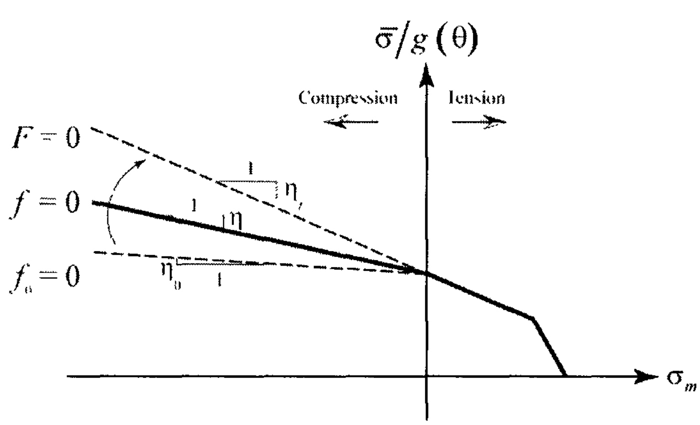

Figure 2.5 – Yield/failure surfaces in the meridional plane

Plastic Potential Surface

A non-associated flow rule has been incorporated to define the direction of plastic flow. In particular, a logarithmic plastic potential surface has been employed to ensure a smooth transition from compaction to dilation (Figure 2.6).

$$\psi = \frac{\bar{\sigma}}{g(\theta)} + \eta_c \bar{\sigma}_m \ln \frac{\bar{\sigma}_m}{\bar{\sigma}_m^0} = 0, \qquad \bar{\sigma}_m = \sigma_m + \frac{\mu}{\eta_c} \tag{2.10}$$

In the expressions above, η_c represents the slope of zero dilatancy line. It is noted that $\bar{\sigma}_m^0$ is evaluated based on the current stress state, so that $\psi = 0$ represents a parametric equation that defines a family of potential surfaces.

General Framework

The loading/unloading criteria are established using the standard Kuhn–Tucker conditions (Karush, 1939; Kuhn and Tucker, 1951). According to these criteria, the

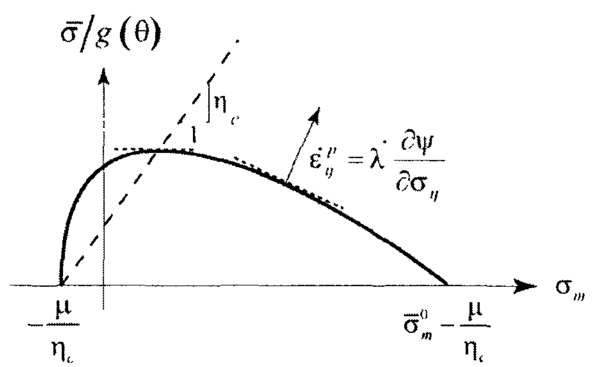

Figure 2.6 – Plastic potential surface

constitutive relation is defined as

$$\begin{cases} \dot{\sigma}_{ij} = D^{e}_{ijkl}\dot{\varepsilon}_{kl} \quad , \quad f < 0 \vee \left(f = 0 \wedge \dfrac{\partial f}{\partial \sigma_{ij}} \dot{\sigma}_{ij} \leq 0 \right) \\ \dot{\sigma}_{ij} = D^{ep}_{ijkl}\dot{\varepsilon}_{kl} \quad , \quad f = 0 \wedge \dfrac{\partial f}{\partial \sigma_{ij}} \dot{\sigma}_{ij} > 0 \end{cases} \tag{2.11}$$

Here, D^{e}_{ijkl} is the elastic constitutive operator which, for an isotropic material, is defined by the generalized Hook's law. D^{ep}_{ijkl} is the elastoplastic operator, which is defined by employing the standard plasticity procedure as outlined below. The plastic strain rate tensor is defined by invoking a non-associated flow rule

$$\dot{\varepsilon}^{p}_{ij} = \dot{\lambda}\frac{\partial \psi}{\partial \sigma_{ij}} \tag{2.12}$$

Here, $\dot{\lambda}$ is the plastic multiplier that defines the magnitude of the plastic strain for an arbitrary stress/strain rate. The formulation involves the additivity postulate that asserts that the total strain rate is the sum of elastic (reversible) and plastic (irreversible) parts, i.e.

$$\dot{\varepsilon}_{ij} = \dot{\varepsilon}^{e}_{ij} + \dot{\varepsilon}^{p}_{ij} \tag{2.13}$$

Substituting the additive postulate in the elastic constitutive relation, one obtains

$$\dot{\sigma}_{ij} = D^{e}_{ijkl}\left(\dot{\varepsilon}_{kl} - \dot{\lambda}\frac{\partial \psi}{\partial \sigma_{kl}} \right) \tag{2.14}$$

The plastic multiplier can now be calculated by invoking the consistency condition, which for a deviatoric hardening material takes the form

$$\dot{f} = \frac{\partial f}{\partial \sigma_{ij}} D^{e}_{ijkl} \left(\dot{\varepsilon}_{kl} - \dot{\lambda} \frac{\partial \psi}{\partial \sigma_{kl}} \right) + \dot{\lambda} \frac{\partial f}{\partial \bar{\varepsilon}^{p}} \left(\frac{1}{2} \operatorname{dev} \frac{\partial \psi}{\partial \sigma_{ij}} \operatorname{dev} \frac{\partial \psi}{\partial \sigma_{ij}} \right)^{1/2} = 0 \tag{2.15}$$

The latter equation can be solved for $\dot{\lambda}$, so that

$$\dot{\lambda} = \frac{1}{H_e + H_p} \frac{\partial f}{\partial \sigma_{ij}} D^{e}_{ijkl} \dot{\varepsilon}_{kl} \tag{2.16}$$

in which $H_e = \frac{\partial f}{\partial \sigma_{ij}} D^{e}_{ijkl} \frac{\partial \psi}{\partial \sigma_{kl}}$ and $H_p = -\frac{\partial f}{\partial \bar{\varepsilon}^{p}} \left(\frac{1}{2} \operatorname{dev} \frac{\partial \psi}{\partial \sigma_{ij}} \operatorname{dev} \frac{\partial \psi}{\partial \sigma_{ij}} \right)^{1/2}$ (2.17)

In the latter expression $\operatorname{dev} \frac{\partial \psi}{\partial \sigma_{ij}}$ represents the deviatoric part of $\frac{\partial \psi}{\partial \sigma_{ij}}$. Eventually, the tangential elastoplastic operator prior to the inception of localization can be obtained by substituting $\dot{\lambda}$ into Equation (2.14)

$$D^{ep}_{ijkl} = D^{e}_{ijkl} - \frac{1}{H_e + H_p} \left(D^{e}_{ijpq} \frac{\partial \psi}{\partial \sigma_{pq}} \frac{\partial f}{\partial \sigma_{mn}} D^{e}_{mnkl} \right) \tag{2.18}$$

(ii) Post-Localization Response

Failure criterion defines the strength of a given constituent under any possible combination of stress. Once the failure criterion is met, it is assumed that the intact material is intercepted by a distinct macrocrack in the specific direction (Figure 2.7). The orientation of the macrocrack is identified based on the inherent characteristics of the active failure locus. For a Mohr-Coulomb criterion, this orientation in $\sigma_1 - \sigma_3$ plane

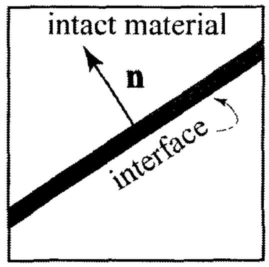

Figure 2.7 – Schematic representation of the intact material intercepted by a macrocrack

would be defined as $\theta = \frac{\pi}{4} + \frac{\phi_f}{2}$, and is measured with respect to the minor principal stress axes, σ_3. For the Rankine's cut-off, however, it is assumed that the unit normal to the localized plane, n_i, is the unit vector defining the maximum tensile principal stress axis, σ_1. These vectors can be defined in a local coordinate system attached to the principal stress axes as

$$\begin{aligned} n_i &= \left\langle \cos\left(\frac{\pi}{4} + \frac{\phi_f}{2}\right) \quad 0 \quad -\sin\left(\frac{\pi}{4} + \frac{\phi_f}{2}\right) \right\rangle^{\mathrm{T}} && \cdots \text{ for Mohr-Coulomb criterion} \\ n_i &= \langle 1 \quad 0 \quad 0 \rangle^{\mathrm{T}} && \cdots \text{ for Rankine criterion} \end{aligned} \tag{2.19}$$

The thickness of the localization band is assumed to be negligible compared to the dimensions of the elementary volume considered. Furthermore, the properties along the interface are assumed to be different from those of the intact material. In order to assess the average macroscopic response, a simple volume averaging procedure is employed based on the work reported by Pietruszczak and Niu (1993), and Pietruszczak (1999). The procedure incorporates the stress/strain rate averaging

$$\dot{\sigma}_{ij} = \upsilon^{(1)}\dot{\sigma}^{(1)}_{ij} + \upsilon^{(2)}\dot{\sigma}^{(2)}_{ij} \; ; \; \dot{\varepsilon}_{ij} = \upsilon^{(1)}\dot{\varepsilon}^{(1)}_{ij} + \upsilon^{(2)}\dot{\varepsilon}^{(2)}_{ij} \tag{2.20}$$

Here, the superscript (1) refers to the intact material whereas (2) represents the fractured zone. The coefficients $\upsilon^{(1)}$ and $\upsilon^{(2)}$ are the volume fractions of the intact material and that confined to the fractured zone, respectively.

The mechanical response along the fractured zone can be estimated, either by employing a rigorous micro-mechanical analysis or by using a macroscopic framework. The macroscopic/continuum approach is not only simpler, but also requires a considerably fewer number of material parameters. Therefore, this approach is adopted in the present work. The strain rate within the fractured zone is defined in terms of velocity discontinuities across the interface, g_i, and is expressed as a symmetric part of a dyadic product (cf. Pietruszczak, 1999)

$$\dot{\varepsilon}^{(2)}_{ij} = \frac{1}{2h}\left(n_i \dot{g}_j + n_j \dot{g}_i\right) \tag{2.21}$$

where h denotes the thickness of the shear band. Considering now the equilibrium requirements for the traction vector along the discontinuity plane, i.e. $\dot{t}^{(1)}_i = \dot{t}^{(2)}_i$, and noting that $\dot{t}^{(1)}_i = \dot{\sigma}^{(1)}_{ij} n_j$ and $\dot{t}^{(2)}_i = K_{ij}\dot{g}_j$, one can write

$$D^{e}_{ijkl} n_j \dot{\varepsilon}^{(1)}_{kl} = K_{ij}\dot{g}_j \tag{2.22}$$

where K_{ij} is the elastoplastic operator defining the properties within the fracture zone.

Since the thickness h of the localization zone is negligible compared to the other dimensions of the representative volume, one can conclude that $\upsilon^{(1)} \approx 1$. In this case, the second equation in representation (2.20) can be expressed as

$$\dot{\varepsilon}_{ij} = \dot{\varepsilon}_{ij}^{(1)} + \frac{\upsilon}{2}\left(n_i \dot{g}_j + n_j \dot{g}_i\right) \tag{2.23}$$

Here, $\upsilon = \upsilon^{(2)}/h$ is a characteristic dimension that is defined as the ratio of the surface area of the localization plane to the volume of the element. Multiplying both sides of this equation by $D_{ijkl}^{e} n_j$, one can obtain

$$\dot{g}_i = S_{ijk} \dot{\varepsilon}_{jk} \tag{2.24}$$

where

$$S_{ijk} = E_{ip}^{-1} D_{pqjk}^{e} n_q ; \qquad E_{ij} = K_{ij} + \upsilon D_{ipqj}^{e} n_p n_q \tag{2.25}$$

The operator referred to as S_{ijk} is structural tensor which defines the velocity discontinuity in terms of the macroscopic strain rate. The stress rate in the intact material can be related to the homogenized strain rate by substituting Equation (2.25) into Equation (2.23), which yields

$$\dot{\sigma}_{ij}^{(1)} = D_{ijpq}^{e}\left(\delta_{pk}\delta_{ql} - \upsilon n_p S_{qkl}\right)\dot{\varepsilon}_{kl} \tag{2.26}$$

Given the negligible thickness of the localized zone, one may conclude that $\dot{\sigma}_{ij}^{(1)} \approx \dot{\sigma}_{ij}$, and therefore

$$\dot{\sigma}_{ij} = D_{ijkl}^{H} \dot{\varepsilon}_{kl} \tag{2.27}$$

The above equation relates the homogenized stress rate within a representative volume to the macroscopic strain rate, and therefore represents the average constitutive relation for a medium intercepted by a macrocrack. Thus, the constitutive operator is defined as

$$D^{H}_{ijkl} = D^{e}_{ijpq}\left(\delta_{pk}\delta_{ql} - \upsilon n_p S_{qkl}\right) \tag{2.28}$$

It should be noted that in this equation, D^{e}_{ijpq} is identified with the elastic constitutive matrix of the intact material. That is due to the fact that the intact material is unloading in this region, in view of the strain-softening characteristics in the fractured zone. The characteristic dimension υ is one of the major parameters affecting the softening behavior. Within the context of finite element analysis, this parameter can be estimated assuming that the volume associated with each Gauss point is concentrated within an equivalent sphere. Thus,

$$\upsilon = \frac{1}{l} = \sqrt[3]{\frac{4\pi}{3V}} \tag{2.29}$$

The elastoplastic operator K_{ij}, defining the response in the localized zone, is obtained by incorporating a strain-softening plasticity framework. Here, a quadratic yield locus is employed (cf. Stankowski et al., 1993; and Lotfi and Shing, 1994)

$$f = \sigma_0\tau^2 + B^2(\kappa)\left(\sigma - C(\kappa)\right) = 0 \tag{2.30}$$

where

$$C(\kappa) = \sigma_0 e^{-\alpha\kappa}, \text{ and } B(\kappa) = B_0 e^{-\beta\kappa}$$

In the latter expression, σ_0 represents the value of the tensile strength at the interface at the onset of localization and α, and β are parameters describing the rate of stress softening. The parameter B_0 is evaluated at the onset of localization, as

$$B_0 = \tau \sqrt{\frac{\sigma_0}{\sigma_0 - \sigma}} \tag{2.31}$$

where $\tau = \sqrt{t_1^2 + t_2^2}$, $\sigma = t_3$ and $t_i = \langle t_1 \quad t_2 \quad t_3 \rangle^{\mathrm{T}}$ is the traction vector at the interface referred to the local coordinate system.

Note that a decrease in the value of parameter C in the course of loading causes a shift of the yield surface along the σ axis, whereas the decrease in B changes the shape of the surface (Figure 2.8). The internal parameter κ is defined in rate form as

$$\dot{\kappa} = \left(\dot{g}_i^p \dot{g}_i^p \right)^{1/2}; \qquad \dot{g}_i^p = \dot{\lambda} \frac{\partial f}{\partial t_i} \tag{2.32}$$

where, $g_i^p = \langle \dot{g}_1^p \quad \dot{g}_2^p \quad \dot{g}_3^p \rangle^{\mathrm{T}}$ is the plastic part of the velocity discontinuity vector. The

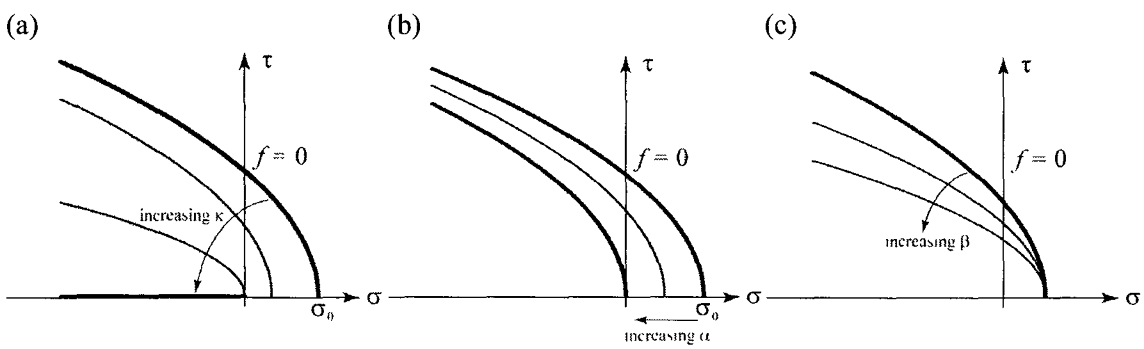

Figure 2.8 – Yield surface in the localized zone; effect of different parameters: (a) κ; (b) α; and (c) β

normal and tangential components of traction are specified as

$$\sigma = \sigma_{ij} n_i n_j, \quad \tau = \sigma_{ij} n_i s_j \tag{2.33}$$

in which

$$s_i = t_i^s / \left\| t_i^s \right\|, \quad t_i^s = \left(\delta_{ij} - n_i n_j \right) \sigma_{jk} n_k, \quad \left\| t_i^s \right\| = \left(t_i^s t_i^s \right)^{1/2} \tag{2.34}$$

Writing $\dot{t}_i = K_{ij} \dot{g}_j$ and recalling the additivity postulate one obtains

$$\dot{t}_i = K_{ij}^e \left(\dot{g}_j - \dot{g}_j^p \right) \tag{2.35}$$

Here, K_{ij}^e represents the elastic constitutive matrix in the localized zone and is expressed as

$$K_{ij}^e = \begin{bmatrix} k_T & 0 & 0 \\ 0 & k_T & 0 \\ 0 & 0 & k_N \end{bmatrix} \tag{2.36}$$

where k_T and k_N define the elastic moduli per unit cross-sectional area of the interface.

By invoking now the consistency condition and employing an associated flow rule (to account for the progressive dilatation of the material) one can obtain the elastoplastic operator

$$K_{ij}^{ep} = K_{ij}^e - \frac{1}{H_e + H_p} \left(K_{im}^e \frac{\partial f}{\partial t_m} \frac{\partial f}{\partial t_n} K_{nj}^e \right) \tag{2.37}$$

where

$$H_e = \frac{\partial f}{\partial t_i} K^e_{ij} \frac{\partial f}{\partial t_j} = 4\sigma_0^2 \tau^2 k_T + B^4 k_N$$

$$H_p = -\frac{\partial f}{\partial \kappa} \left(\frac{\partial f}{\partial t_k} \frac{\partial f}{\partial t_k} \right)^{1/2} = \left(2\beta B^2 \left(\sigma - C\left(\kappa\right) \right) - \alpha B^2 C \right) \sqrt{4\sigma_0^2 \tau^2 + B^4} \tag{2.38}$$

2.3. IMPLEMENTATION

In order to implement the constitutive model described above, a user defined subroutine is developed within FORTRAN 90 and is linked to COSMOS 2.7 FE package. In this commercial finite element package, the following element groups can be associated with a user-defined material model:

- 2–D and 3–D truss elements
- 2–D, 4 or 8-node plane elements (plane stress, plane strain and axisymmetric)
- 2–D, 3 or 6-node triangle elements (plane stress, plane strain and axisymmetric)
- 3–D, 8 or 20-node brick elements
- 3–D, 4 or 10-node tetrahedral elements

In the course of this study, only 3–D, 8-node brick elements have been used.

(i) Stability Indicator

The onset of global loss of stability can be detected using a suitably defined stability factor (*SF*). In this study, a simplified energy approach is employed (after Pietruszczak and Oulapour, 1999) in which the stability factor is defined in terms of the normalized second rate of work at each load step

$$SF = \frac{\int_V \dot{\sigma}_{ij} \dot{\varepsilon}_{ij} \, dV}{\int_V \dot{\sigma}^{e}_{ij} \dot{\varepsilon}_{ij} \, dV} \tag{2.39}$$

In the equation above, the denominator represents the second rate of work in an elastic continuum; $\dot{\sigma}_{ij}$ is the actual stress rate, $\dot{\sigma}^{e}_{ij}$ is the elastic stress rate, and the integration is carried out over the entire domain. It should be noted that in elastic domain the value of SF remains equal to one, while beyond that limit it gradually decreases until, at the onset of global instability, it becomes equal to zero. The progression into the unstable zone yields a negative value of SF.

(ii) Parametric Study

In order to verify the performance of the presented material model some simple boundary value problems have been analyzed and the effect of various material parameters on the overall response has been examined. In particular, a sample of mortar with an aspect ratio of 4.0 (40 mm width × 160 mm height) is considered here, subjected to two different loading histories, namely uniaxial tension and uniaxial compression. A displacement-controlled analysis is carried out to ensure capturing of the global softening response. A small imperfection zone is introduced in the middle of the specimen in order to enforce the onset of crack propagation (Figure 2.9). The strength parameters, such as uniaxial tensile and compressive strength, as well as the modulus of elasticity in the imperfection zone are considered to be 30% of those of the mortar. A constant velocity field is imposed in the *y*-direction along the top surface. The lower surface is restrained against vertical displacement, and the entire domain is discretized into 1936, 8-node solid elements. Elastic modulus and the strength parameters are fixed, while a parametric study is conducted on other model parameters in order to examine their overall effect on the response of the specimen. The parameters employed in this study are summarized in Tables 2.1, 2.2, and 2.3.

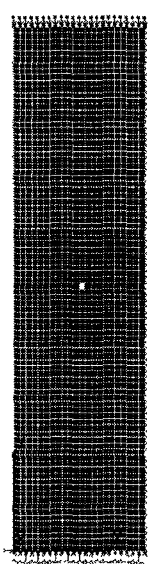

Figure 2.9 – Geometry and Boundary Conditions of the adopted specimen

Table 2.1 – Material properties for the specimen

		Value
Elastic properties	E (MPa)	1050
	ν	0.06
Failure Surface Parameter	c (MPa)	1.0
	ϕ (°)	37
	f_c (MPa)	4.0
	f_t (MPa)	0.8
Interface properties	k_N (MPa/m)	25000
	k_T (MPa/m)	12500

Table 2.2 – Material properties for the imperfection

		Value
Elastic properties	E (MPa)	315
	ν	0.06
Failure Surface Parameter	c (MPa)	0.3
	ϕ (°)	37
	f_c (MPa)	1.2
	f_t (MPa)	0.24
Interface properties	k_N (MPa/m)	7500
	k_T (MPa/m)	3750

Table 2.3 – Model parameters

		Value
Elastoplastic parameters	A	10^{-5}, 5×10^{-5}, 10^{-4}
	η_t	0.0
	η_c	0.869
Softening parameters	α (m^{-1})	500 – 2000
	β(m^{-1})	100 – 1000

Tension Test

By examining the Equation (2.30), it is clear that B has a negligible effect on the behavior of the softening branch in tension. This is due to the fact that for this loading history the shear stress at the interface is zero. Therefore, the main parameter affecting the softening response for this loading history is α. The results of parametric studies employing different values of this parameter are presented in Figure 2.10. As anticipated, an increase in α results in a steeper response in post-localization zone. The typical damage propagation pattern is depicted in Figure 2.11.

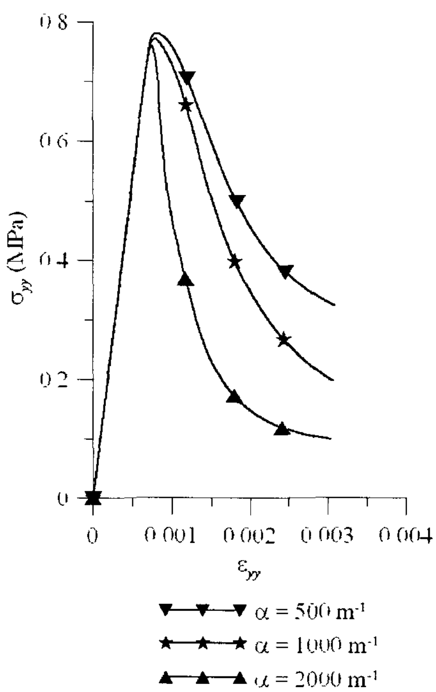

Figure 2.10 – Behavior in tension regime, $\beta = 300$ m^{-1}

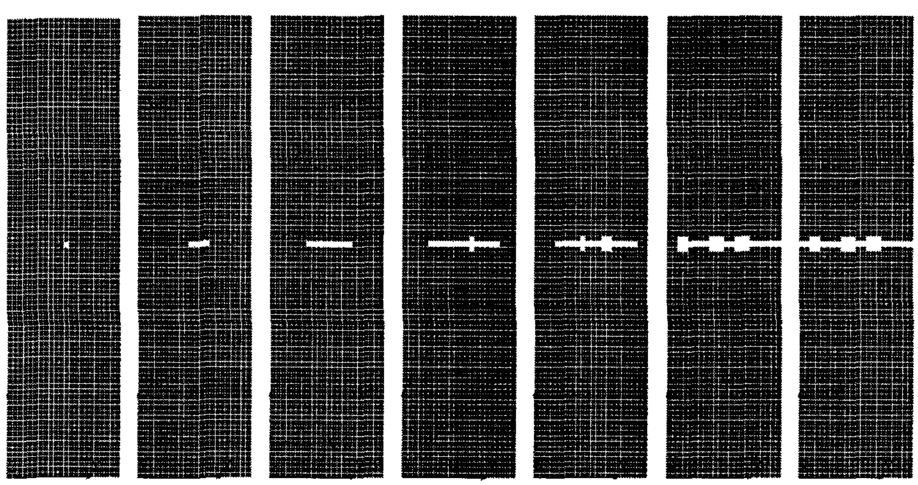

Figure 2.11 – Crack propagation pattern within a sample subjected to uniaxial tension

Compression Test

An axial compression test has been simulated in order to evaluate the performance of the model in compression regime, and to study the effect of the parameters A , α , and β . In the numerical analysis, the upper surface of the specimen was subjected to a uniform velocity field imposed in the *y*-direction. Figure 2.12 shows the effect of parameter A on the pre-localization behavior, while Figures 2.13 and 2.14 depict the effect of different values of softening parameters on the post-localization response. The typical crack propagation pattern under such loading is presented in Figure 2.15. As anticipated, the crack initiates within the imperfection zone and subsequently propagates through the surrounding elements in a pattern consistent with the experimental evidence. Apparently, while the softening parameters do not drastically change the ultimate load, they significantly affect the post-softening response.

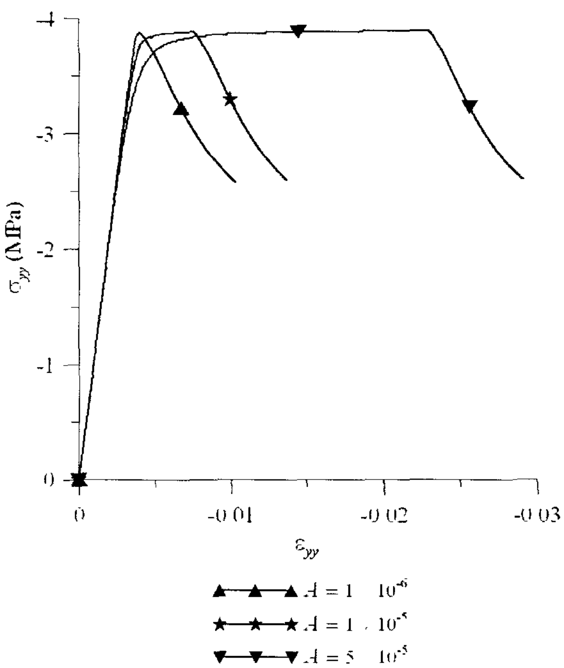

Figure 2.12 – Parametric study on A: $\eta_c = 0.869$, $\alpha = 1000\ m^{-1}$, $\beta = 300\ m^{-1}$

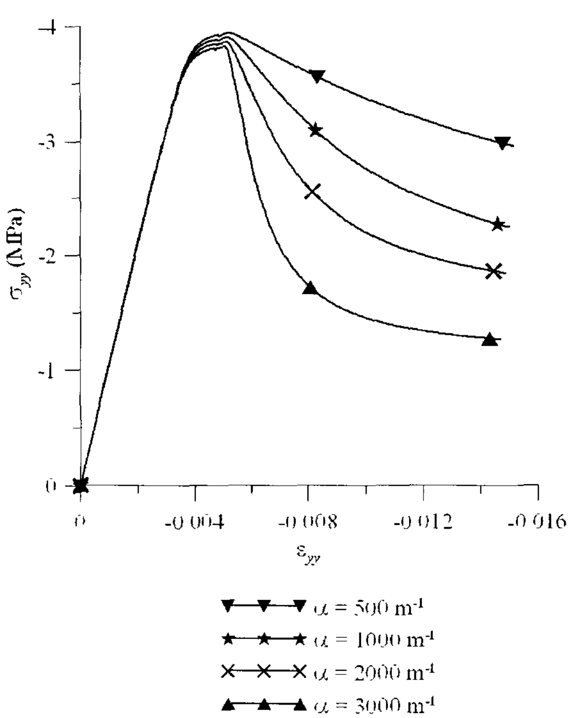

Figure 2.13 – Parametric study for α: $\beta = 300\ m^{-1}$

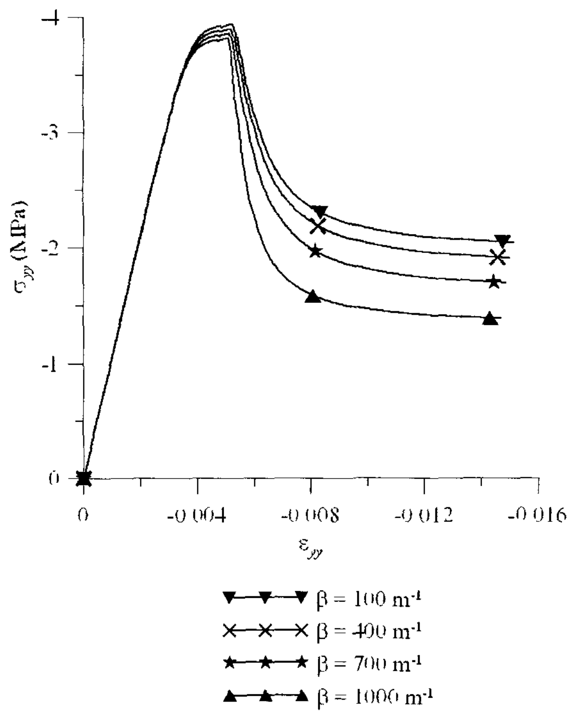

Figure 2.14 – Parametric study on β: $A = 10^{-6}$, $\alpha = 2000$ m^{-1}

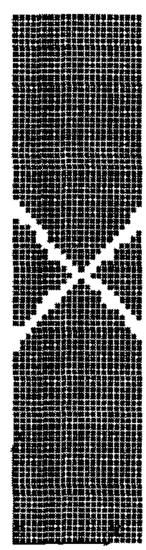

Figure 2.15 – Crack propagation pattern for the specimen with imperfection subjected to uniaxial compression

2.4. FINAL REMARKS

In this chapter an advanced constitutive model was presented which is capable of addressing all distinct stages of deformation, i.e. elastic, elastoplastic and softening. Subsequently, the model was implemented in a commercial Finite Element package, and a series of simple boundary value problems were solved. The objective was to assess the effect of different model parameters on the pre and post-localization response. In the next chapter, the performance of the model is verified further using the experimental data available in the literature.

CHAPTER 3

DISCRETE ANALYSIS; MESOSCALE APPROACH

3.1. INTRODUCTION

In the preceding chapter a constitutive model was developed and implemented in COSMOS 2.7 FE package as a user-defined material module. Some simple boundary value problems were solved in order to verify its performance. In this chapter, an extensive numerical analysis is conducted which involves modeling of some experimental tests carried out on brick masonry. These tests include the shear tests conducted by van der Pluijm (1993), the direct shear tests performed by Atkinson et al. (1989), and the biaxial tension - compression tests carried out by Page (1983). A mesoscopic modeling scheme is employed during the course of the analysis, in which brick and mortar are discretized and modeled separately. Both constituents, i.e. brick and mortar, are assumed to be homogeneous within themselves.

3.2. SIMULATION OF TESTS CONDUCTED BY VAN DER PLUIJM

Rob van der Pluijm (1993) carried out a series of tests to investigate the strength of bed joints under shear displacement loading, which to date presents the most comprehensive characterization of the shear behavior of the brick masonry. The shear and tensile bond strength were determined separately. A total number of 54 displacement-controlled tests were performed on specimens which consisted of two 200 × 100 × 50 mm brick units with a bed joint of thickness of 15 mm. The specimens were pre-stressed in a direction normal to the bed joints and the level of the normal compressive stress varied between 0.1 MPa and 1.0 MPa. The shear load was applied to the specimen by imposing a vertical displacement on the upper L-shaped mould, as shown in Figure 3.1.

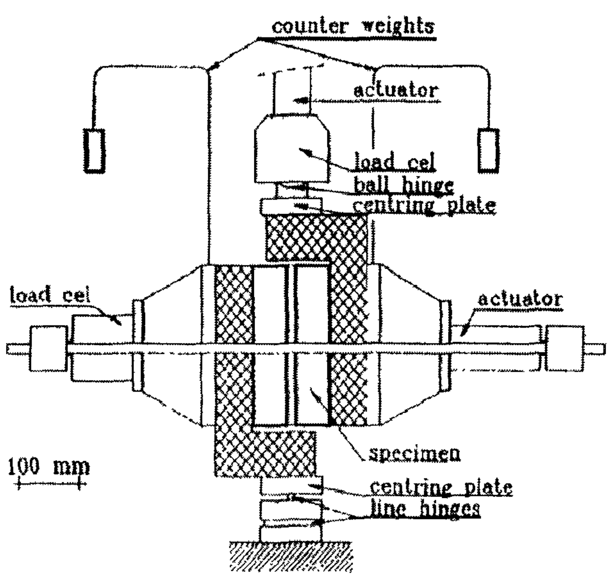

Figure 3.1 – Test specimen and the load rig, after van der Pluijm (1993)

Numerical model and results of simulations

The constitutive model developed in previous chapter has been employed to assess the ultimate load bearing capacity and the damage propagation for specimens tested at different values of normal stresses. Both the test specimen and the L-shaped mould were discretized. A 3-D mesh with a total number of 2884 nodes and 1320, 8-noded solid elements was employed. In order to decrease the overall number of unknowns, a much coarser mesh was employed for discretization of the L-shaped moulds. In this region, a mixed constraint formulation was used to solve the problem (Zienkiewicz and Taylor, 2000). In this approach, which is an example of a "partial field" approximation, the entire region is subdivided into two or more sub-domains, in each of which an irreducible (displacement) formulation is implemented. Independently approximated Lagrange multipliers (tractions) are used on each interface to join the sub-domains. The standard virtual work expressions in each sub-domain are supplemented by weak statements of displacement continuity at the interfaces between the adjacent domains (Zienkiewicz and Taylor, 2000).

The mould was made of steel, and within the range of the imposed loading was assumed to behave elastically. The key material parameters for the specimen are given in Table 3.1. In general, the values of f_c, ϕ, and c are related through the following equations

$$f_c = \frac{3\mu}{\sqrt{3}-\eta_f}; \quad \eta_f = \frac{2\sqrt{3}\sin\phi}{3-\sin\phi}, \quad \mu = \frac{2c\sqrt{3}\cos\phi}{3-\sin\phi}$$

Here, the angle of internal friction for each constituent was chosen based on some typical values reported in the literature, while the corresponding value of cohesion c was evaluated from the equation above using f_c that is specified in Table 3.1. Note that in the numerical simulations the properties of mortar were replaced by those of a weaker mortar-brick interface. This is a simplification introduced in order to avoid the need for employing the interface elements in the course of FE analysis. Furthermore, no experimental information was provided on the material parameters A and η_c, Equations (2.9) and (2.10). Thus, the values were chosen on purely intuitive basis using the information from parametric studies conducted in the preceding chapter. For both brick and mortar it was assumed that $A = 10^{-5}$, while the slope of the zero dilatancy line was taken as $\eta_c = 0.85\eta_f$. Note that the primary focus here was on estimating the value of the ultimate load, rather than on an accurate modeling of deformation characteristics. In this context, the values of A and η_c have little influence on the results.

The identification of softening parameters α and β, Equations (2.30), requires a series of direct shear tests along the crack surface. Again, the results of such experiments were not available. Given this, a parametric study was conducted assessing the influence of these parameters on the value of the ultimate load. The results of this study which are described later in Figure 3.5, indicated that the sensitivity is not very pronounced for a broad range of the values of these parameters. In view of this, the actual simulations reported here were carried out assuming $\alpha = 1000\ \text{m}^{-1}$ and $\beta = 200\ \text{m}^{-1}$.

Finally, the values of elastic constants for the interface should be large enough to ensure that the behavior is predominantly plastic. The simulations were carried out assuming $k_N = 15000$ GP/m and $k_T = 10000$ GP/m.

In the loading process, a prescribed compressive normal stress was first imposed on the left side of the left L-shaped mould, which was also restrained against the vertical displacement along its bottom surface. The right L-shaped mould was then subjected to a vertical displacement on its top surface, which was applied incrementally. The finite element discretization is shown in Figure 3.2. Figure 3.3 shows the shear load-displacement curve obtained from numerical simulations against the experimental curves reported by van der Pluijm (1993). The ultimate load is reached without sustaining any substantial amount of vertical displacement. The damage propagation pattern is depicted in Figure 3.4, where the cracked elements are shown in white. By referring to this figure, one can see that the crack initiates in the middle of the mortar joint, where the maximum shear stress develops, and gradually propagates towards the edges of the specimen. When the crack covers the entire mortar joint, a global mechanism is formed and the softening branch commences.

Finally, Figure 3.5 shows the results of the parametric study mentioned earlier that was conducted to assess the influence of the softening parameters on the ultimate load. The analysis here was focused on the sample subjected to a normal compressive stress of 0.1 MPa. A series of 6 simulations were conducted, in which the effect of different pairs of α and β was studied. In total, two different values for α and three different values for β were considered. According to the results of this study, the influence of the softening parameters on the ultimate load is less pronounced than the scatter observed in the reported experiments.

Table 3.1 – Experimental data (van der Pluijm, 1993) and model parameters

Constituent	Property	Value
Brick	Young's modulus, E (MPa)	16700
	Poisson's ratio, ν	0.15
	Compressive strength, f_c (MPa)	66.0
	Tensile strength, σ_0 (MPa)	3.51
Brick and Mortar Interface	Young's modulus, E (MPa)	2974
	Mean tensile bond strength, σ_0 (MPa)	0.62
	Angle of internal friction, ϕ (°)	36
	Cohesion, c (MPa)	0.88

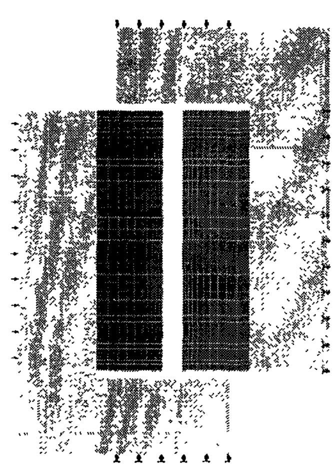

Figure 3.2 – Finite element discretization; van der Pluijm shear test (1993)

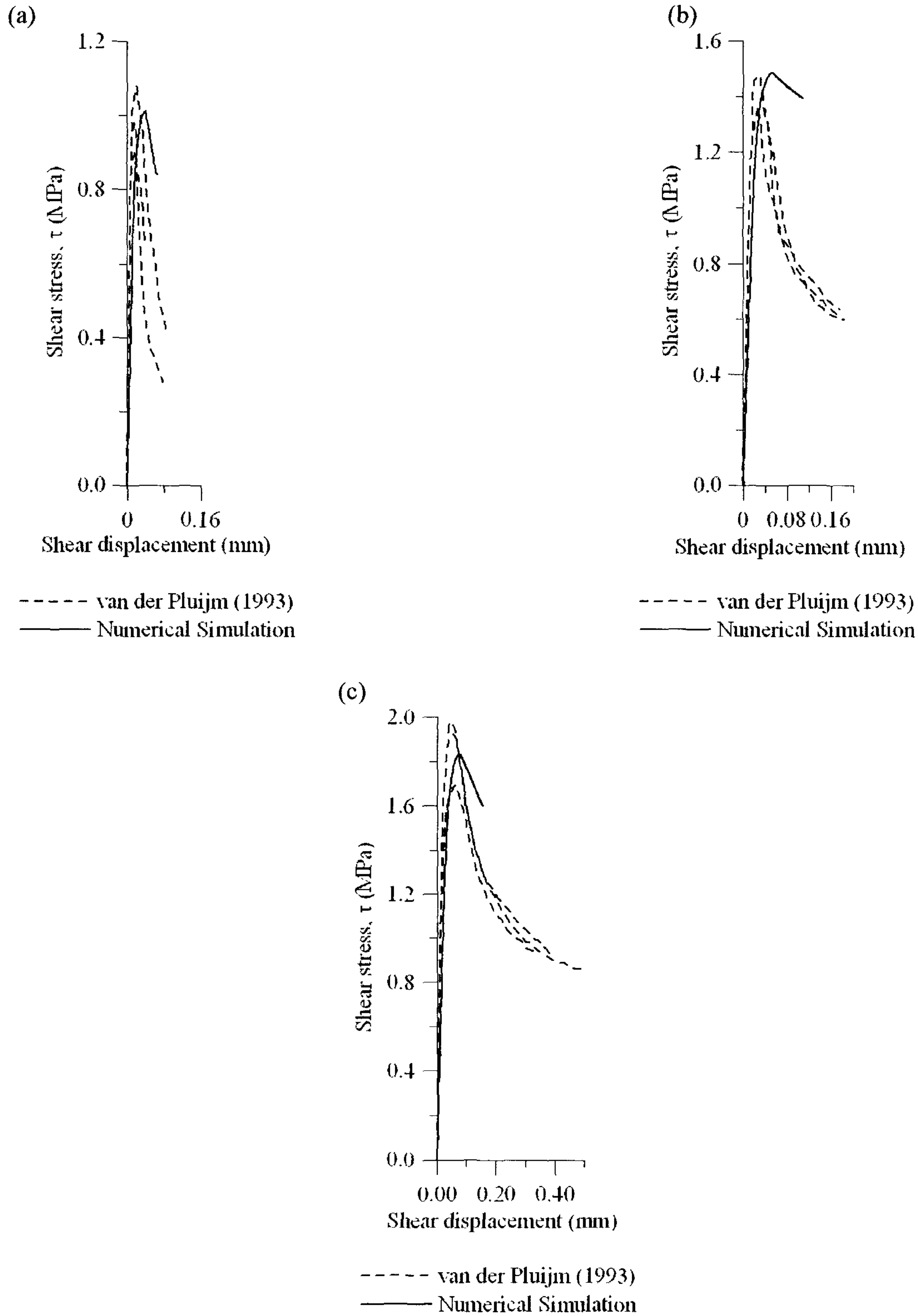

Figure 3.3 – van der Pluijm experiments v.s. finite element simulations: (a) σ_n = 0.1 MPa; (b) σ_n = 0.5 MPa; and (c) σ_n = 1.0 MPa

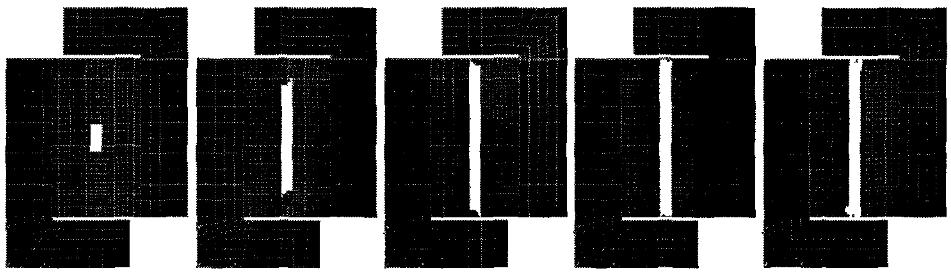

Figure 3.4 – Damage propagation pattern, van der Pluijm test (1993)

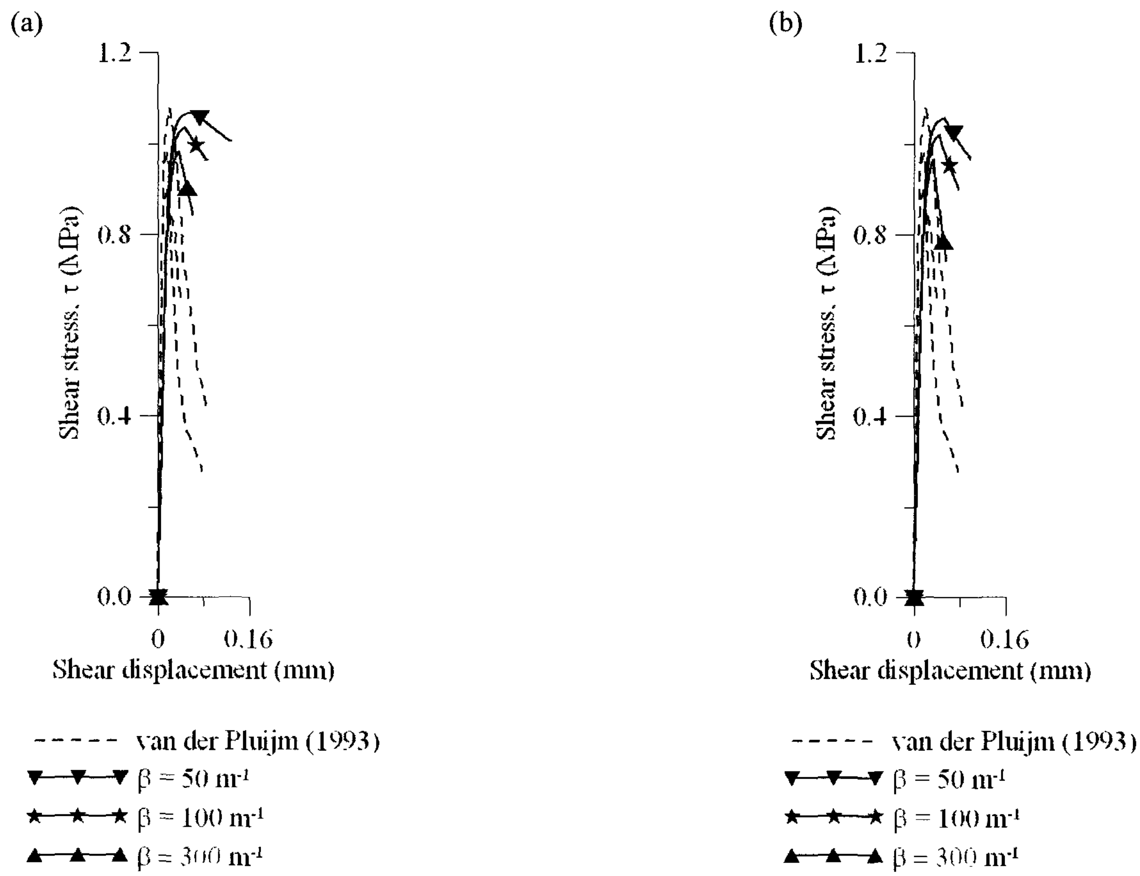

Figure 3.5 – Parametric study on the softening parameters for σ_n = 0.1 MPa: (a) α = 100 m^{-1}; and (b) α = 1000 m^{-1}

3.3. SIMULATION OF TESTS CONDUCTED BY ATKINSON ET AL.

Atkinson et al. (1989) performed a series of tests to obtain the shear strength and shear load-displacement characteristics of brick masonry under cyclic loading. More specifically, the objective was to obtain not only the ultimate load bearing capacity of the samples, but also to study their post peak response. A special testing apparatus capable of transferring both normal and shear loading was used (Figure 3.6). Due to the limitations of the apparatus, the maximum allowable size of the tested running bond brick work was 152 mm in width by 440 mm in length. During the test, the upper shear box was restrained against horizontal motion. The vertical load was applied first followed by imposing a relative motion of the bottom support plates, resting on two rows of roller bearings, against the restrained upper part. After applying a small seating load, the

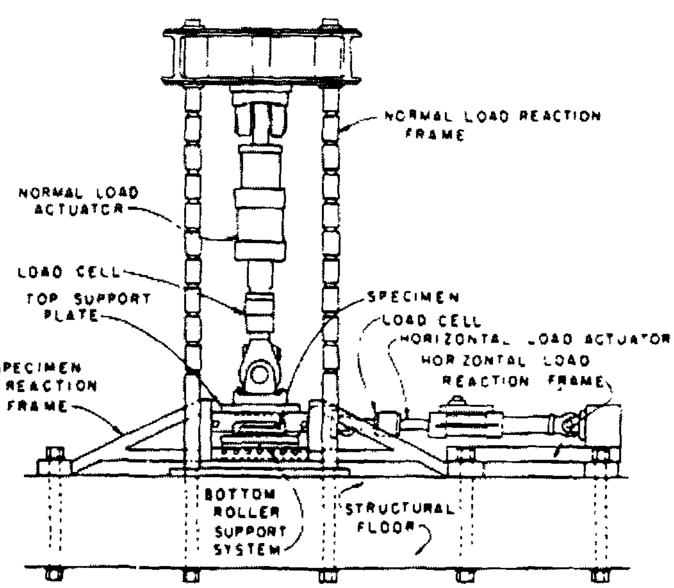

Figure 3.6 – Direct shear apparatus, Atkinson et al. (1989): Side view – schematic illustration

normal load was increased to the desired level and kept constant during the shear phase. Three distinct sets of constituent materials were used in the tests. First, a total of 44 experiments were performed on specimens consisting of old clay units and a mortar with the volumetric ratio of cement:lime:sand equal to 1:2:9. The bricks were obtained from an old building and were 208 × 100 × 64 mm in size. The thickness of the mortar joints was 13 mm. Second, another nine tests were carried out on specimens consisting of modern clay units, having the dimensions of 193 × 92 × 55 mm. The thickness of the mortar joint was approximately equal to 7 mm. Finally, some additional tests were carried out on the intact specimens of brick and mortar collected from older brick walls damaged during the 1987 Whitter, California earthquake. These samples consisted of two bricks intercepted by a mortar bed joint with a thickness ranging from 6 to 9 mm. The latter tests were performed to compare the laboratory test results with those of the field specimens.

The tests were conducted for a series of nominal normal stresses ranging between 0.36 MPa and 3.7 MPa for the old brick specimens, and between 0.4 MPa and 4.2 MPa for the new brick specimens.

(i) Numerical model

The three dimensional mesh (Figure 3.7) incorporated the clay bricks and the mortar joints as well as upper and lower platens. It employed 4760 nodes and 3762, 8-

noded solid elements. The upper platen was fixed on the right side, while the lower platen was constrained only in the vertical direction. Initially, the normal stress was gradually applied while the horizontal displacement was kept constant. After the normal vertical load was in place, uniform displacement increments were applied on the left hand side of the lower platen. The material parameters were chosen according to the data reported by Atkinson et al. (1989) and are shown in Table 3.2. Again, the remaining parameters that define the response in the elastoplastic regime were assessed using the same methodology as for van der Pluijm tests reported in the previous section. Thus, $A = 10^{-5}$ and $\eta_c = 0.85\eta_f$ were taken, while the values of softening parameters were assumed as $\alpha = 500$ m^{-1} and $\beta = 200$ m^{-1}.

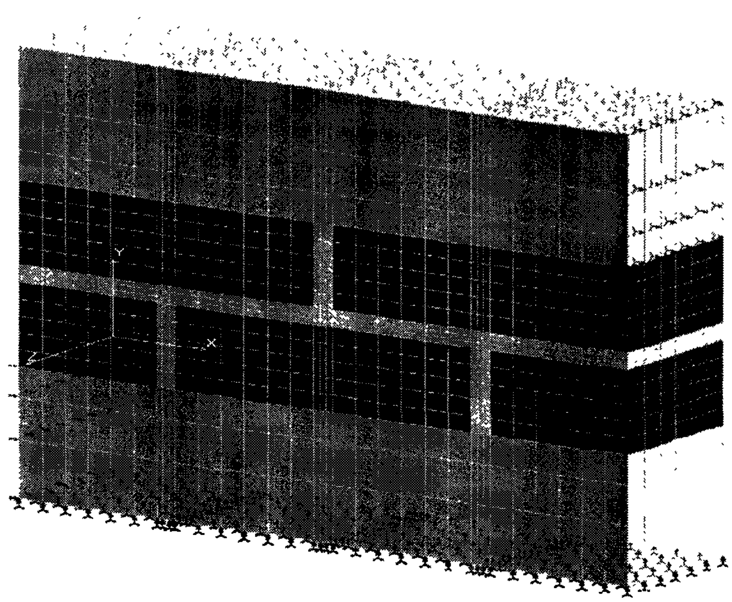

Figure 3.7 – 3D finite element model; Atkinson et al. direct shear experiments

Table 3.2 – Experimental data (Atkinson et al., 1989) and model parameters

	Old clay units	1:2:9 Mortar	New clay units	1:1.5:4.5 Mortar
E (MPa)	8796	1050	14701	2109
ν	0.16	0.06	0.22	0.05
σ_0 (MPa)	3.45	0.76	3.14	0.94
f_c (MPa)	33.10	4.87	64.00	5.16
ϕ (°)	30	35	30	37
c (MPa)	9.56	0.127	18.48	0.811

The simulations were carried out as displacement-controlled and the analysis was terminated shortly after the maximum load capacity was attained. The overall stability was monitored by examining the evolution of the safety indicator, Equation (2.39), which became negative as soon as the horizontal load started to decrease.

(ii) Results of numerical simulations

In this section the key results of numerical analysis are presented. Figure 3.8 (a) shows the response for the shear test performed on a brick masonry specimen consisting of old bricks and 1:2:9 mortar mixture with a 13-mm joint thickness, subjected to constant normal load of 13.7 kN. The ultimate load is reached shortly after the failure zone spreads throughout the entire bed joint area, and thereafter the behavior becomes unstable. In Figure 3.8 (b), the deformation characteristic for a specimen consisting of new bricks and 1:1.5:4.5 mortar mixture with a 7 mm joint thickness subjected to constant pre-stress load equal to 49 kN is presented. The results clearly show a rapid rise in the shear load to a peak value followed again by a decrease in the shear resistance in the post-peak regime, which is confirmed by the experimental evidence. It can be seen that there is a good agreement between the numerical analysis and the experimental data, particularly in the context of the assessment of the ultimate bearing capacity. Figure 3.9 shows the damage propagation, with the cracked elements marked as white. Since for this loading configuration the damage is confined to the bed joints, only the mortar joints are depicted in this figure. The propagation pattern is monitored by presenting a series of

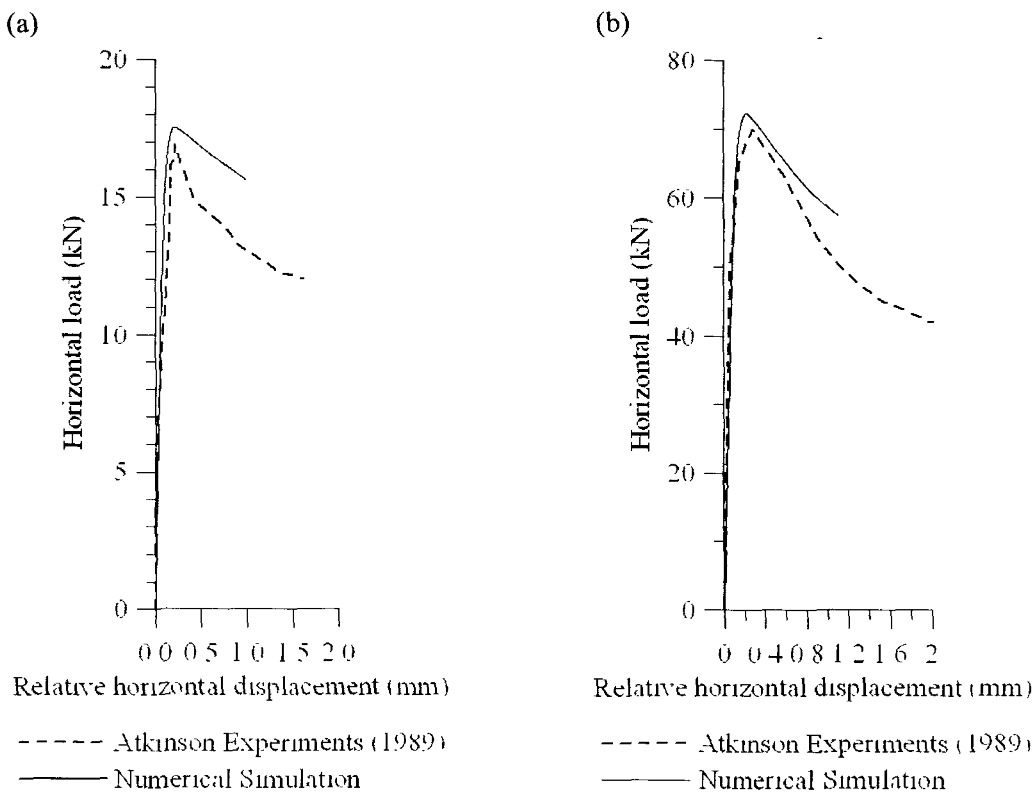

Figure 3.8 – Shear load-relative shear displacement, Atkinson et al. experiments (1989): (a) Old bricks, $\sigma_N = 330$kPa; (b) New bricks, $\sigma_N = 1.33$MPa

figures associated with different displacement increments. The top left figure shows the onset of cracking which commences at the intersection between the bed and the head joints (due to stress concentration). The propagation pattern through consecutive load steps is also depicted, leading to the formation of a global mechanism when the damaged zone eventually covers the entire bed joint area. In the latter case, the onset of global softening occurs. It is noted that while the higher normal pressure increases the ultimate bearing capacity, the damage propagation pattern remains unchanged.

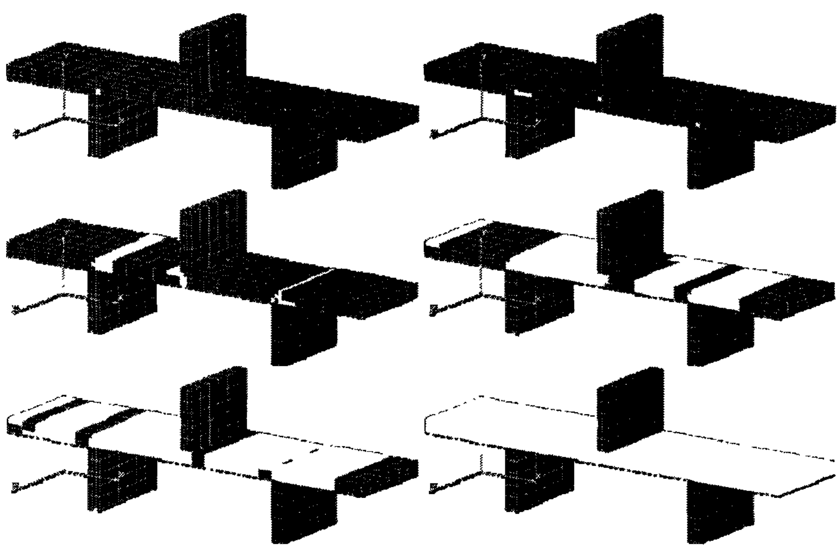

Figure 3.9 – Damage propagation, Atkinson et al. direct shear test

3.4. SIMULATION OF TESTS CONDUCTED BY PAGE

In the early 1980's, Page published the results of a series of tests designed to assess the directional strength characteristics of masonry panels subjected to in-plane monotonic loading. For that purpose, he conducted a series of biaxial tension-compression (Page, 1983) and biaxial compression-compression (Page, 1981) tests, which are still, to the author's knowledge, the most comprehensive experimental program conducted on the in-plane behavior of brick masonry. The test specimen consisted of a 360 × 360 mm square panel of running bond brick masonry constructed by adhering the bricks in their designated place to a temporary plate, and then pouring in mortar. Half-scale bricks were used, where the actual bricks were cut in half in all three dimensions (Figure 3.10). In the corners, each individual brick was sawn to the appropriate shape required to fit the designated angle. The specimens were subjected to a biaxial load-controlled test in the load rig shown in Figure 3.11. In order to alleviate the restraining

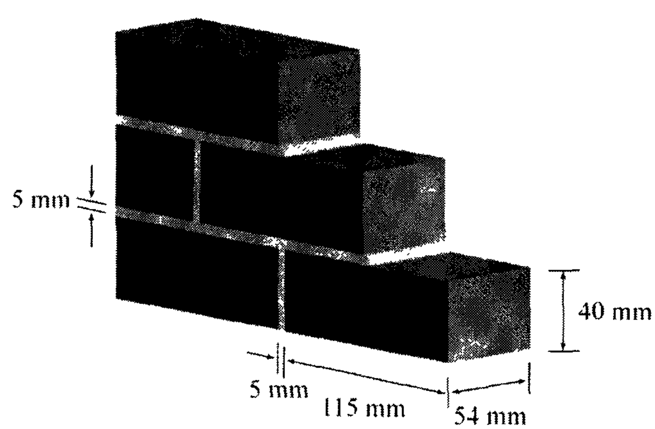

Figure 3.10 – Typical dimensions of the constituents implemented in Page test

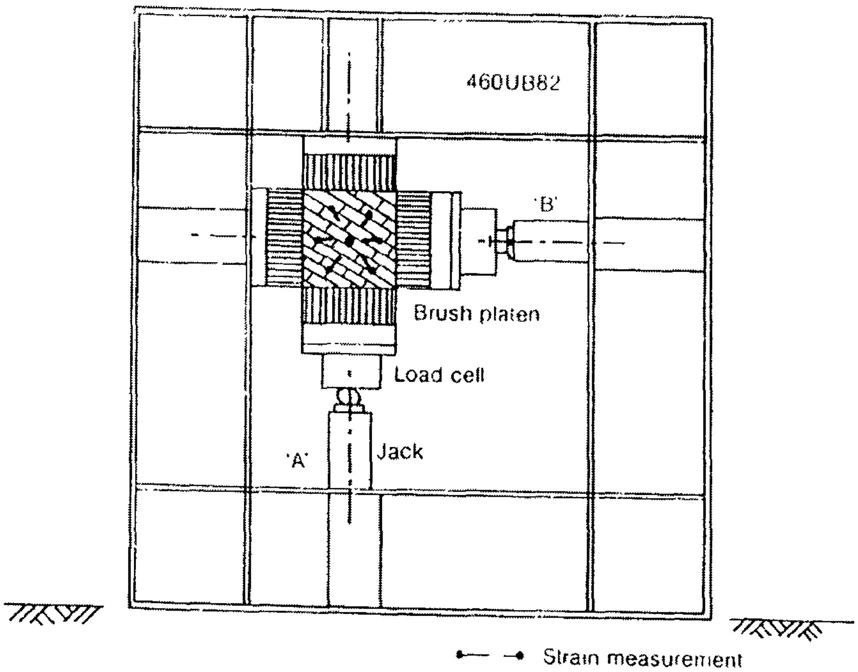

Figure 3.11 – Page test setup

effect of the loading caps, a series of brush platens were used to transfer the load to the panel. The tests were conducted for five different orientations, 0°, 22.5°, 45°, 67.5°, and 90°. The results from all orientations were then gathered to obtain a fairly comprehensive picture of the directional strength characteristics of brick masonry.

(i) Numerical model

The entire set up has been discretized using a three dimensional mesh with 37422 nodes and 30400, 8-noded solid elements, Figure 3.12. A non-uniform mesh was

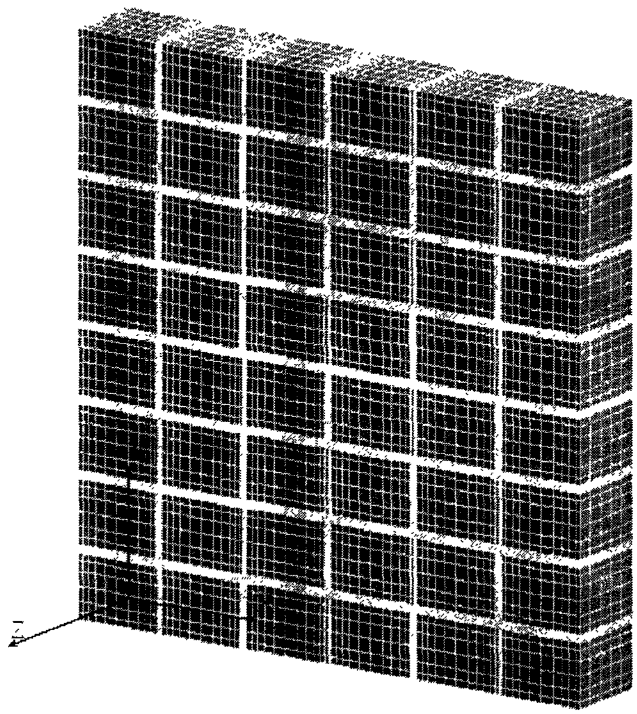

Figure 3.12 – Discretization of the Page panels (1983)

employed to account for the high deformation gradient regions. All the nodes on the centerline were fixed in the vertical direction. To eliminate all rigid body modes, the node at the intersection of the centerline and the front surface was fixed in all three directions. The loading was imposed on the boundaries of the specimen, where the brush platens made contact with the surface in real tests. Since the actual tests were performed using a force-controlled setup, the finite element analysis also incorporated the same loading scheme. The numerical simulations were carried out for different orientations of the bed joints relative to the loading direction. For each orientation, two different loading patterns were applied, namely uniaxial tension and biaxial tension-compression with $\sigma_c/\sigma_t = 1$

(equivalent to a pure shear at 45°). The basic material parameters, for both constituents, are listed in Table 3.3. This table gives the data reported by Page in the article of 1983. Based on this information and assuming some typical values for the angles of internal friction of constituents, the set of material parameters given in the table has been selected. Note that for the loading conditions considered here, the failure mechanism involves the fracture along the mortar joints that is initiated at the interfaces with brick units. Therefore, the values of strength parameters ϕ, c, and σ_0 reflect the properties of the interface rather than mortar, as it is more critical in the assessment of the strength of the panel. The remaining parameters, i.e. A, η_c, α and β were chosen according to the procedure outlined in Section 3.2. Thereby, it was assumed that $A = 10^{-5}$, $\eta_c = 0.85\eta_f$, α = 500 m^{-1}, and β = 200 m^{-1}. Once again, the stability indicator (Equation 2.39) was used to detect the ultimate load.

Table 3.3 – Experimental data (Page, 1983) and model parameters

Constituent	Property	Value
Brick	Module of elasticity, E_b (MPa)	6740
	Poisson's ratio, ν_b	0.167
	Compressive strength, $f_{c\,b}$ (MPa)	15.4
	Tensile strength, $\sigma_{0\,b}$ (MPa)	1.5
	Angle of intertal friction, ϕ_b (°)	30
	Cohesion, c_b (MPa)	4.35
Brick and Mortar Interface	Module of elasticity, E_m (MPa)	1700
	Poisson's ratio, ν_m	0.06
	Compressive strength, $f_{c\,m}$ (MPa)	5.08
	Tensile strength, $\sigma_{0\,m}$ (MPa)	0.24
	Angle of intertal friction, ϕ_m (°)	40
	Cohesion, c_m (MPa)	0.35

(ii) Results of numerical simulations

Uniaxial Tension

For uniaxial tension, the panel was subjected to the loading pattern shown in Figure 3.13. The load was gradually increased until the ultimate conditions were reached and the configuration became unstable (stability factor approaching zero). The simulations were performed for different orientations of the bed joints using 10° intervals. The directional strength characteristics obtained from numerical simulations are presented in Figure 3.14 and are compared with the Page data (1983). It can be seen from this figure that the experimental data is quite scattered. For most orientations, however,

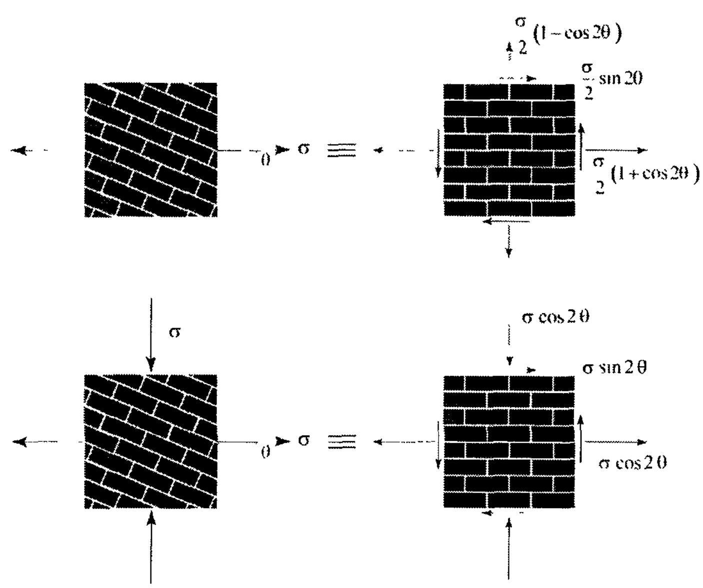

Figure 3.13 – Load pattern for the Page tests for different orientations – Top: Uniaxial loading; Bottom: Biaxial loading (pure shear)

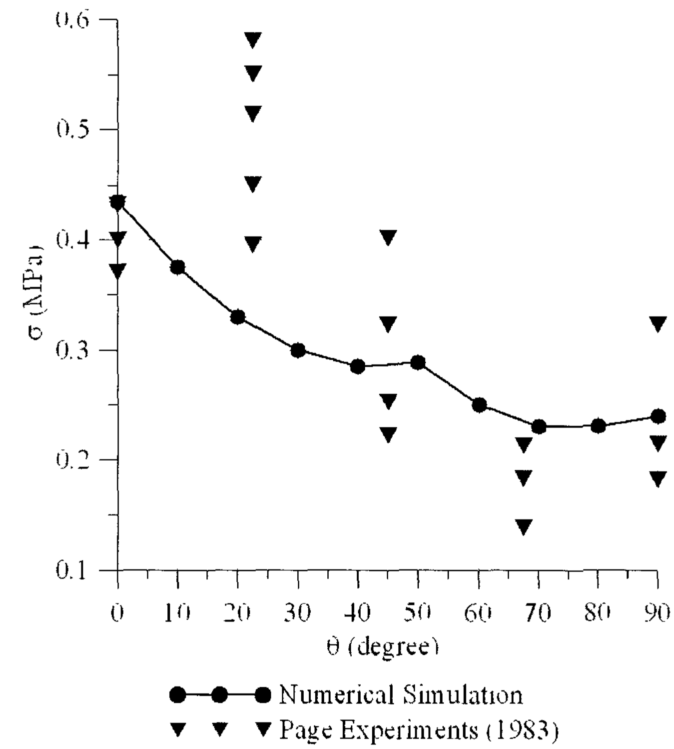

Figure 3.14 – Failure envelope for the Page setup (1983) under uniaxial tension for different orientations of the bed joints

the numerical predictions are in a reasonably good agreement with the mean values of the experimental data. The damage pattern was also monitored and compared with the experimental evidence reported by Page (1983), Figures 3.15 and 3.16. Since for the loading considered here the cracks do not penetrate the bricks, only the mortar joints are depicted in these figures. Once again, the cracked elements are shown in white. The numerical simulations revealed that for $\theta > 50°$ the failure mechanism is governed by Rankine's criterion and the damage is localized in the bed joints. On the other hand, for $\theta < 50°$ the mechanism involves a shear failure along the bed joints (Mohr-Coulomb criterion) accompanied by the tensile fracture of the head joints. These two mechanisms are combined to form zigzag or tooth-like patterns (Figures 3.15, b and c). Figure 3.16 presents the experimental crack pattern recorded for different loading histories (Page, 1983). The predominant failure modes are similar to those predicted numerically.

As mentioned earlier, the assessment of failure load is quite consistent with Page's results, Figure 3.14, except for θ = 22.5° where the finite element simulation underestimates the ultimate strength of the panel by over 30%. This can be due to the fact that, given the small size of the samples, the stress distribution is significantly affected by the constraints imposed along the boundaries. The latter produce additional confinement that alters the stress path and consequently increases the strength of the specimen, particularly in the regime where the dominant failure mode is pressure sensitive (Mohr-Coulomb criterion). It is anticipated that for larger test specimens the results from the experiments would be closer to those obtained from simulations.

Biaxial tension-compression – pure shear

A special case of $\sigma_c/\sigma_t = 1$ is studied here, which is equivalent to pure shear of a specimen with bed joints at θ + 45° with respect to the horizontal axis. The strength characteristic obtained from numerical analysis is presented in Figure 3.17. The results are compared with the best fit to the experimental curves reported by Page (1983) for the

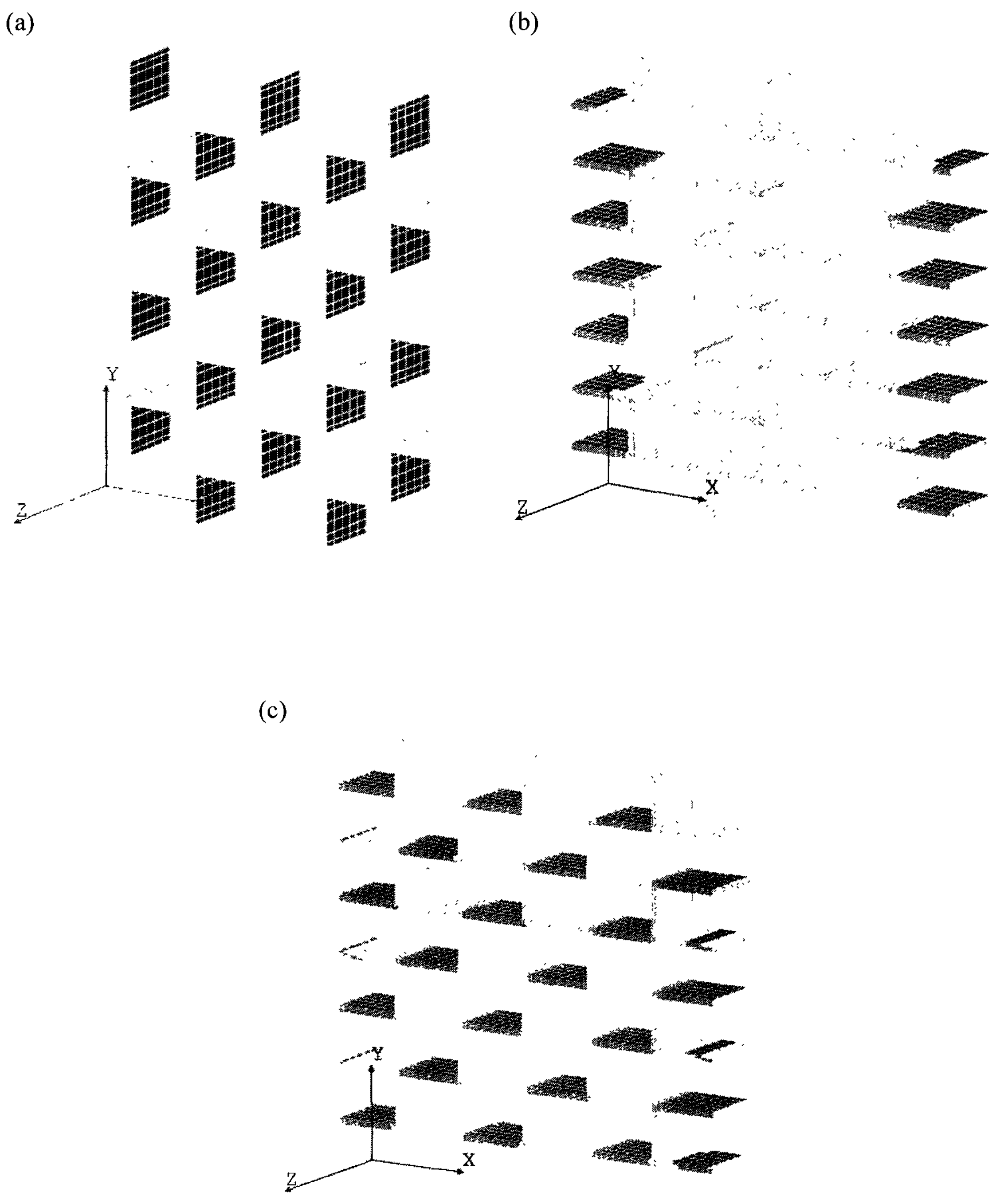

Figure 3.15 – Crack propagation pattern within the mortar joints in page specimens subjected to unixial tension; (a) perpendicular to the bed joints, $\theta = 90°$; (b) perpendicular to the head joints, $\theta = 0°$; and (c) $\theta = 10°$

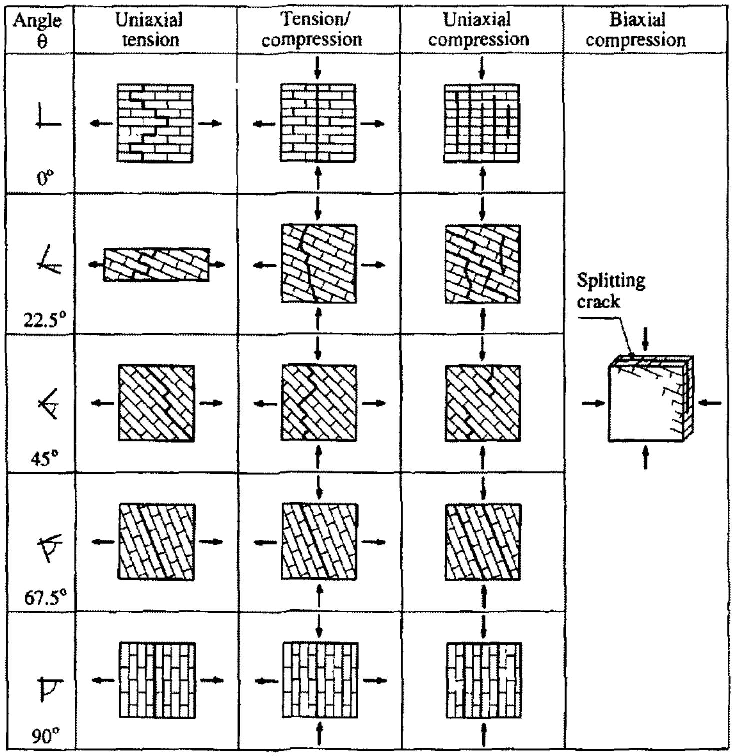

Figure 3.16 – Failure modes within the Page specimens under uniaxial loading (after Dhanasekar et al., 1985)

same loading history. For θ = 0° the failure mode is characterized by the tensile debonding of the head joints and tensile failure of the bricks, forming a vertical crack running through the entire panel, Figure 3.18 (a). This pattern is observed for orientations up to 30°, Figure 3.18 (b). Afterwards, the failure mode switches to a stepped pattern consisting of tensile debonding of the head joints followed immediately by the shear failure along the bed joints. For the orientations beyond 50°, this mechanism is replaced by a failure along the bed joints governed by the Rankine's cut-off criterion. The results

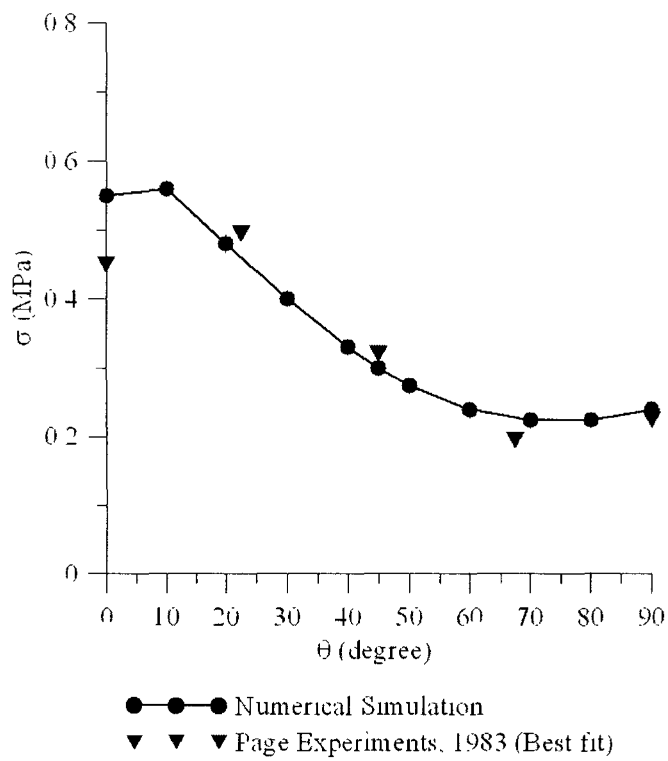

Figure 3.17 – Failure envelope for the Page specimens (1983) subjected to biaxial tension-compression ($\sigma_c / \sigma_t = 1.0$) for different orientations of the bed joints

are, in general, consistent with the experimental evidence presented in Figure 3.16 (Page, 1983). Another aspect that is worth mentioning is the periodicity of the solution for any given orientation. As an example, Figure 3.19 shows the distribution of the principal stresses for $\theta = 10°$. It is evident here that the stress field is periodic within the entire domain, except for the regions adjacent to the boundaries. The same conclusion stems from examining the crack pattern in Figure 3.18 (a). The notion of periodicity of the solution is exploited in the following chapter by introducing the approach based on numerical homogenization.

(a) (b)

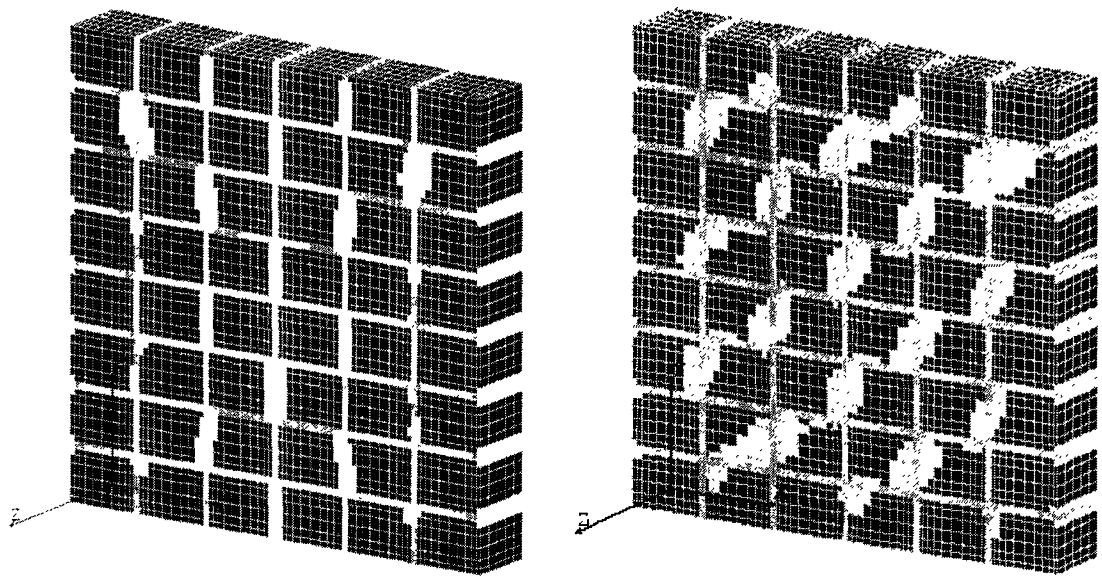

Figure 3.18 – Crack propagation pattern within the page specimens subjected to biaxial tension-compression for (a) $\theta = 0°$; (b) $\theta = 10°$

(a) (b)

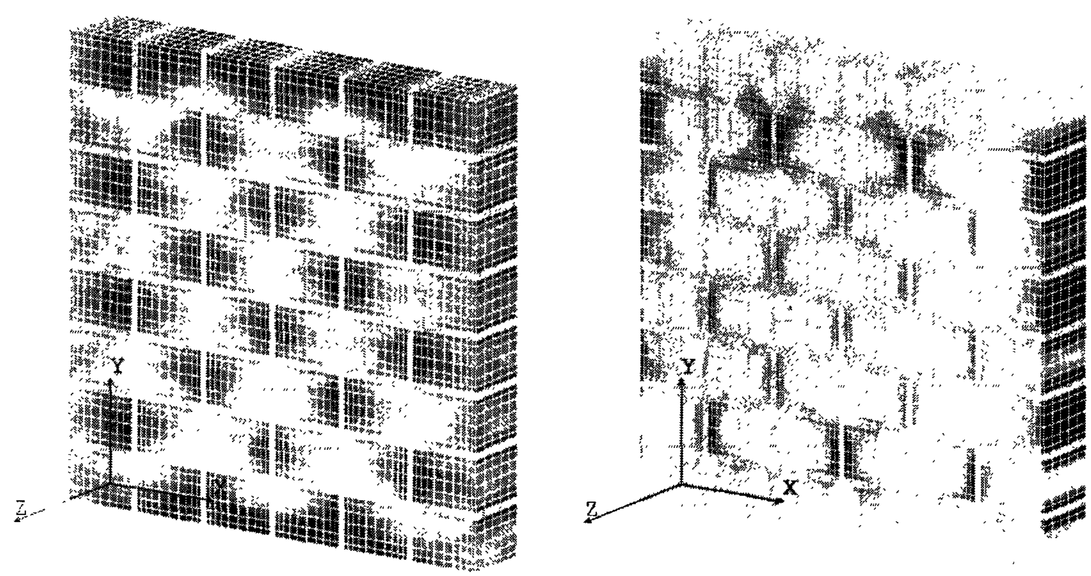

Figure 3.19 – Stress distribution pattern for biaxial tension-compression test for $\theta = 10°$: (a) maximum principal stress; (b) minimum principal stress

3.5. FINAL REMARKS

The constitutive relation developed in the previous chapter was implemented to model some experimental tests reported in the literature. Specifically, Atkinson et al. shear tests (1989), van der Pluijm direct shear tests (1993), and Page biaxial tension-compression tests (1983) were studied. A mesoscopic modeling approach was used, in which the discretization was performed at the level of constituents. The reliability of the developed model was demonstrated by comparing the results of numerical simulations with the experimental data.

CHAPTER 4

CONTINUUM ANALYSIS; HOMOGENIZATION APPROACH

4.1. INTRODUCTION

In the previous chapter a discrete approach was used in which a mesoscale model was constructed and analyzed. Implementing such an approach in the context of real masonry structures, however, is not feasible given the actual dimensions of the problem. Therefore, a more appealing approach is that in which the masonry is considered as a continuum with a strong inherent anisotropy. In general, the identification of properties on the macro scale requires a large number of tests on masonry panels, similar to those conducted by Page (1981, 1983). These tests, however, are expensive and difficult to perform. An attractive alternative is to employ the numerical analysis to generate the data on the directional dependence of strength characteristics of masonry based on properties of constituents. This information can then be explicitly used for the purpose of identification of the continuum approach. In this chapter, a procedure is developed for assessing the strength of brick masonry based on homogenization theory (after Kawa et al., 2007). The approach invokes a lower bound analysis whereby plastically admissible stress fields are constructed in the constituents involved, subject to periodic boundary conditions and static equilibrium requirements. The critical load is obtained by solving a constrained optimization problem. The analysis employs a set of specific loading histories such as axial tension, pure shear and biaxial tension-compression at different orientations of the bed joints. The performance of this approach is verified using numerical homogenization that employs a perfectly plastic formulation. Subsequently, a more sophisticated material model, as outlined in Chapter 2, is used in the context of numerical homogenization to make more accurate predictions of the directional strength characteristics of the brick masonry. In the second part of this chapter, a methodology is outlined for identification of material parameters/functions in a macroscopic failure criterion. Given the latter, a numerical analysis can be carried out on the continuum level. The failure criterion itself is based on the critical plane approach (Pietruszczak & Mróz, 2001; Ushaksaraei & Pietruszczak, 2002). In this approach, the conditions at failure are defined in a local sense, i.e. in terms of traction components acting on a physical plane, and the mathematical representation employs a set of material functions specifying the spatial variation of strength parameters. The approach consists of identifying such an orientation of the critical or localization plane, for which the failure function reaches a maximum.

Finally, a number of numerical simulations are performed aimed at the verification of the performance of the latter methodology in the context of the critical plane approach and the results are compared with the available experimental data.

4.2. HOMOGENIZATION PROCEDURE

As mentioned earlier, the analysis of masonry structures should ideally be conducted at the meso-level, i.e. should incorporate the properties of constituents as well as the details of the architectural arrangement (cf. Chapter 3). However, for large engineering structures, it is virtually impossible to conduct the analysis at this level, even when using the most advanced computer technologies. Given the scale of the problem, some homogenization techniques must be employed. In this section, the strength of a composite has been defined by invoking the notion of a plastically admissible stress state. The latter is a set of macrostress fields for which the microstress tensors do not violate the corresponding failure criteria for all constituents involved. In a composite consisting of two distinct constituents like structural masonry, the plastically admissible macrostress field can be defined as (Suquet, 1987; Lydzba et al., 2003)

$$F\left(\left\langle\sigma_{ij}\right\rangle\right)\leq 0$$
$$\Updownarrow$$
$$\left\langle\sigma_{ij}\right\rangle\in A=\left\{\begin{array}{l}\left\langle\sigma_{ij}\right\rangle \left|\ \forall x,y,z\in V_{RVE}\left\{\begin{array}{l}f_1\left(\sigma_{ij}\left(x,y,z\right)\right)\leq 0\ \forall x,y,z\in V_1\subset V_{RVE}\\ f_2\left(\sigma_{ij}\left(x,y,z\right)\right)\leq 0\ \forall x,y,z\in V_2\subset V_{RVE}\end{array}\right.\right.\\ \wedge\displaystyle\int_{V_{RVE}}\frac{\sigma_{ij}\left(x,y,z\right)}{V_{RVE}}dV=\left\langle\sigma_{ij}\right\rangle\wedge\ \mathrm{div}\sigma_{ij}=0\ \wedge\ \text{periodic B.C.s}\end{array}\right\} \tag{4.1}$$

In this expression, F is the macroscopic failure function, $\langle\sigma_{ij}\rangle$ and σ_{ij} represent the macro and microstress tensors respectively, V_m is the volume occupied by the constituent m (=1,2), $f_m(\sigma_{ij}) \le 0$ is the corresponding local failure function for this constituent and V_{RVE} is the volume of RVE, i.e. the Representative Volume Element.

The above approach, in the context of the limit theorems, gives a lower bound assessment of strength for the given loading conditions. Note that the problem can, in general, be formulated as a constraint optimization problem. The variables here are the respective microstress fields, while the constraints are represented by the failure criteria for constituents, equilibrium requirements and the boundary conditions. For practical purposes, the size of the problem needs to be reduced to a manageable level by postulating, a priori, some idealized stress distributions within the RVE. It should be noted that in this case the solution is not an exact one but represents a lower bound estimate on the critical load.

The Representative Volume Element is defined as the smallest volume that contains all the necessary information at the level of the constituents involved. For masonry structures, the RVE can be selected in a variety of different ways, as indicated in Figure 4.1. Most frequently, the periodic cells *a, b* and *c* are chosen as they are subject to classical stress periodicity conditions, i.e. equality of traction magnitudes on opposite faces of the RVE. These conditions are the direct results of periodicity of the structural arrangement, i.e. the entire structure is obtained here by enforcing periodicity of a unit cell. The RVE marked as *d* employs the same periodicity conditions; it invokes, however, a smaller volume. In this work, the unit cell marked as f has been selected as being most convenient in the context of writing and implementing the optimization equations. The size of the cell is small and the faces are aligned with the principal material triad. In this case, however, the periodicity conditions imposed on the stress field need to be modified in accordance with the pattern with which this cell repeats itself within the entire panel. Referring to the sketch on the right hand side of Figure 4.1, the vertical boundaries are subject to classical periodicity conditions. Along the horizontal boundaries, however, a 'translation' is required. The latter entails the anti-periodicity of the traction vector on pairs B and E, as well as F and C. Note that the periodicity applies, in general, to the in-plane arrangement only, so that the homogenization procedure is restricted to a plane (2D) case.

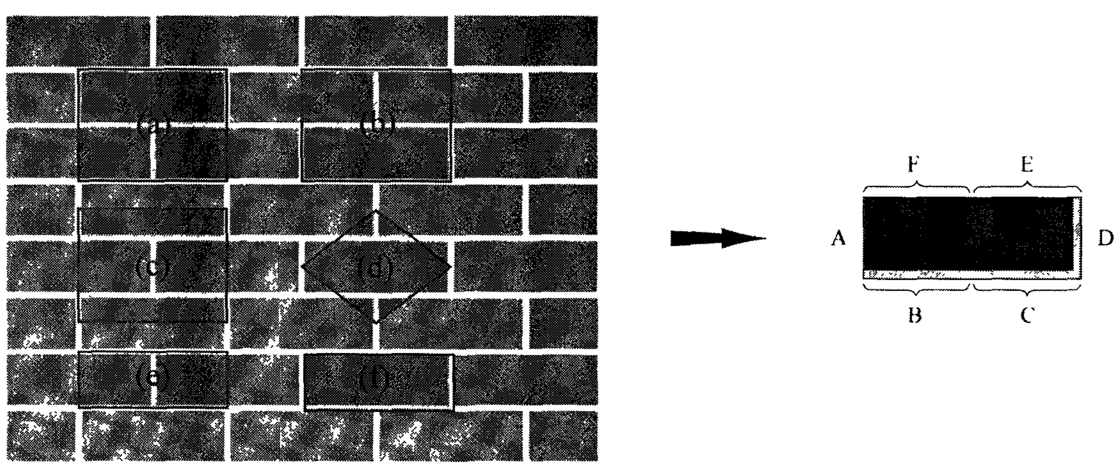

Figure 4.1 – Various options for adopting RVE

For the constituents involved, i.e. brick and mortar, the conditions at failure have been described by implementing a Mohr-Coulomb criterion intercepted by Rankine's cut-off in the tension domain. Denoting by σ_1, σ_2 the in-plane principal stresses, the Mohr-Coulomb failure condition takes the form

$$\begin{aligned} &\frac{1}{2}|\sigma_1 - \sigma_2| \le c\cos\phi - \frac{1}{2}(\sigma_1 + \sigma_2)\sin\phi \\ &\frac{1}{2}|\sigma_1 - \sigma_z| \le c\cos\phi - \frac{1}{2}(\sigma_1 + \sigma_z)\sin\phi \\ &\frac{1}{2}|\sigma_z - \sigma_2| \le c\cos\phi - \frac{1}{2}(\sigma_z + \sigma_2)\sin\phi \end{aligned} \tag{4.2}$$

where ϕ and c represent the angle of internal friction and cohesion, respectively. Here, in order to simplify the problem, a plane stress state was assumed in which the out-of-plane principal stress σ_z was taken to be zero over the entire thickness of the panel. Note that in reality the condition of $\sigma_z = 0$ is enforced only along the vertical stress free boundaries.

The Rankine's cut-off criterion takes the form

$$\sigma_1 \le \sigma_0; \;\; \sigma_2 \le \sigma_0; \;\; \sigma_z \le \sigma_0 \tag{4.3}$$

where σ_0 is the tensile strength.

In order to formulate the optimization problem, one needs to invoke the standard relations defining the principal stress magnitudes, that is

$$\sigma_{1,2}=\frac{\sigma_x+\sigma_y}{2}\pm\sqrt{\left(\frac{\sigma_x-\sigma_y}{2}\right)^2+\sigma_{xy}^2}$$

The latter can be re-arranged in the form

$$\sigma_1+\sigma_2=\sigma_x+\sigma_y\,;\;\sqrt{\left(\frac{\sigma_x-\sigma_y}{2}\right)^2+\sigma_{xy}^2}\le\frac{\sigma_1-\sigma_2}{2} \tag{4.4}$$

Note that replacing the equality by an inequality in the second relation appearing in (4.4) is plastically admissible and it is introduced here in order to ensure the convexity of all the constraints involved. Finally, the formulation of the problem can be completed by noting that the macro/microstress fields must be consistent with each other. For instance, if the macrostress tensor is defined in terms of its principal values $\langle\sigma_1\rangle$ and $\langle\sigma_2\rangle$, with the base vectors at an angle θ with respect to bed joints (Figure 4.2), then the following conditions must be met

$$\begin{aligned}
&\frac{1}{V_{\mathrm{RVE}}}\int_{V_{\mathrm{RVE}}}\sigma_x(x,y)dV=\langle\sigma_1\rangle\cos^2\theta+\langle\sigma_2\rangle\sin^2\theta\\
&\frac{1}{V_{\mathrm{RVE}}}\int_{V_{\mathrm{RVE}}}\sigma_y(x,y)dV=\langle\sigma_1\rangle\sin^2\theta+\langle\sigma_2\rangle\cos^2\theta\\
&\frac{1}{V_{\mathrm{RVE}}}\int_{V_{\mathrm{RVE}}}\sigma_{xy}(x,y)dV=\left(\langle\sigma_1\rangle-\langle\sigma_2\rangle\right)\sin\theta\cos\theta\\
&\frac{1}{V_{\mathrm{RVF}}}\int_{V_{\mathrm{RVE}}}\sigma_z(x,y)dV=0
\end{aligned} \tag{4.5}$$

The Equations (4.2) – (4.5), together with the prescribed boundary conditions, define the constraints of the optimization problem. The solution was obtained in AMPL

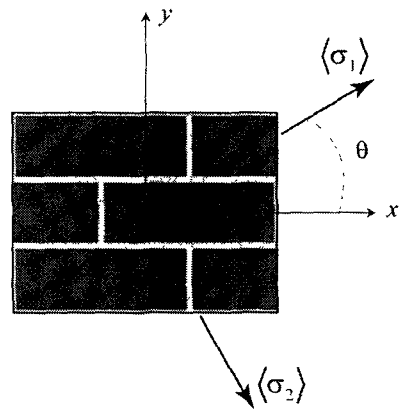

Figure 4.2 – Orientation of principal macrostress axes relative to the bed joints

environment (www.ampl.com) using the IPOPT solver. IPOPT is an open source code which is freely available. It incorporates a primal-dual interior point method for solving general nonlinear programming problems.

In the following section, an example is provided of a lower bound assessment of directional strength characteristics of brick masonry. Different loading configurations are considered, namely axial tension and biaxial tension-compression, and the strength is assessed for different orientations of the bed joints relative to the loading direction. The performance of this approach is then verified by conducting a series of finite element simulations for RVE that incorporate a perfectly plastic formulation with an associated flow rule. Note that in the latter case, since there are no restrictions on the stress distribution, the results represents a close approximation of the analytical solution.

4.3. A LOWER BOUND ASSESSMENT OF STRENGTH PROPERTIES; AN EXAMPLE

As mentioned in the previous chapter, it appears that one of the most comprehensive studies conducted so far on the strength characteristics of masonry is that carried out by Page (1981; 1983). It involved a series of biaxial tension, biaxial compression and biaxial tension-compression tests at different orientations of mortar joints relative to the loading direction. A more detailed description of the tests can be found in Chapter 3. The material parameters used here for the constituents are identical to those employed in Section 3.4 and the key values are listed in Table 3.3.

(i) Uniaxial tension

For uniaxial tension, the preliminary analysis focused on two basic loading configurations that included the tension in the direction normal and parallel to the bed joints, Figure 4.3. In the former case, the governing criterion is the Rankine's cut-off, Equation 4.3. The solution is, in general, consistent with the experimental data; the critical value of macroscopic tensile stress is 0.24MPa, which is the value of σ_0 for the weaker constituent, i.e. the tensile strength of the brick and mortar bond. The associated failure mechanism involves the tensile fracture along both the bed and head joints, Figure 4.3 (a). The latter result is the direct consequence of the assumption that the strength properties of head and bed joints are the same. In reality, however, the tensile strength at the interfaces is lower than that of the mortar, so that the failure occurs along the bed joints (Page, 1983).

The response for tension in the direction along the bed joints is more complex. The failure of head joints is still governed by the Rankine's cut-off criterion. At the same time, however, the transfer of tensile stresses in bricks is accompanied by development of shear in the bed joints. A simplified stress distribution in mortar was adopted for the direct tension tests, which is shown in Figure 4.4. Based on this assumption, the predicted strength for tension along the bed joints is equal to 0.52MPa. The corresponding failure mechanism is consistent with that depicted in Figure 4.3 (b), i.e. it involves a mixed mode associated with failure in tension and shear.

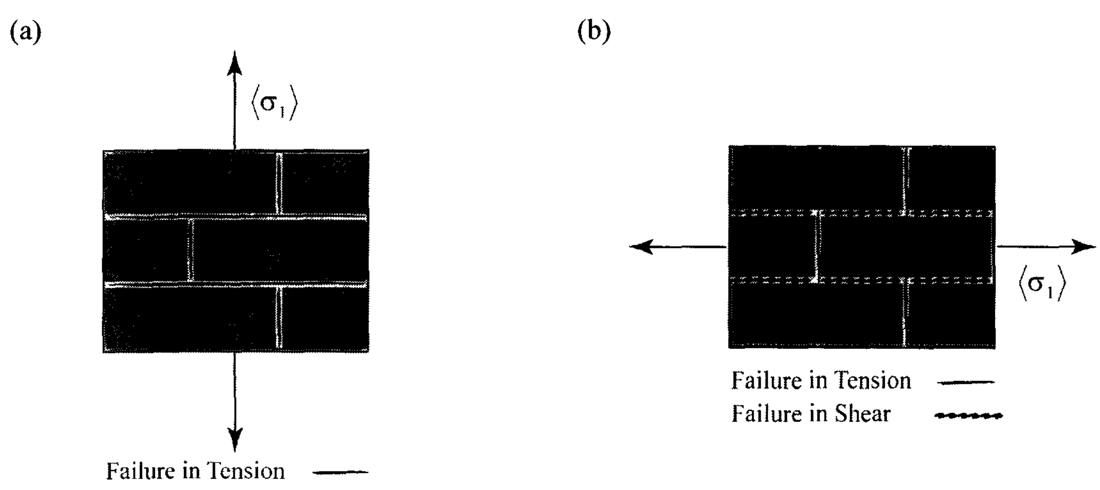

Figure 4.3 – Failure mechanisms in uniaxial tension

Referring to Figure 4.4, the stress field is defined here by specifying tractions at the boundaries of the sub-domains shown and the notation employs the variables that explicitly appear in the formulation of the optimization problem, as defined in Appendix A. Here, XY_1 is the macroscopic shear stress and XY_2 is a local corrector associated with the transfer of normal stress in the brick units. Thus, in each segment the micro-shear stress is equal to the sum of corresponding macro-shear stress and the corrector. Since the volume average of the corrector within the periodic cell is equal to zero, the equality between the macro and the average micro-shear stress is automatically enforced. The assumed stress field is used to examine the conditions at failure in mortar joints only, as these are the weakest links in the system. Along the joints, i.e. in segments D, E and G, the stress field is uniform. This is not the case though in sub-domains F and H. Here, XY_1 and X are uniform, while XY_2 and Y are functions of x and y, respectively. Assuming a linear variation of both XY_2 and Y, it can be shown that for both Rankine's and Mohr-Coulomb criterion the failure function F, as defined by Equations (4.2) and (4.3), may have a critical point within the domain, at which it attains a relative *minimum*. Since both functions are continuous, the absolute *maximum* must occur on the boundaries of these sub-domains. Now, it can also be shown that if F has an extremum along the boundary, it is always a *minimum*. Given this, one can conclude that, for both Rankine's and Mohr-Coulomb criterion, F takes on the maximum value at one of the corners. Thus, the plastic admissibility of the stress field is checked in a discrete manner at all four corners of the sub-domains F and H, respectively. A detailed proof is provided in Appendix B.

Note that the stress distribution in bricks is not explicitly defined, i.e. it is arbitrary provided the equilibrium is enforced. In fact, if the equilibrium is satisfied in a weak (integral) sense for each segment, then for an arbitrary continuous distribution, the actual stress field is statically admissible. Also note that the modified periodicity conditions imply that the horizontal component of the macrostress field depends explicitly on X_3, i.e. the normal stress inside the brick unit, Figure 4.4.

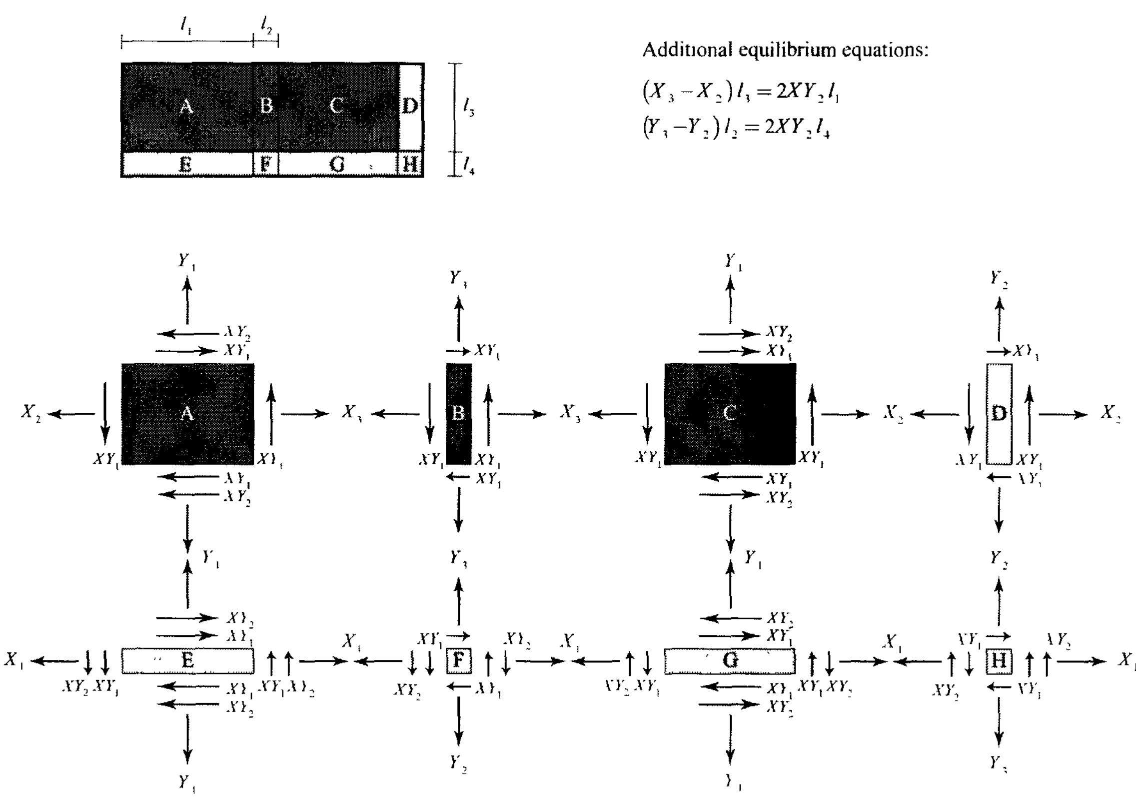

Figure 4.4 – The stress distribution and equilibrium conditions in every segment of the unit cell

It is evident that for $XY_2 = 0$, a simplified stress distribution is obtained in which the stress state at the boundary of each segment is the same. This, in fact, is the configuration that describes the axial tension in the direction normal to the bed joints. Thus, given that the distribution in Figure 4.4 is representative of both configurations shown in Figures 4.3 (a) and 4.3 (b), this stress field has been employed for assessing the strength under an arbitrary orientation of bed joints relative to the loading direction.

(ii) Biaxial tension-compression

The tests simulated in this section involve a combination of tension and compression in two mutually perpendicular directions, as shown in Figure 4.5. Two series of simulations were carried out corresponding to $\xi = 0$ and $\xi = 0.8$. Clearly, the case of $\xi = 0$ corresponds to pure shear at 45°. At the same time, $\xi > 0$ is a combination of pure shear with superimposed hydrostatic pressure of intensity $\xi\sigma$. These two

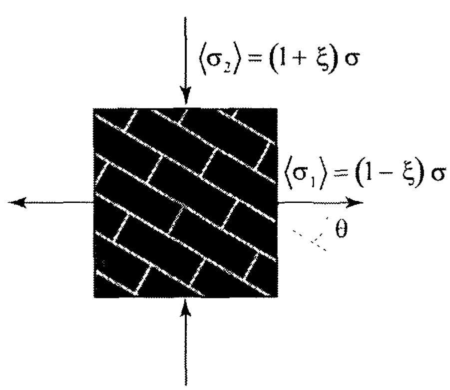

Figure 4.5 – Biaxial tension-compression

configurations, i.e. $\xi = 0$ and $\xi = 0.8$, are employed later in Section 4.5 to identify the material functions/parameters in a macroscopic representation that incorporates the critical plane approach.

For biaxial tests, the stress distribution of Figure 4.4 needs to be modified to yield reasonable estimates. The stress field employed is depicted in Figure 4.6. Here, the normal stresses in the individual segments of the brick unit are modified. In particular, the difference $Y_4 - Y_1$ gives a rotational couple inside the panel; a mechanism that is

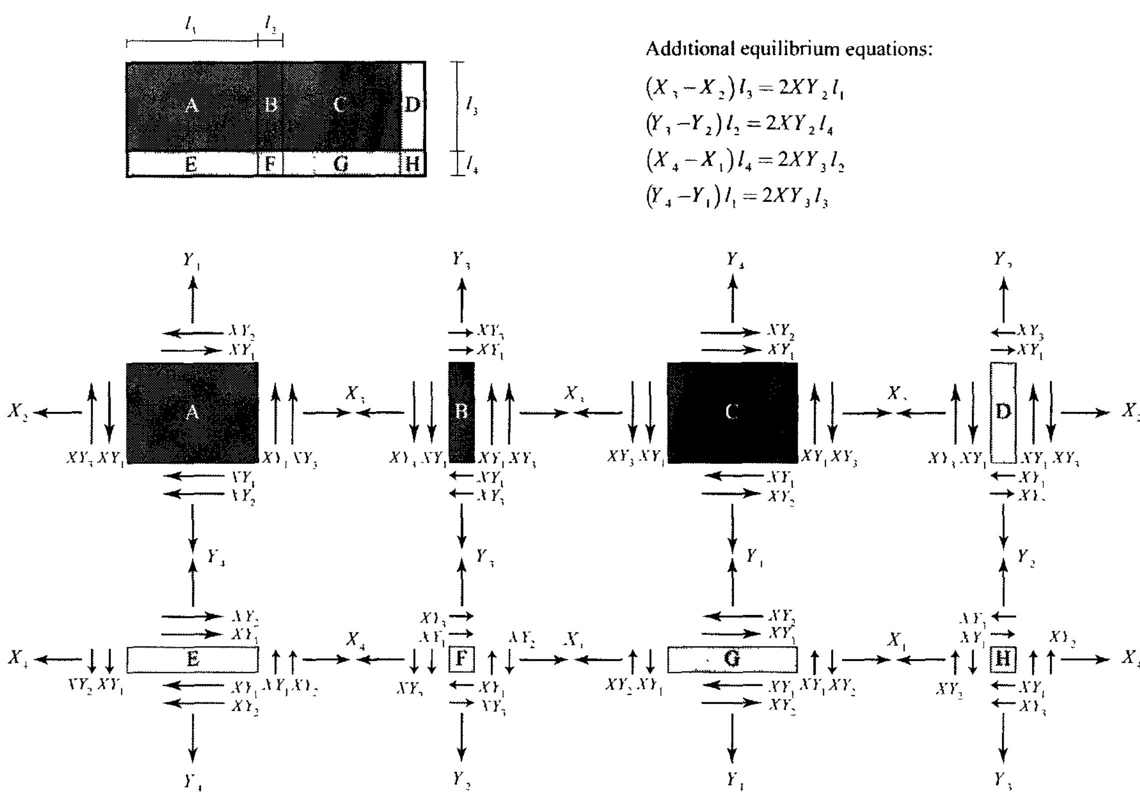

Additional equilibrium equations:

$$(X_3 - X_2)l_3 = 2XY_2 l_1$$
$$(Y_3 - Y_2)l_2 = 2XY_2 l_4$$
$$(X_4 - X_1)l_4 = 2XY_3 l_2$$
$$(Y_4 - Y_1)l_1 = 2XY_3 l_3$$

Figure 4.6 – Modified stress distribution (as compared with Figure 4.4) as employed in biaxial tension-compression tests.

similar to that often used for block structures. In order to equilibrate this couple, an additional shear stress corrector XY_3 has been introduced. Again, the average value of this corrector is zero, so that the equilibrium requirements are enforced.

The optimization was conducted with respect to the parameter σ. The results of all simulations, including those of uniaxial tension, are presented in Figure 4.7. It is noted that, for biaxial tension-compression, the failure mechanism for both the bed and head joints is associated with a pattern involving failure in tension and shear regimes, which is analogous to that depicted in Figure 4.3 (b).

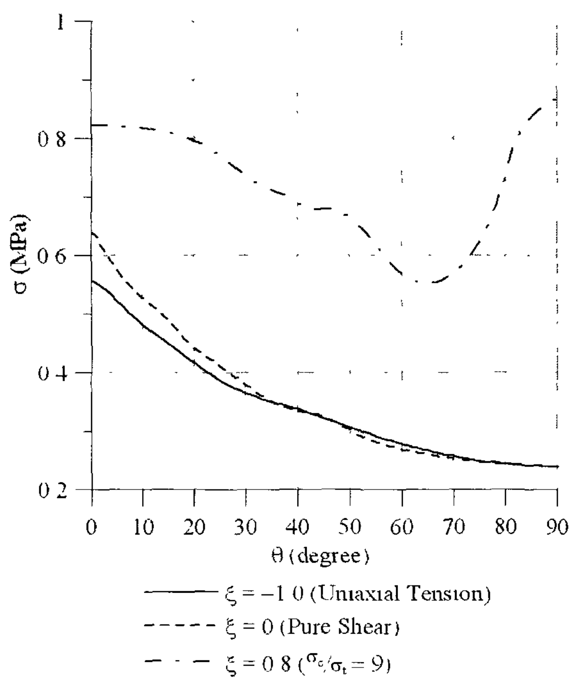

Figure 4.7 – Lower bound assessment for three different loading patterns

4.4. NUMERICAL HOMOGENIZATION; FINITE ELEMENT ANALYSIS

(i) Perfectly plastic formulation: Verification of the lower bound assessment

In this section, a numerical homogenization is employed in order to assess the accuracy of the predictions based on lower bound analysis. In this approach, the RVE was discretized using 3840, 8-noded brick elements, Figure 4.8. A load-controlled scheme was used in the analysis and the ultimate load was identified with the onset of global instability, which in turn was assessed by monitoring the evolution of the safety indicator (Equation 2.39). A non-uniform mesh was employed to account for regions of high deformation gradients. To ensure the compatibility of strain fields along the boundaries of adjacent RVE's, the periodicity conditions were imposed. The latter require that the displacement fields on the opposite in-plane faces of the RVE be the same except for a rigid body translation (cf. Anthoine, 1995). For the adopted RVE these constraints read

$$u_i^D - u_i^A = U_i\,; \quad u_i^E - u_i^B = V_i\,; \quad u_i^F - u_i^C = W_i \tag{4.6}$$

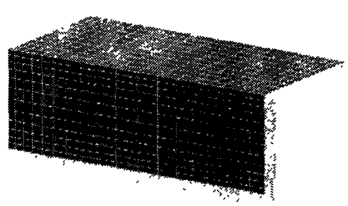

Figure 4.8 – Finite element discretization of adopted RVE

where U_i = const, V_i = const and W_i = const, Figure 4.1.

The numerical analysis has been carried out using COSMOS 2.7 F.E. package with a user-defined material module. The constituents involved were considered to be homogeneous within themselves and were defined as elastic perfectly-plastic. Both have been described using Mohr-Coulomb criteria with the Rankine's cut-off in the tension domain, which is consistent with the formulation in Section 4.3. The loading consisted of uniform traction applied along the boundaries of RVE and the analysis was carried out using an associated flow rule. Clearly, as no a priori assumptions are imposed here on the stress/deformation fields, the results are close to an exact solution for a perfectly-plastic material and consequently can be used as a benchmark to assess the accuracy of the lower bound solution.

The key results for uniaxial tension and biaxial compression-tension, at different orientation of bed joints, are provided in Figures 4.9 (a) – 4.9 (c). Note that all simulations employed the same mesh, Figure 4.8, regardless of the orientation of the microstructure. Instead, for a fixed orientation of the joints, the traction was transformed to the coordinate system associated with the principal material axes.

For uniaxial tension, Figure 4.9 (a), the lower bound estimate is very close to that obtained through numerical homogenization. In this case, all predictions are, in fact, fairly consistent with the experimental data. Note that the experimental scatter is quite significant here. The failure mechanisms, as obtained through numerical homogenization, are shown in Figure 4.10. For tension perpendicular to the bed joints, the damaged zone (shown in white) is confined to the bed joints. For tension normal to the head joints, however, the failure mechanism involves a zigzag pattern, i.e. tensile failure along the head joints, accompanied by the shear failure along the bed joints. The above mechanism is again consistent with the experimental evidence.

For the biaxial tests, the orientation of joints plays a significant role in the development of the damage pattern. When the tensile stress is applied along the bed joints, the initiation of damage is confined to the head joints and later penetrates into the bricks. For the tensile stress perpendicular to the bed joints, the damage starts at the bed joint - brick interface. At the advanced deformation stage, a zigzag pattern is observed for most orientations. Figures 4.9 (b) and 4.9 (c) show a comparison between the strengths characteristics corresponding to $\xi = 0$ (pure shear) and $\xi = 0.8$. As anticipated, the lower bound assessment employing constrained optimization yields a lower value of the ultimate strength. All predictions, however, appear to be reasonably consistent with the available experimental data. In general, it can be asserted that the lower bound assessment for $\xi = 0.8$, which is the least accurate, can be further improved by considering a more complex stress field for this loading configuration.

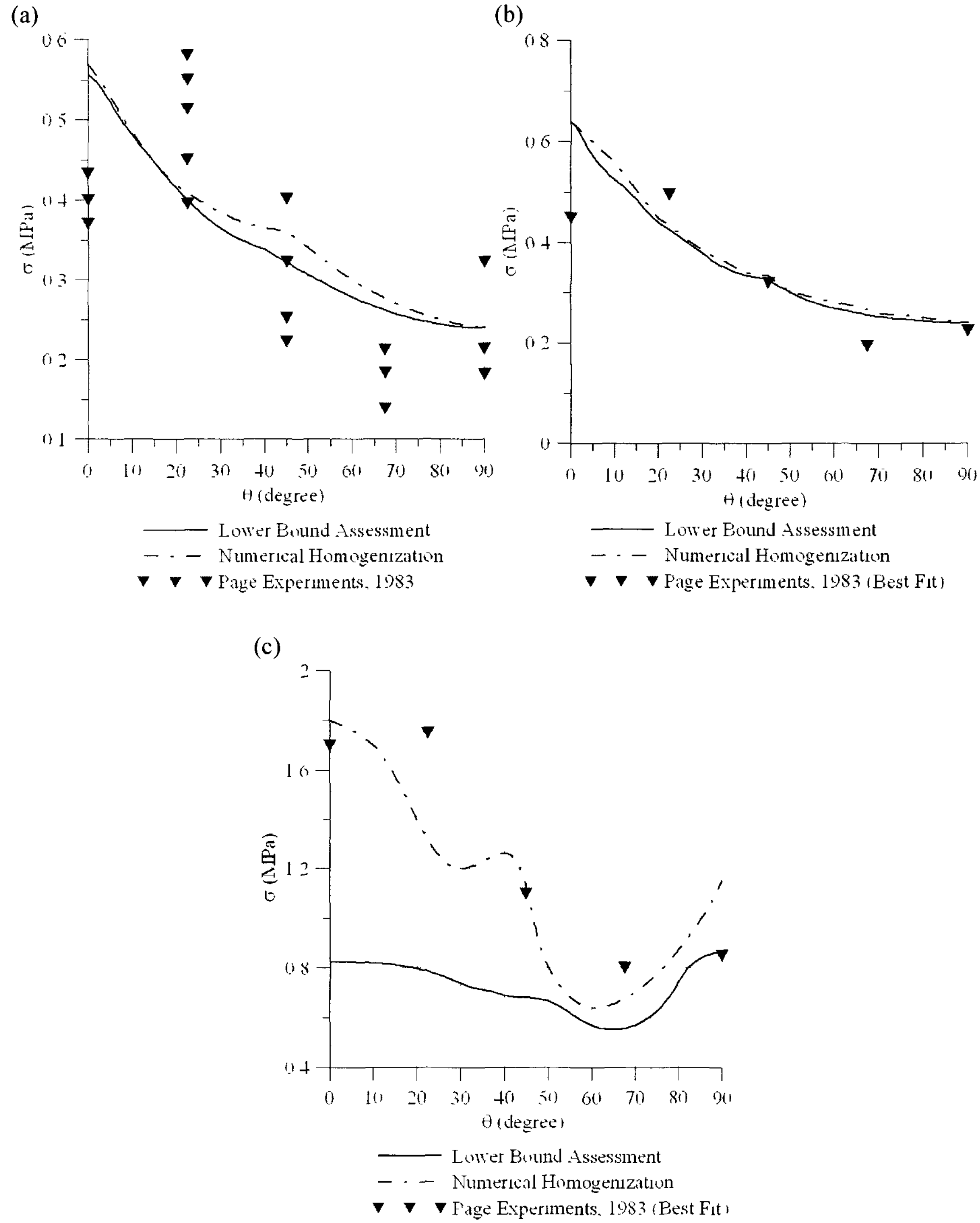

Figure 4.9 – Variation of strength of masonry with the orientation of bed joints; lower bound solution vs. numerical homogenization: (a) Uniaxial tension; (b) Pure shear; (c) Biaxial tension-compression ($\xi = 0.8$)

(a) (b)

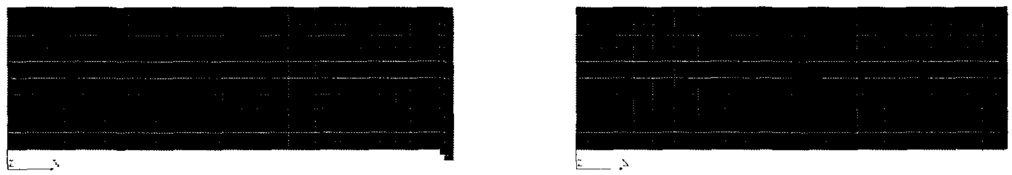

Figure 4.10 – Damage pattern for tension normal to (a) the bed joints; (b) the head joints

(ii) Strain hardening/softening framework with localized deformation

In the preceding section the numerical homogenization with an elastic-perfectly plastic formulation was employed to validate the performance of the lower bound assessment. Even though the results are fairly consistent with the experimental data, it is desirable to seek a more accurate estimate for the orientation dependent characteristics, which can be later used as a reliable tool for deriving the macroscopic material parameters. Hence, a series of simulations were conducted employing the numerical homogenization based on the material model introduced in Chapter 2. The analysis was performed for the same loading configurations as those adopted in the previous section, namely uniaxial tension, biaxial tension-compression with $\xi = 0$ (pure shear), and biaxial tension-compression with $\xi = 0.8$, Figure 4.5. Each analysis was conducted for different orientation of the bed joints. A total number of 11 simulations were carried out for each loading configuration employing 10° intervals. The objective here was two-fold. The first was to compare the solution with estimates obtained from perfectly-plastic formulation. The second was to examine the accuracy of this solution in the context of full-scale analysis conducted in Chapter 3. The material parameters were identical to those given in Section 3.4.

Once again, a load-controlled scheme was employed and the ultimate load was identified based on the evolution of the safety indicator. The results are shown in Figure 4.11, and are compared with those obtained in Sections 4.4.i and 3.4. Figure 4.11 (a) provides the characteristics obtained for the uniaxial tension. It can be seen that the results for RVE are close to those obtained from the full scale tests. The difference stems mainly from the influence of boundary conditions that affect the local stress/strain fields. In fact, the small size of the Page panels makes the effect of the boundaries more pronounced. It is worth mentioning that in general the difference between the full-scale simulations and the RVE will decrease by increasing the size of the test panels. The solution obtained from the perfectly-plastic formulation, however, does not yield an accurate assessment for the ultimate load, especially when loading is perpendicular to the head joints. This is mainly due to the fact that in tension, the response is predominantly brittle and consequently a perfectly plastic formulation does not provide a realistic representation. Figure 4.11 (b) presents the results of simulations pertaining to pure shear. Again, both numerical homogenization and the full-scale tests yield similar assessments of ultimate load. In general, the difference is more pronounced for small θ's. This can again be attributed to the effect of the boundaries for this loading pattern. Finally, the results for $\xi = 0.8$ are given in Figure 4.11 (c). In this case, a fairly consistent trend for both perfectly-plastic and strain hardening/softening formulations is obtained.

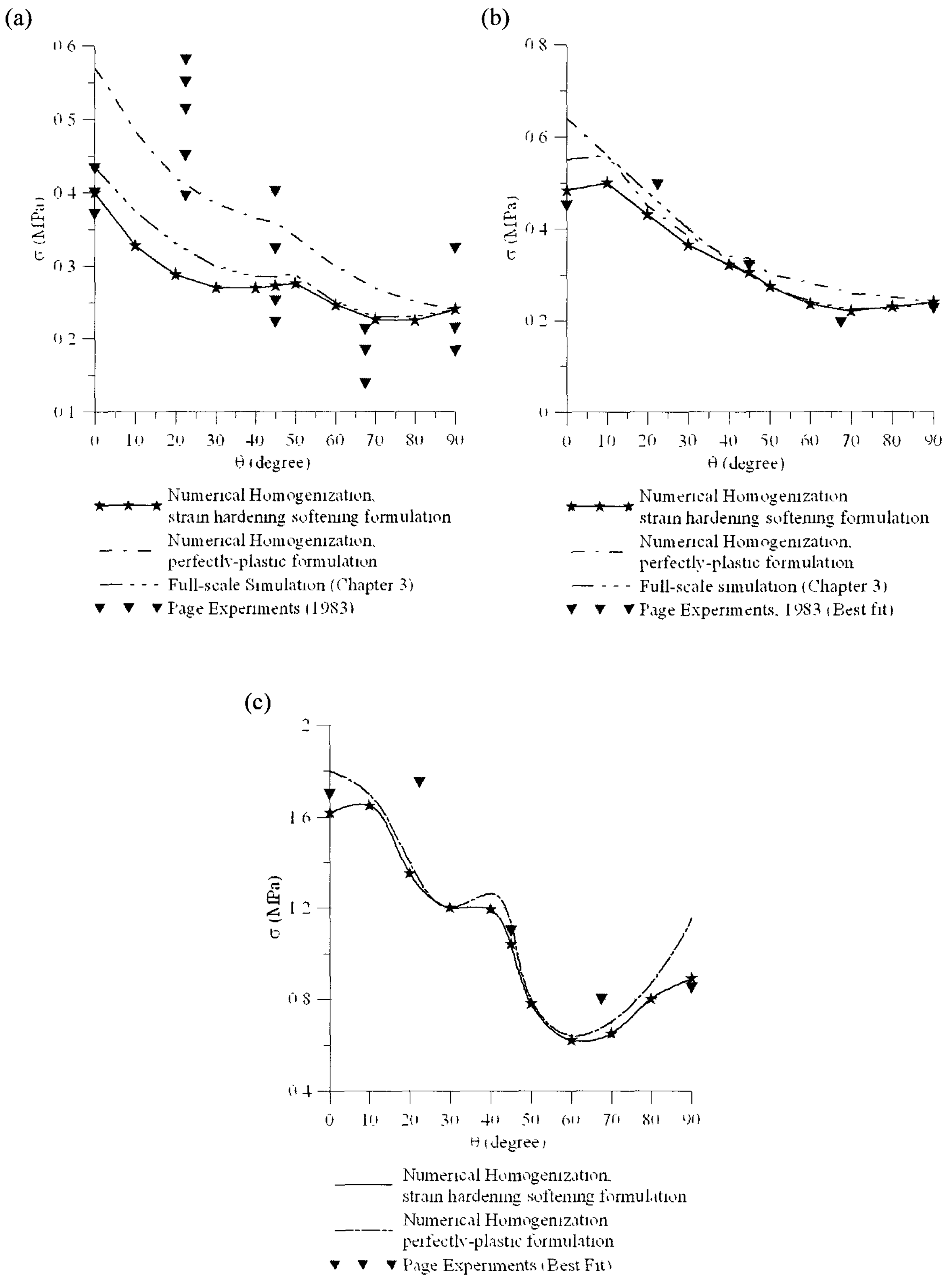

Figure 4.11 – Directional strength characteristics of masonry; (a) Uniaxial tension; (b) Pure shear; (c) Biaxial tension-compression ($\xi = 0.8$)

4.5. CRITICAL PLANE APPROACH; IDENTIFICATION OF MATERIAL PARAMETERS

Implementing a mesoscale approach in the context of real masonry structures is not feasible given the actual dimensions of the problem. Therefore, a more appealing approach is that in which the masonry is considered as a continuum with a strong inherent anisotropy. As mentioned previously, the identification of properties on the macroscale requires a large number of tests on masonry panels that are expensive and difficult to perform. As an alternative the homogenization procedure as outlined in Sections 4.3 and 4.4 may be employed to generate the required data based on properties of constituents. This information can then be explicitly used for the purpose of identification of the continuum approach. In this section, a procedure is outlined for specification of material functions employed in a macroscopic formulation that is based on the critical plane approach (Pietruszczak & Mróz, 2001). Subsequently, the performance of this framework is verified against a broad range of experimental tests conducted by Page.

The critical plane approach consists of specifying the orientation of a critical plane over which the failure function assumes a maximum. In this approach, the conditions at failure are defined in terms of traction components acting on the critical/localization plane. The orientation of this plane is determined by maximizing the failure function using a constrained optimization analysis (cf. Ushaksaraei and

Pietruszczak, 2002). The simplest approach is the one analogous to that employed at mesoscale, i.e. the conditions at failure on an arbitrary plane are defined by the Mohr-Coulomb criterion with the Rankine's cut-off in tension domain. In this case, the failure functions can be written as

$$F_1 = \sigma - \sigma_0, \quad F_2 = |\tau| + \sigma \tan\phi - c \tag{4.7}$$

where τ and σ represent the shear and normal traction on a plane with unit normal n_i, respectively, i.e.

$$\tau = \sigma_{ij} n_i s_j \, ; \; \sigma = \sigma_{ij} n_i n_j \tag{4.8}$$

in which

$$s_i = t_i^s / \|t_i^s\| \, ; \; t_i^s = (\delta_{ij} - n_i n_j) \sigma_{jk} n_k \tag{4.9}$$

and $n_i n_i = 1, s_i s_i = 1, \; n_i s_i = 0$.

The strength parameters, ϕ, c and σ_0 are assumed to be orientation-dependent and are defined as

$$\phi = \phi_1 + \sum_{m=1} \phi_m \left(\Omega_{ij}^{\phi} n_i n_j\right)^m \tag{4.10}$$

$$c = c_1 + \sum_{m=1} c_m \left(\Omega_{ij}^{c} n_i n_j\right)^m \tag{4.11}$$

$$\sigma_0 = \sigma_{0_1} + \sum_{m=1} \sigma_{0_m} \left(\Omega_{ij}^{\sigma_0} n_i n_j\right)^m \tag{4.12}$$

Here, ϕ_m (m = 1, 2, 3 ...), c_m (m = 1, 2, 3 ...), and σ_{0_m} (m = 1, 2, 3 ...) are material constants whereas Ω_{ij} 's represent a set of symmetric traceless tensors which describe the bias in the spatial distribution of strength. ϕ_1, c_1, and σ_{0_1} are the orientation averages of ϕ, c, and σ_0 respectively. In this context, the orientation of the critical plane is defined in terms of maximization of F's (Equation 4.7) with respect to n_i, s_i. The failure is said to take place if

$$F = \max\{\bar{F}_1, \bar{F}_2\} = 0 \tag{4.13}$$

where

$$\bar{F}_1 = \underset{n_i}{\underline{\max}}(\sigma - \sigma_0)\text{, and } \bar{F}_2 = \underset{n_i, s_i}{\underline{\max}}(|\tau| + \sigma \tan\phi - c) \tag{4.14}$$

The solution can be obtained using Lagrange multipliers or any other known technique (e.g. interior point method).

The identification of material constants requires the information on strength characteristics in three distinct configurations. In particular, the results of biaxial tension-compression tests may be employed. In this section the Page data (1981, 1983) is used to demonstrate and verify the performance of the proposed methodology. It is noted that for all tests involving biaxial tension-compression (including uniaxial tension) the failure is confined to the in-plane configuration (Page, 1983). Consequently, for all these cases one can assume, without a loss of generality, that $\Omega_1 = \Omega_3$ which results in $\Omega_2 = -2\Omega_1$. Hence, the only independent parameter in the spectral decomposition of Ω_{ij} is Ω_1.

The evaluation of parameters appearing in the material function σ_0, Equation (4.12), can be carried out using the results of the uniaxial tension, in which the dominant failure locus is the Rankine's cut-off criterion, Equation (4.7). The identification process involves determination of the maximum tensile stress envelope at the onset of failure on each individual plane. This is done by calculating the distribution of normal stress in the case when the panel is subjected to uniaxial tension at different orientation of the bed joints, α, i.e.

$$\sigma_n = \sigma_{ij} n_i n_j = f_t \cos^2(\alpha - \theta) \tag{4.15}$$

In the above equation α represents the angle between the normal to the plane, n_i, and the bed joints, while θ is the orientation of the bed joints with respect to the horizontal *x*-axis. f_t represents the tensile strength of the brick masonry under uniaxial state of stress for any given orientation of θ. For Page tests (1983), this function is constructed by obtaining the best fit to the experimental data given for five different orientations, i.e. 0°, 22.5°, 45°, 67.5° and 90° (Figure 4.12). The envelope of maximum normal stress is obtained by maximizing Equation (4.15) with respect to θ, as depicted in Figures 4.13 and 4.14.

For the Rankine's criterion, the spatial distribution of the tensile strength of the panel must be consistent with the maximum normal stress envelope, Figure 4.14. Noting that

$$\Omega_{ij}^{\sigma_0} n_i n_j = \Omega_1^{\sigma_0} \left(1 - 3\sin^2 \alpha\right) \tag{4.16}$$

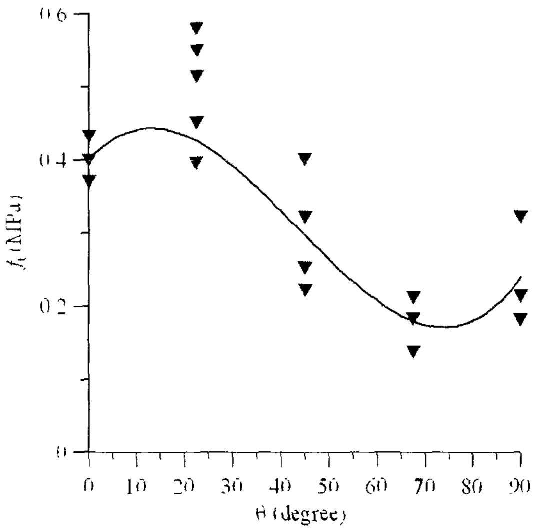

Figure 4.12 – f_t (θ); The best fit approximation to uniaxial tensile strength of brick masonry, Page (1983)

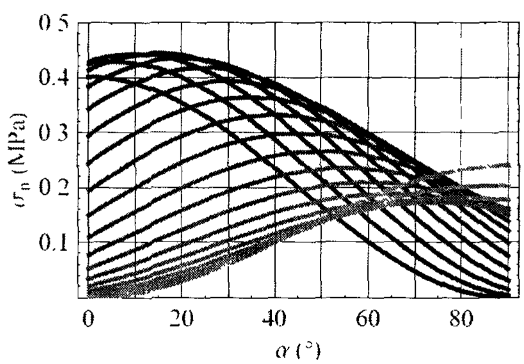

Figure 4.13 – Spatial distribution of normal stress; panel subjected to uniaxial tension at different orientations of bed joints

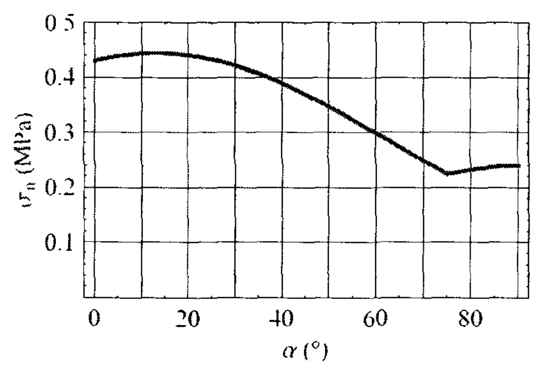

Figure 4.14 – The maximum tensile stress envelope

and assuming the third order approximation for σ_0, Equation (4.12) simplifies to

$$\sigma_0 = \sigma_{0_1}\left(1+\Omega_1^{\sigma_0} - 3\Omega_1^{\sigma_0}\sin^2\alpha\right) + \sigma_{0_2}\left(\Omega_1^{\sigma_0} - 3\Omega_1^{\sigma_0}\sin^2\alpha\right)^2 + \sigma_{0_3}\left(\Omega_1^{\sigma_0} - 3\Omega_1^{\sigma_0}\sin^2\alpha\right)^3 \quad (4.17)$$

At this point, the identification process consists of establishing the best fit approximation to the maximum normal stress envelope using the representation (4.15). The results are shown in Figure 4.15 and correspond to the following set of material parameters

$$\sigma_{0_1} = 0.4089 \text{ MPa},\ \sigma_{0_2} = -0.8804 \text{ MPa},\ \sigma_{0_3} = -1.7177 \text{ MPa, and } \Omega_1^{\sigma_0} = 0.1656$$

Thus, the distribution of the tensile strength is governed by

$$\sigma_0 = 0.3560 + 0.1093\cos 2\alpha - 0.0139\cos 4\alpha - 0.00658\cos 6\alpha \text{ MPa}$$

The polar distribution of this function is depicted in Figure 4.16.

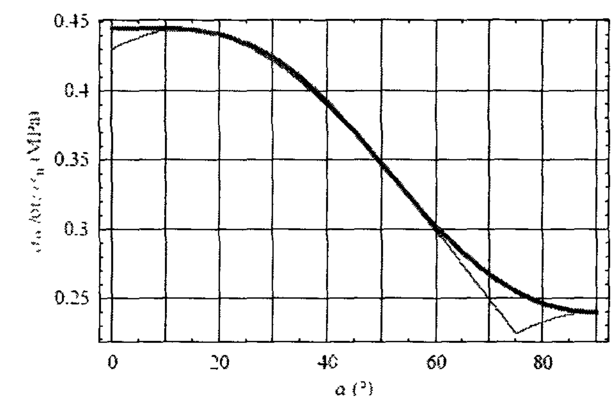

Figure 4.15 – Best fit to the maximum tensile stress envelope

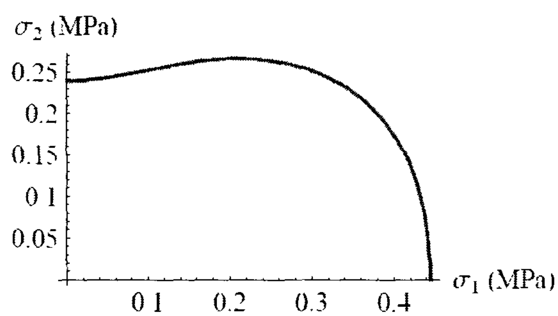

Figure 4.16 – Polar distribution of tensile strength

A conceptually similar approach may be applied for identification of material functions appearing in the Mohr-Coulomb criterion (Equation 4.7). In this case, however, the problem is more complex as it involves specification of a set of parameters, viz. ϕ and c. Here, the experimental data reported by Page for uniaxial compression (1981) and biaxial tension-compression (1983) have been employed to ensure that the Mohr-Coulomb is the active criterion at the onset of failure. The envelope of the maximum normal and shear stresses on each plane is obtained first using the results of tests at different orientation of the bed joints. The spatial distribution of material parameters is obtained by solving the following equations on each arbitrary plane

$$\begin{cases} \underline{\max}_{\theta}\left(\tau_1 + \sigma_1 \tan\phi = c\right) \\ \underline{\max}_{\theta}\left(\tau_2 + \sigma_2 \tan\phi = c\right) \end{cases} \tag{4.18}$$

where $\{\tau_1, \sigma_1\}$ and $\{\tau_2, \sigma_2\}$ represent the shear and normal stresses on the plane for the panel subjected to a uniaxial compression and pure shear, respectively. The individual traction components can be obtained using the following expressions

$$\begin{array}{ll} \tau_1 = f_c \sin(\alpha-\theta)\cos(\alpha-\theta); & \sigma_1 = f_c \sin^2(\alpha-\theta) \\ \tau_2 = \tau_u \sin 2(\alpha-\theta); & \sigma_2 = \tau_u \cos 2(\alpha-\theta) \end{array} \tag{4.19}$$

in which τ_u represents the ultimate strength for the pure shear, $\xi = 0$ (Figure 4.5). Having identified the distribution of $\tan\phi$, one can obtain the distribution of c using either one of the equations in (4.18). Again, for the sake of numerical representation, τ_u and f_c are defined as a function of θ by the obtaining the best fit to the experimental data reported by Page (1981, 1983).

Given the information above, the required material parameters can now be obtained by establishing the best fit approximation to the corresponding ideal distributions by employing the material functions ϕ and c (Equations 4.10, 4.11). Given the irregularity of the ideal function for ϕ, a 6^{th} order polynomial is assumed for approximating the distribution of the function. In this case, the following material parameters are identified

$$\phi_1 = 51.3°,\ \phi_2 = 2.6778\times10^6,\ \phi_3 = -7.8798\times10^8,\ \phi_4 = -2.5743\times10^{11},$$
$$\phi_5 = 1.2709\times10^{14},\ \phi_6 = -1.2701\times10^{16},\ \Omega_1^\phi = -0.002649$$

Thus, the material function ϕ $(°)$ is defined as

$$\phi = 55.36 - 1.020\cos 2\alpha + 1.445\cos 4\alpha - 0.0585\cos 6\alpha$$
$$-1.583\cos 8\alpha - 1.619\cos 10\alpha - 1.562\cos 12\alpha$$

For approximating the distribution of c, it is sufficient to employ a third degree polynomial. Adopting the same procedure as that outlined above, the following parameters are identified for the equivalent cohesion

$$c_1 = 0.908 \text{ MPa} \quad c_2 = -1.491 \text{ MPa} \quad c_3 = 14.45 \text{ MPa} \quad \Omega_1^c = 0.105$$

so that,

$$c = 0.806614 + 0.230162\cos 2\alpha - 0.0471571\cos 4\alpha + 0.014266\cos 6\alpha \ \ (\text{MPa})$$

Figure 4.17 shows the spatial distribution of material functions based on the identified set of parameters vs. their ideal distributions. Also, the polar distribution of these functions is shown in Figure 4.18.

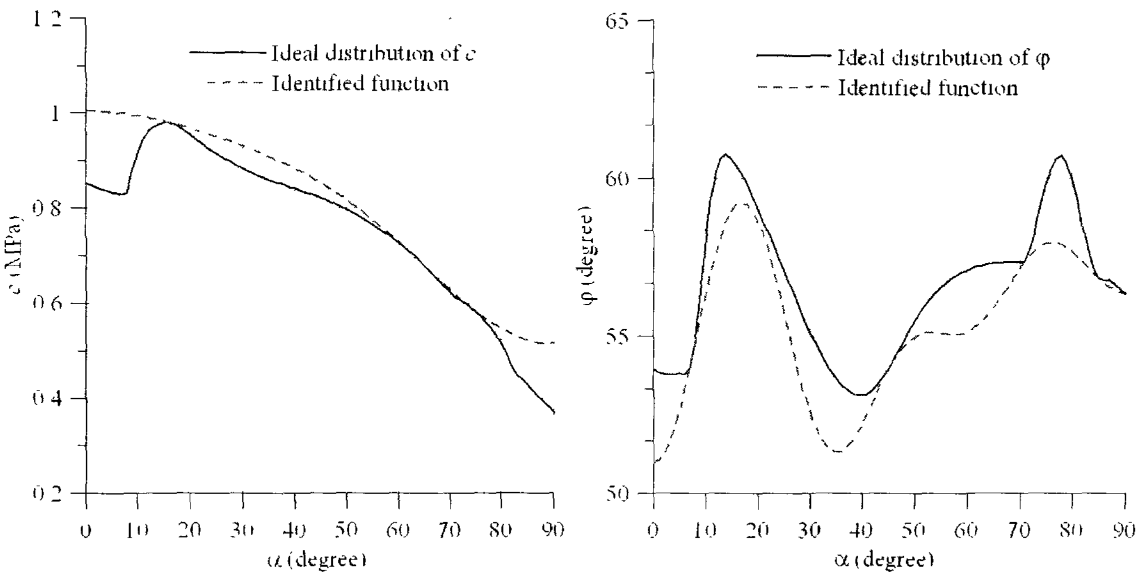

Figure 4.17 – Ideal distributions of c and ϕ vs. the identified functions

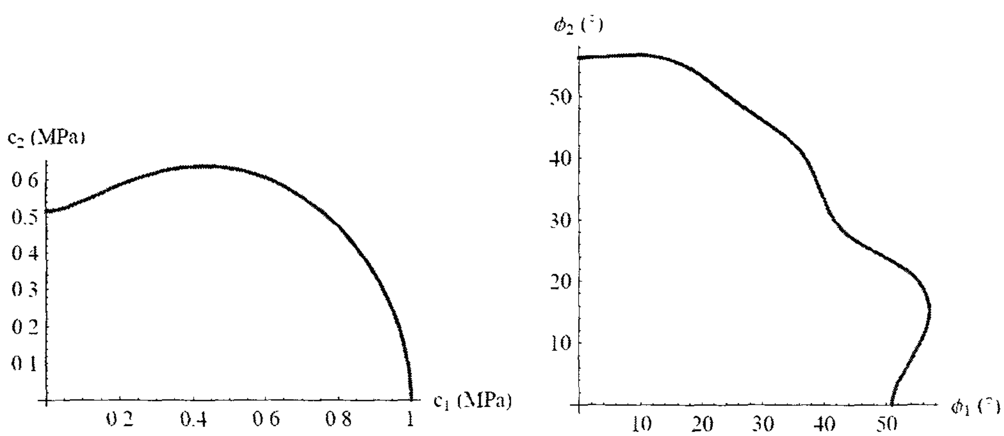

Figure 4.18 – Polar distribution of c and ϕ

4.6. VERIFICATION OF THE MACROSCOPIC FORMULATION

In this section, the material functions derived in Section 4.5 are employed to predict the directional strength characteristics of brick masonry subjected to different loading histories, using the Critical Plane Approach (CPA). In particular, the performance of the masonry panel under uniaxial tension, pure shear and uniaxial compression is examined for different orientation of the bed joints. The results of numerical simulations are shown in Figure 4.19 and are compared with the experimental data reported by Page (1981 and 1983). It can be seen that the results obtained from CPA are in a fairly good agreement with the experimental data. For all loading cases considered here, the orientation of the critical plane has also been established and the results are depicted in Figure 4.20. Figure 4.20 (a) shows the orientation of the macrocrack as a function of orientation of bed joints for the uniaxial tension. In this case, for tension perpendicular to the head joints the macrocrack is almost perpendicular to the bed joints, which at a micro-scale is consistent with a tooth-like pattern along the head and bed joints. For $\theta > 10°$, the predicted orientation can be interpreted as a zigzag pattern. Finally, for $\theta > 40°$ the macrocrack is aligned with the bed joints. The latter is equivalent to the tensile debonding along the bed joints. The results, are again in good agreement with the experimental observation (Page, 1983). An almost identical pattern is observed for pure shear, Figure 4.20 (b). In this case, the failure mechanism changes to tensile debonding along the bed joints at around $\theta = 50°$. Finally, the orientation of the localization plane for uniaxial compression is shown in Figure 4.20 (c). In general, the results are, once more, consistent with the experimental findings. However, for the compression perpendicular to the bed joints the predictions are slightly different from the expected pattern (i.e. along the bed joints). In this case, the obtained mechanism mimics a pattern through the bed joints, occasionally running through a head joint. This can be a consequence of the rather significant difference between the identified function for ϕ and its ideal distribution at that vicinity (Figure 4.17). Higher order approximations can alleviate this problem.

Finally, an extensive set of simulations has been carried out aiming at establishing the macroscopic failure envelopes in biaxial tension-compression for a number of discrete orientations of the bed joints, viz. 0^o, 22.5^o, 45^o, 67.5^o and 90^o, respectively. The results, which are presented in Figure 4.21, indicate a fairly good agreement with the experimental data.

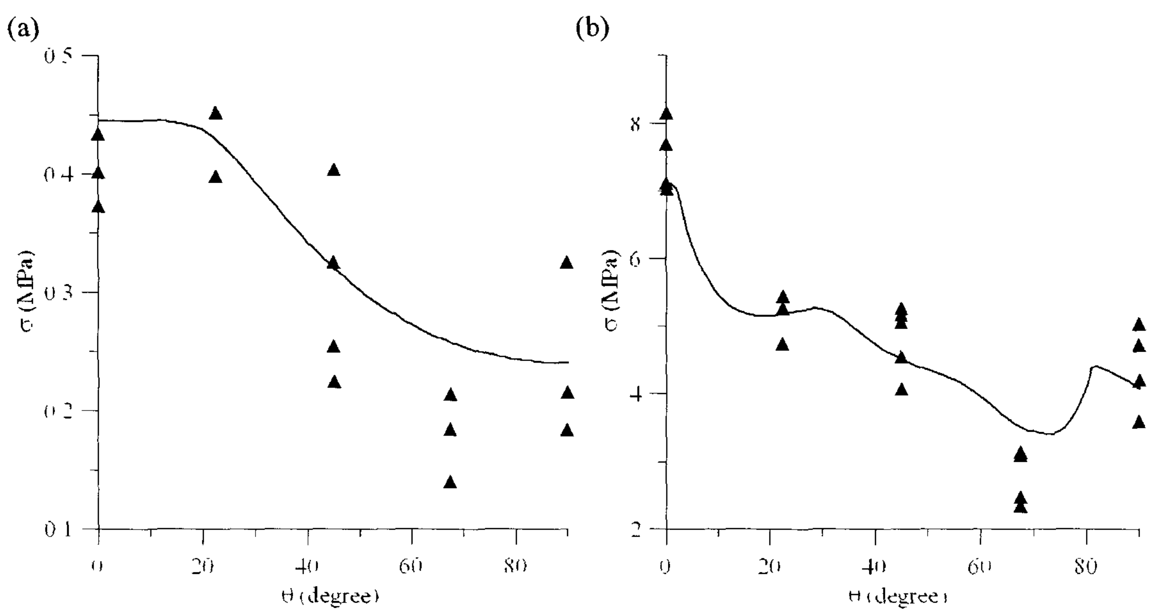

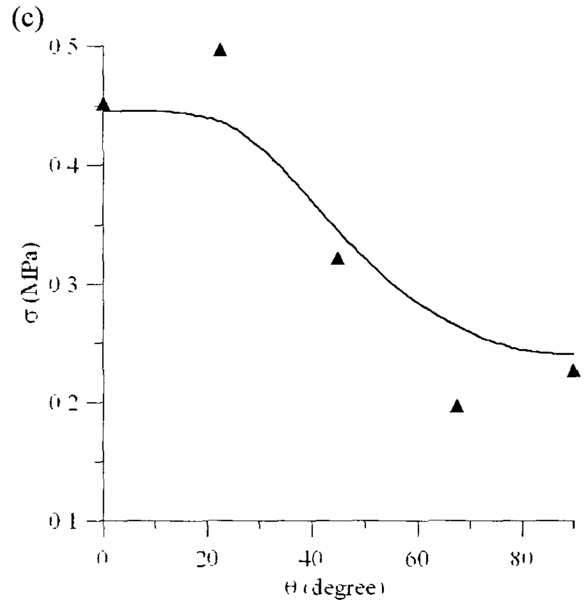

Figure 4.19 – The simulations of (a) Uniaxial tension; (b) Uniaxial compression; and (c) Pure shear tests conducted by Page (1981, 1983) on samples at different orientation of bed joints

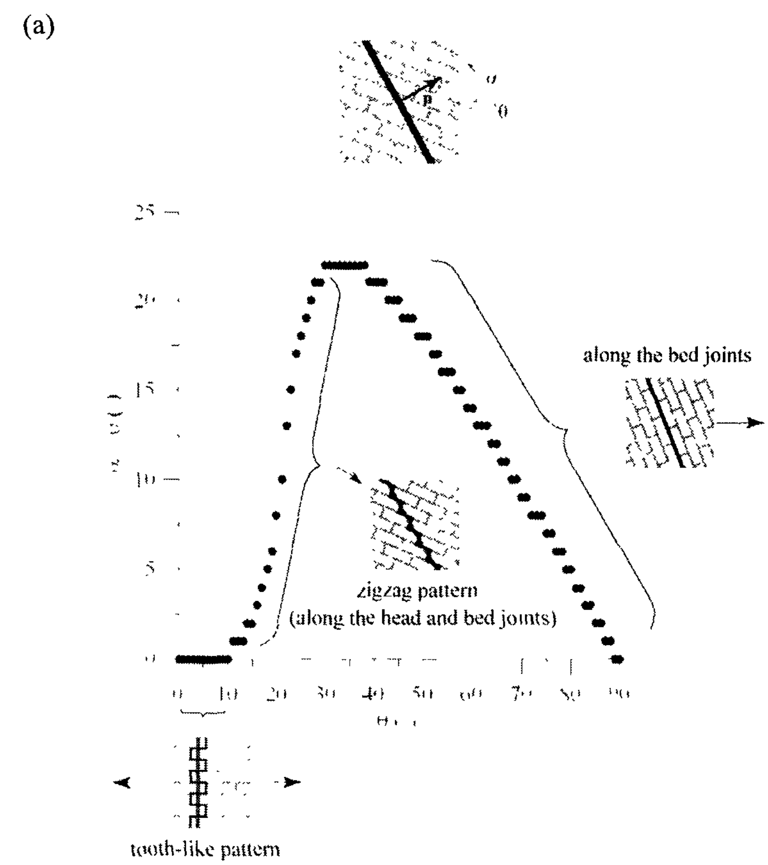

(b)

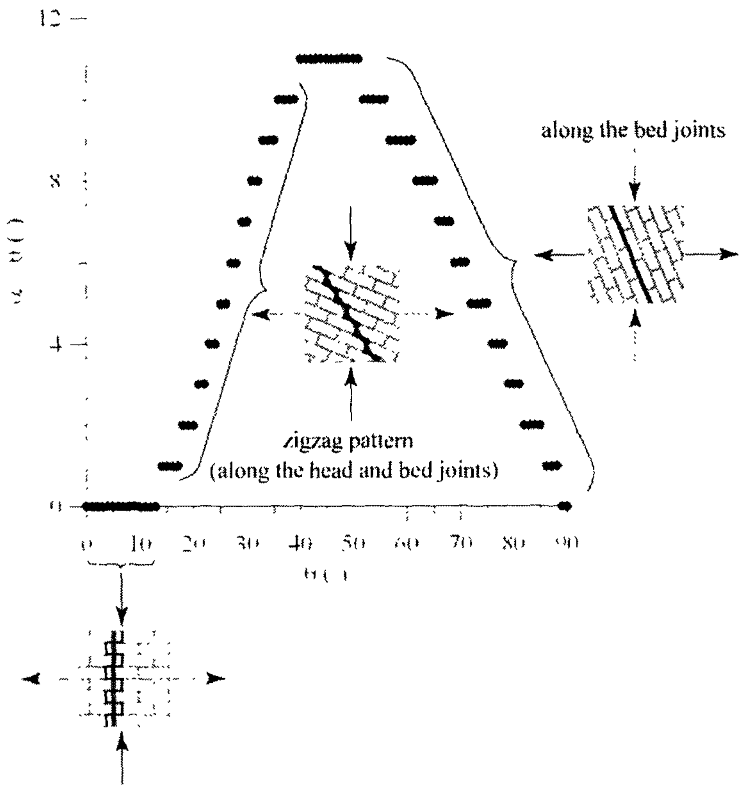

(c)

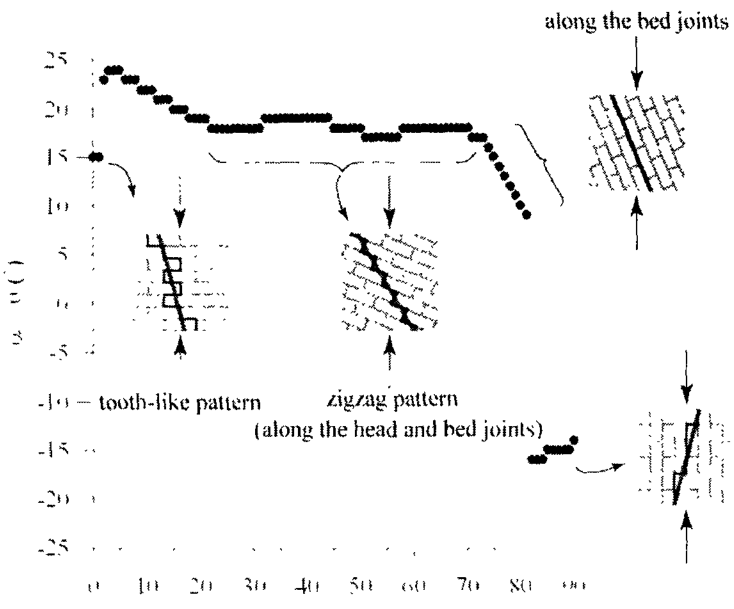

Figure 4.20 – Orientation of macrocracks w.r.t. the x-axis: (a) Uniaxial tension; (b) Pure shear; and (c) Uniaxial compression

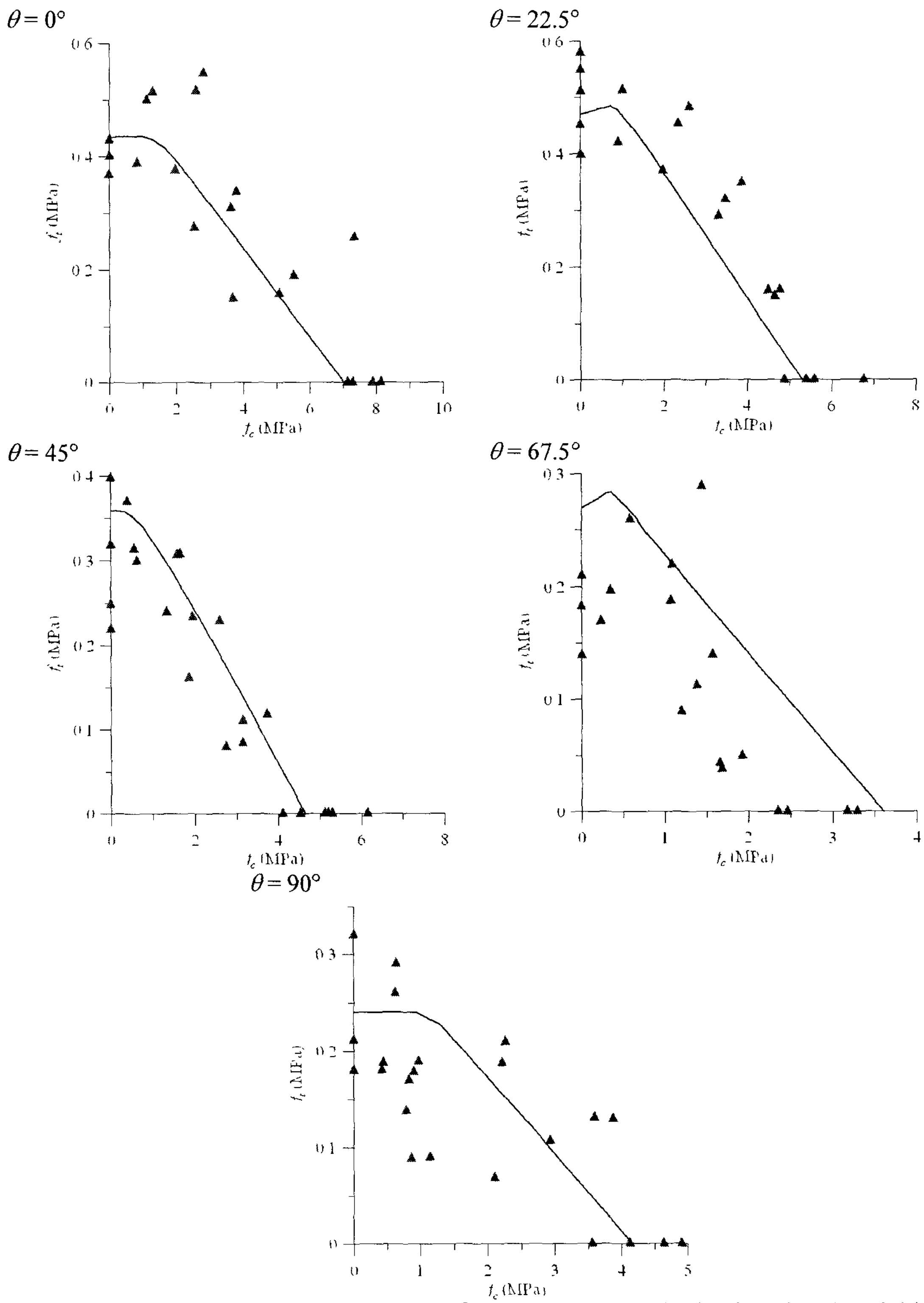

Figure 4.21 – Biaxial tension-compression failure surface for the brickwork using Critical Plane Approach and the identified macromodel

4.7. FINAL REMARKS

In this chapter a methodology was developed for estimating the strength of brick masonry based on homogenization theory. The approach involved a lower bound analysis whereby a plastically admissible microstress field was assumed in the constituents involved. The critical load was obtained by solving a constrained optimization problem. The performance of the proposed approach was verified against numerical solutions based on finite element analysis. The numerical homogenization was carried out for a representative elementary volume, subject to periodic boundary conditions, and employed a perfectly plastic formulation with an associated flow rule. In addition, the same RVE was analyzed using a more accurate material model. The constitutive model developed in Chapter 2 was employed for this purpose. Consequently, a more accurate description of the directional strength characteristics of the brick masonry was obtained.

In the second part of this study, a macroscopic failure criterion was formulated based on the critical plane approach. A procedure for identification of material functions was outlined and a quantitative verification of this approach was carried out based on experimental data of Page (1981, 1983). The verification employed a broad range of loading configurations involving biaxial compression-tension at different orientation of bed joints relative to the loading direction. The results proved to be quite consistent with the experimental data.

The general methodology advocated in this chapter is to employ the homogenization procedure to generate the data on the directional dependence of strength characteristics of masonry based on properties of constituents. Given this data, the macroscopic material functions appearing in the continuum formulation can then be identified. Note that in this approach the only experimental information required is that on isotropic strength properties of constituents, which can be obtained from standard material tests.

CHAPTER 5

CONCLUSIONS AND RECOMMENDATIONS

5.1. CONCLUSIONS

A realistic analysis of masonry structures requires advanced nonlinear models, at both micro and macro levels. While small scale tests can be easily modeled using a meso-level approach, the analysis of real masonry structures needs to be performed by incorporating appropriate homogenization techniques. In the latter case, an extension to non-linear analysis can be achieved by introducing a suitably defined macroscopic failure criterion (e.g., Pietruszczak and Mróz, 2001; Pietruszczak and Ushaksaraei, 2003). A reliable model capable of capturing the anisotropic response and the corresponding failure modes requires the introduction of a set of orientation-dependent parameters. Ideally, these parameters should be identified through a series of carefully designed experimental tests. Given the difficulties associated with conducting such an experimental program, some alternative methodologies should be explored. One of the most promising approaches here is the implementation of meso-scale modeling to generate the data required at the macroscale. In this case, the only experimental information needed is that on isotropic properties of constituents, which can be obtained from standard material tests.

The objective of the first part of the study was to introduce an advanced constitutive model which is capable of addressing all distinct stages of deformation in brick and mortar, i.e. elastic, elastoplastic and softening. This constitutive model was then implemented in COSMOS 2.7 FE package. After its verification, which was accomplished via a series of simple boundary value problems, a series of experimental tests reported in the literature were studied using a mesoscopic modeling strategy. That included Atkinson et al. (1989) and van der Pluijm (1993) shear tests. The focus here was mainly on examining the degree of accuracy of the model in predicting the critical load recorded in the aforementioned tests. The latter study was followed by modeling of the directional strength characteristics of brick masonry using the experimental data of Page (1983) from a series of full-scale tests. Two distinct loading configurations, namely uniaxial tension and pure shear, were considered. For Atkinson et al. (1989) and van der Pluijm (1993) tests, the results of numerical simulations were quite consistent with the experimental data, thereby providing a degree of confidence in the predictive abilities of the constitutive model. For Page (1983) tests, given the significant scatter in the experimental results, the numerical simulations were also quite satisfactory in both qualitative (viz. the basic trends in characteristics) and quantitative sense.

In the second part of this study, a methodology was developed for estimating the strength of brick masonry based on homogenization theory. The approach involved a lower bound analysis whereby a plastically admissible microstress field was assumed in the constituents involved. The critical load was obtained by solving a constrained optimization problem. The performance of the proposed approach was verified against numerical solutions based on finite element analysis. The numerical homogenization was carried out for a representative elementary volume, subject to periodic boundary conditions, and employed a perfectly plastic formulation with an associated flow rule. The latter was used in an attempt to assess the accuracy of the solution based on lower bound analysis. For simple loading configurations such as uniaxial tension or pure shear at different orientations of bed joints, the results based on lower bound assessment were in good agreement with those obtained using numerical homogenization. This is significant, considering the amount of computational time that can be saved using the lower bound approach. For more complex loading patterns, however, such as biaxial tension-compression, the lower bound estimates were not satisfactory. It was concluded that in order to obtain a better representation, more elaborate stress distribution in the constituents of RVE is required.

Later in this part of the thesis, the same RVE was analyzed using a more accurate material description, i.e. the constitutive model developed in Chapter 2. As a result, a more accurate description of the directional strength characteristics of the brick masonry was obtained. The latter results were then compared with those obtained from the full-scale tests as well as the perfectly plastic formulation. In general, the methodology advocated here was to employ the homogenization procedure to generate the data on the directional dependence of strength characteristics of masonry based on properties of constituents. This data can then be used to identify the material functions appearing in any specific continuum formulation.

In the last part of this study, a macroscopic failure criterion was formulated based on the critical plane approach. A procedure for identification of material functions was outlined and a quantitative verification of this approach was carried out based on the experimental data of Page (1981, 1983). The verification employed a broad range of loading configurations involving biaxial tension-compression at different orientation of the bed joints relative to the loading direction, and involved the prediction of both critical load and macroscopic failure patterns. The results proved to be quite consistent with the experimental data.

Based on this study, the following general conclusions can be made:

- Numerical analysis at the mesoscale is efficient and accurate in terms of analyzing small-scale masonry structures. Such an approach also provides an attractive alternative to experimental tests for estimating the anisotropic strength properties of masonry panels based on properties of its constituents. This approach requires an adequate constitutive model in which all major failure mechanisms are accounted for. In this context, the constitutive relation employed in this work proved to be quite reliable in terms of both, the ultimate load assessment and the predicted failure patterns.

- In terms of estimating the macroscopic properties, the most efficient strategy is the one that exploits the periodicity conditions, viz. homogenization. The most straightforward approach is perhaps the limit analysis that can be employed to obtain simple approximations of the critical load. A more rigorous approach, which is based on numerical homogenization, leads to quite satisfactory predictions of the macroscopic characteristics, both in terms of the ultimate load and the failure patterns. In general, the lower bound assessment provides a fast and reliable method for obtaining the directional strength properties under simple loading conditions. However, for more complicated loading configurations this methodology yields too conservative assessments.

- An optimization approach can be used as an efficient tool for a systematic identification of the set of material parameters/functions appearing in a macro model. This was illustrated using the experimental results of Page (1983) that were employed to verify the performance of a Critical Plane framework. It was shown that parameters identified using the advocated methodology yield satisfactory predictions of the strength characteristics in a broad range of loading conditions and orientation of the microstructure of brick masonry.

5.2. RECOMMENDATIONS FOR FUTURE WORK

In this research various methodologies were introduced and verified which can be used as an effective tool when dealing with analysis of masonry structures. Based on the current work, some key recommendations for the future research are outlined.

1. A properly structured experimental program is required to identify the isotropic material properties at the level of constituents, i.e. brick and mortar. This requires a series of tests aimed at specification of strength parameters such as ϕ and c. Also, for an accurate description of deformation characteristics, a series of tests needs to be conducted to identify the deformation related parameters such as A and η_c, as well as the softening parameters.

2. The verification of the numerical model can be enriched by conducting a series of full scale experimental tests, aimed at specifying the directional characteristics of the brick masonry.

3. Although the limit analysis proves to be both reasonable and promising for simple loadings, such as uniaxial tension or pure shear, further improvements seems to be necessary for obtaining satisfactory results under complex loading. This can be achieved by introducing a better approximation for the assumed stress field.

4. The methodology introduced for the identification of material parameters/ functions can be extended to out-of-plane configuration. A series of 3-D numerical tests can be carried out in order to identify the relevant parameters, which are necessary for a reliable prediction of strength characteristics under compression-compression loading.

5. The proposed methodology can be employed to examine the behavior of engineering structures. These structures can be studied within the context of finite element analysis, using the identified macroscopic failure criterion.

APPENDIX A

FORMULATION OF THE OPTIMIZATION PROBLEM

The parameters:

$c \in \mathbb{R}^+$, $\phi \in \mathbb{R}^+$, $\sigma_0 \in \mathbb{R}^+$

material properties of mortar

$m \in [0,1]$, $n \in [0,1]$, $l_1 \in \mathbb{R}^+$, $l_2 \in \mathbb{R}^+$, $l_3 \in \mathbb{R}^+$, $l_4 \in \mathbb{R}^+$

geometric parameters

$\alpha \in [0, \pi/2]$

the angle defining the orientation of the principal stress system relative to the bed joints (Figure 4.2)

ξ

loading factor for biaxial tension-compression (Figure 4.5)

The variables:

$\langle \sigma_1 \rangle, \langle \sigma_2 \rangle$

principal values of macrostress tensor

$\langle\sigma\rangle$

optimized value (defines both components of macrostress tensor through the loading factor)

$X_{1,\dots,4}$, $Y_{1,\dots,4}$

normal components of microstress tensor in the material coordinate system

$XY_{1,\dots,3}$

macroscopic shear stress referred to the material coordinate system and its local correctors

$P_{1,\dots,7}$, $Q_{1,\dots,7}$

local principal microstresses

Z

Out-of-plane normal stress, which under plane stress assumption is equal to zero

Constraints:

Relations between the optimized value and the principal values of macrostress tensor

$$\langle\sigma_1\rangle = (1-\xi)\langle\sigma\rangle$$

$$\langle\sigma_2\rangle = -(1+\xi)\langle\sigma\rangle$$

Compatibility of micro - macrostress tensors:

$$X_2(1-m)+X_1m+X_3(1-m)+X_4m=2(\langle\sigma_1\rangle\cos^2\theta+\langle\sigma_2\rangle\sin^2\theta)$$

$$Y_1(1-n)+Y_2n+Y_4(1-n)+Y_3n=2(\langle\sigma_2\rangle\cos^2\theta+\langle\sigma_1\rangle\sin^2\theta)$$

$$XY_1=(\langle\sigma_2\rangle-\langle\sigma_1\rangle)\sin\theta\cos\theta$$

Note that for the dimensions of the brick units and mortar joints, as specified in Figure 3.10, the parameters $m, n, l_1, \ldots, l_4$ assume the following values

$$l_1=55\text{mm},\ l_3=40\text{mm},\ l_2=l_4=5\text{mm},\ m=\frac{l_4}{l_3+l_4}=0.111,\ n=\frac{l_2}{l_1+l_2}=0.0833$$

Equilibrium constraints:

$$(X_3-X_2)l_3=2XY_2l_1$$

$$(Y_3-Y_2)l_4=2XY_2l_2$$

$$(Y_4-Y_1)l_1=2XY_3l_3$$

$$(X_4-X_1)l_4=2XY_3l_2$$

Rankine's criterion:

$$B_{,l1}\le\sigma_0,\quad B_{,l2}\le\sigma_0$$

Mohr-Coulomb failure criterion:

$$A_{,l1}+A_{,l2}=B_{,l1}+B_{,l2},\quad \sqrt{\left(\frac{A_{,l1}-A_{,l2}}{2}\right)^2+(XY_1+A_{,l3})^2}\le\frac{|B_{,l1}-B_{,l2}|}{2}$$

$$\frac{|B_{,l1}-B_{,l2}|}{2}\le c\cos\phi+\left(\frac{B_{,l1}+B_{,l2}}{2}\right)\sin\phi$$

$$\frac{|B_{,l1}-Z|}{2}\le c\cos\phi+\left(\frac{B_{,l1}+Z}{2}\right)\sin\phi$$

$$\frac{|B_{i2}-Z|}{2} \le c\cos\phi + \left(\frac{B_{i2}+Z}{2}\right)\sin\phi$$

Objective function to be maximized:

$$\langle\sigma\rangle$$

where in above equations,

$$\mathbf{A} = \begin{bmatrix} X_1 & Y_1 & XY_1 - XY_2 \\ X_4 & Y_4 & XY_1 + XY_2 \\ X_2 & Y_2 & XY_1 - XY_3 \\ X_4 & Y_2 & XY_1 - XY_3 + XY_2 \\ X_1 & Y_2 & XY_1 - XY_3 - XY_2 \\ X_1 & Y_3 & XY_1 - XY_2 + XY_3 \\ X_4 & Y_3 & XY_1 + XY_2 + XY_3 \end{bmatrix}, \mathbf{B} = \begin{bmatrix} P_1 & Q_1 \\ P_2 & Q_2 \\ P_3 & Q_3 \\ P_4 & Q_4 \\ P_5 & Q_5 \\ P_6 & Q_6 \\ P_7 & Q_7 \end{bmatrix}$$

Note that the representation above corresponds to the stress distribution provided in Figure 4.6. The operators representing the stress field in Figure 4.4 are obtained by setting $XY_3 = 0$, $Y_4 = Y_1$ and $X_4 = X_1$. In general, the first three rows of the matrix **A** refer to stress states in segments E, G and D, respectively. The other four correspond to the stress state at the corners of segment F or H.

APPENDIX B

ON THE PLASTIC ADMISSIBILITY OF THE STRESS FIELD IN FIGURE 4.4

In the configuration shown in Figure 4.4, the stress field inside the segments D, E, and H is uniform. Consequently, the value of the failure function is constant over the entire domain, including the boundaries. In segments F and H, however, that is not the case. In what follows, it is proven that enforcing the plastic admissibility at four corners of each of these segments ensures the admissibility of stress field inside the entire domain. Here, the analysis is focused on segment H. It is noted that due to the symmetry, the status of segment F is identical to that of segment H.

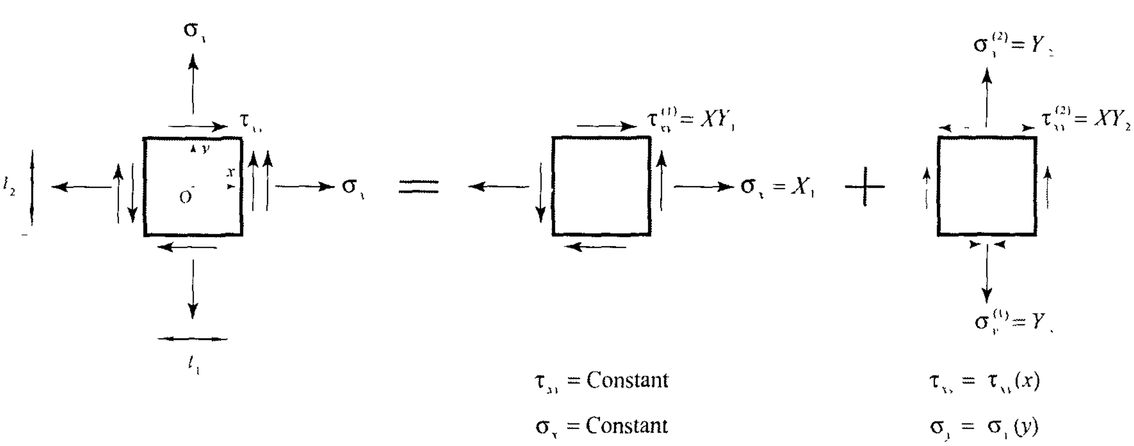

Figure B.1 – Stress state in segment H

Assuming a linear variation for τ_{xy} and σ_y (Figure B.1), one can write

$$\sigma_x = X_1 = \text{Const.};\ \sigma_y = \frac{Y_3 + Y_2}{2} + (Y_2 - Y_3)\frac{y}{l_2};\ \tau_{xy} = XY_1 + XY_2 \frac{2x}{l_1} \tag{B.1}$$

The plastic admissibility requirement reads

$$F_1 = \frac{\sigma_x + \sigma_y}{2} + \sqrt{\left(\frac{\sigma_x - \sigma_y}{2}\right)^2 + \tau_{xy}^2} - \sigma_0 \le 0 \tag{B.2}$$

$$F_2 = \left(\frac{\sigma_x + \sigma_y}{2}\right)\sin\phi + \sqrt{\left(\frac{\sigma_x - \sigma_y}{2}\right)^2 + \tau_{xy}^2} - c\cos\phi \le 0 \tag{B.3}$$

Here, F_1 represents the Rankine's cut-off criterion while F_2 stands for the Mohr-Coulomb criterion.

Substituting the stress field of Equation (B.1) into Equations (B.2) and (B.3), and taking the derivatives of the functions w.r.t. x and y, one can write

$$\frac{\partial F_1}{\partial x} = \frac{\partial F_2}{\partial x} = \frac{2XY_2\left(XY_1 + \frac{2XY_2}{l_1}x\right)}{l_1\sqrt{\frac{1}{4}\left(X - \frac{Y_3 + Y_2}{2} + \frac{Y_3 - Y_2}{l_2}y\right)^2 + \left(XY_1 + \frac{2XY_2}{l_1}x\right)^2}} \tag{B.4}$$

$$\frac{\partial F_1}{\partial y} = \frac{Y_2 - Y_3}{2l_2} - \frac{(Y_2 - Y_3)\left(X_1 - \frac{Y_3 + Y_2}{2} + \frac{Y_3 - Y_2}{l_2}y\right)}{4l_2\sqrt{\frac{1}{4}\left(X_1 - \frac{Y_3 + Y_2}{2} + \frac{Y_3 - Y_2}{l_2}y\right)^2 + \left(XY_1 + \frac{2XY_2}{l_1}x\right)^2}} \tag{B.5}$$

$$\frac{\partial F_2}{\partial y} = \left(\frac{Y_2 - Y_3}{2l_2}\right)\sin\phi - \frac{(Y_2 - Y_3)\left(X_1 - \frac{Y_3 + Y_2}{2} + \frac{Y_3 - Y_2}{l_2}y\right)}{4l_2\sqrt{\frac{1}{4}\left(X_1 - \frac{Y_3 + Y_2}{2} + \frac{Y_3 - Y_2}{l_2}y\right)^2 + \left(XY_1 + \frac{2XY_2}{l_1}x\right)^2}} \tag{B.6}$$

From Equations (B.4) – (B.6), it is evident that the first derivatives of both functions can be discontinuous inside the segment, and therefore no stationary points can be found for these functions. Note that since in general $XY_2 \neq 0$, the first derivative of both functions with respect to x becomes equal to zero at $XY_1 + \frac{2XY_2}{l_1}x = 0$, i.e. along the line $x = x_0 = -\frac{l_1}{2}\frac{XY_1}{XY_2}$. In this case, i.e. along $x = x_0$, each criterion reduces to

$$\begin{aligned} F_1(x_0,y) &= -\sigma_0 + \frac{1}{2}\left(X + \frac{Y_3+Y_2}{2} + \frac{Y_2-Y_3}{l_2}y\right) \\ &+ \frac{1}{4}\left|-2X + Y_3 + Y_2 + \frac{2(Y_2-Y_3)}{l_2}y\right| \end{aligned} \tag{B.7}$$

and

$$\begin{aligned} F_2(x_0,y) &= -c\cos\phi + \frac{1}{2}\left(X + \frac{Y_3+Y_2}{2} + \frac{Y_2-Y_3}{l_2}y\right)\sin\phi \\ &+ \frac{1}{4}\left|-2X + Y_3 + Y_2 + \frac{2(Y_2-Y_3)}{l_2}y\right| \end{aligned} \tag{B.8}$$

Both functions shown above are piece-wise continuous (have C^0 continuity). The y coordinate of the point at which the slope of the function is discontinuous can be obtained by setting the expression inside the absolute value function to zero. This gives

$$y = y_0 = -\frac{l_2}{2}\left(\frac{2X - Y_3 - Y_2}{Y_3 - Y_2}\right) \tag{B.9}$$

This point can correspond to either a relative minimum or maximum. In order to establish this, one should evaluate the value of derivative at $y \to y_0$. For Rankine criterion

$$Y_3 < Y_2 \quad \rightarrow \quad \begin{cases} \lim\limits_{x=x_0,\, y\to y_0^-} \dfrac{\partial F_1}{\partial y} = 0 \\ \lim\limits_{x=x_0,\, y\to y_0^+} \dfrac{\partial F_1}{\partial y} = \dfrac{Y_2 - Y_3}{2l_2} > 0 \end{cases}$$

$$Y_3 > Y_2 \quad \rightarrow \quad \begin{cases} \lim\limits_{x=x_0,\, y\to y_0^-} \dfrac{\partial F_1}{\partial y} = \dfrac{Y_2 - Y_3}{2l_2} < 0 \\ \lim\limits_{x=x_0,\, y\to y_0^+} \dfrac{\partial F_1}{\partial y} = 0 \end{cases}$$

which in both cases defines a local minimum.

Using the same approach, for Mohr-Coulomb one can write

$$Y_3 < Y_2 \quad \rightarrow \quad \begin{cases} \lim\limits_{x=x_0,\, y\to y_0^-} \dfrac{\partial F_2}{\partial y} = -\dfrac{Y_2 - Y_3}{2l_2}\left(1 - \sin\phi\right) < 0 \\ \lim\limits_{x=x_0,\, y\to y_0^+} \dfrac{\partial F_2}{\partial y} = +\dfrac{Y_2 - Y_3}{2l_2}\left(1 + \sin\phi\right) > 0 \end{cases}$$

$$Y_3 > Y_2 \quad \rightarrow \quad \begin{cases} \lim\limits_{x=x_0,\, y\to y_0^-} \dfrac{\partial F_2}{\partial y} = +\dfrac{Y_2 - Y_3}{2l_2}\left(1 + \sin\phi\right) < 0 \\ \lim\limits_{x=x_0,\, y\to y_0^+} \dfrac{\partial F_2}{\partial y} = -\dfrac{Y_2 - Y_3}{2l_2}\left(1 - \sin\phi\right) > 0 \end{cases}$$

Again, in either case the point proves to be a local minimum.

Other than at (x_0, y_0), there are no other relative extrema for these functions. Now, depending on the values of the stress components, the point (x_0, y_0) can be either inside or outside the segment (defined by $-\frac{l_1}{2} \le x \le \frac{l_1}{2}$ and $-\frac{l_2}{2} \le y \le \frac{l_2}{2}$). In either case, since both functions F_1 and F_2 are continuous, the absolute maximum must occur on the boundaries.

Along the boundaries, one can show using the same approach, that if either of these criteria attains an extremum, it would be a local minimum. Therefore, the absolute maximum for both Rankine or Mohr-Coulomb criterion must occur at either one of the corners of the segment.

In order to provide a graphical illustration, these two functions are plotted in Figure B.2 for two arbitrary set of parameters, i.e.

(a) $X_1 = 3$ MPa, $Y_3 = 4$ MPa, $Y_2 = 1$ MPa, $XY_1 = 1$ MPa, $XY_2 = 2$ MPa, $l_1 = 2$ m, $l_2 = 2$ m, $\sigma_0 = 6$ MPa, $c = 5$ MPa, and $\phi = 30°$

(b) $X_1 = 3$ MPa, $Y_3 = 4$ MPa, $Y_2 = 1$ MPa, $XY_1 = 2$ MPa, $XY_2 = 1$ MPa, $l_1 = 2$ m, $l_2 = 2$ m, $\sigma_0 = 6$ MPa, $c = 5$ MPa, and $\phi = 30°$

The magnitude of the stress field in the first set is chosen such that the minimum lies inside the segment, while for the second set the local minimum lies outside the segment. The plastic admissibility of the stress field in Figure 4.6 can also be addressed using the same approach.

(a)

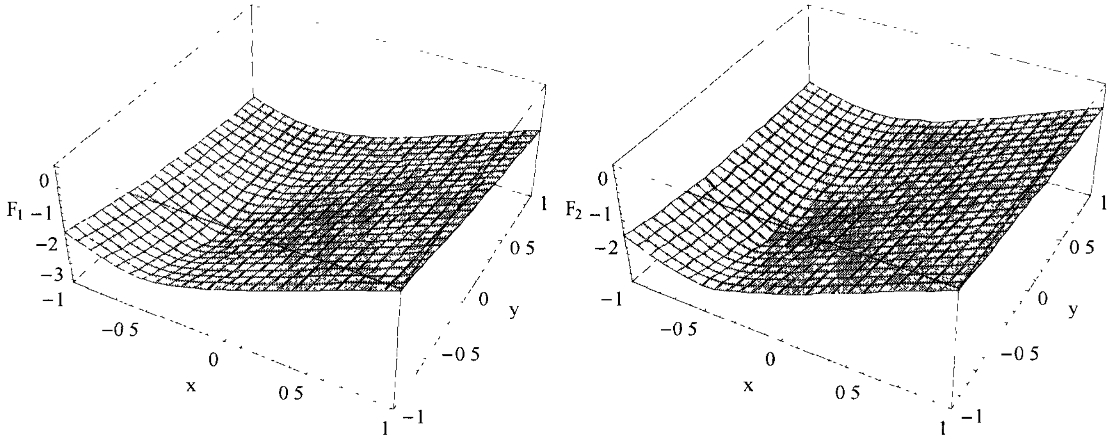

(b)

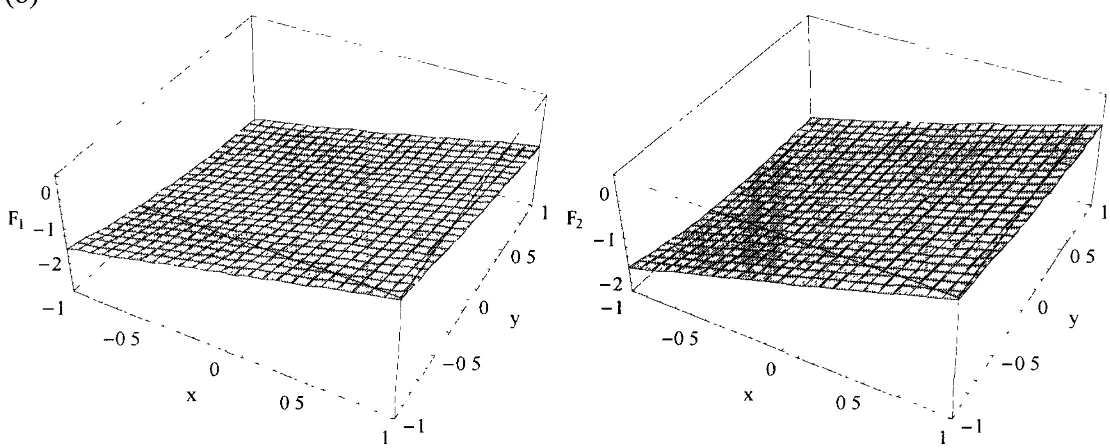

Figure B.2 – Plot of the Rankine criterion (left) and Mohr-Coulomb (right) criterion for (a) $x_0 = -l_1/2$, $y_0 = -l_2/3$; (b) $x_0 = -3l_1/2$, $y_0 = -l_2/3$

BIBLIOGRAPHY

Alpa, G., and Monetto, I. (1994). "Microstructural model for dry block masonry walls with in-plane loading." *J. Mech. Phys. Solids*, **42**, 1159–1175.

Anthoine, A. (1995). "Derivation of in-plane elastic characteristics of masonry through homogenization theory." *Int. J. Solids Struct.*, **32** (2), 137–163.

Anthoine, A. (1997). "Homogenization of periodic masonry: plane stress, generalized plane strain or 3D modelling?" *Commun. Numer. Meth. Eng.*, **13**, 319–326.

Andreaus, U. (1996). "Failure criteria for masonry panels under in-plane loading." *J. Struct. Engrg.*, **122** (1), 37–46.

Atkinson, R.H., Noland, J.L., Abrams, D.P., and McNary, S. (1985). "A deformation failure theory for stack-bond brick masonry prisms in compression." In: *Proceedings of the third North American masonry conference*, 18-1 – 18-18.

Atkinson, R.H., Amadei, B.P., Saeb, S. and Sture, S. (1989). "Response of masonry bed joints in Direct Shear." *J. Struct. Eng., ASCE,* **115** (9), 2276–2296.

Bažant, Z.P. and Jirásek, M. (2002). "Nonlocal integral formulations of plasticity and damage: Survey of progress." *J. Engng. Mech.*, 1119–1149.

Bekaert, A., and Maghous, S. (1996). "Three dimensional yield strength properties of jointed rock mass as a homogenized medium." *Mech. Coh.-Frict. Mater.*, **1**, 1–24.

Bierwirth, H., Stöckl, S., and Kupfer, H. (1993). "Triaxial tests on mortar specimens taken from bed joints." In: *Proc. 6th North American Masonry Conf.*, eds. A.A. Hamid and H.G. Harris, Drexel University, Philadelphia, Pennsylvania, USA, 995–1007.

Binda, L., Fontana, A., Frigerio, G. (1988). "Mechanical behaviour of brick masonries derived from unit and mortar characteristics." In: *Proc 8th Int. Brick/Block Masonry Conf.*, Dublin, Ireland, 205–216.

Cluni, F., and Gusella, V. (2004). "Homogenization of non-periodic masonry structures." *Int. J. Solids Struct.*, **41** (7), 1911–1923.

de Buhan, P., and Salençon, J. (1990). "Yield strength of reinforced soils as anisotropic media." In: *Mechanical Engineering Publications,* ed. J. P. Boehler, 791–803.

de Buhan, P., and Taliercio, A. (1991). "A homogenization approach to the yield strength of composite materials." *Eur. J. Mech. A/Solids*, **10** (2), 129–154.

de Buhan, P., and de Felice, G. (1997). "Homogenization approach to the ultimate strength of brick masonry." *Journ. Mech. Phys. Solids*, **45** (7), 1085–1104.

de Felice, G. (1994). "Omogeneizzazione e calcolo a rottura della muratura." *Tesi di dottorato,* Dip. Ingegneria Strutturale e Geotecnica, Roma.

Dhanasekar, M., Page, A.W., and Kleeman P.W. (1985). "The failure of brick masonry under biaxial stresses." *Proc. Instn. Civ. Engrs.*, **79** (2), 295–313.

Drysdale, R.G., and Khattab, M.M. (1995). "In-plane behavior of grouted concrete masonry under biaxial tension-compression.", *ACI Struct. J.*, **92** (6), 653–664.

Drysdale, R.G., Hamid, A.A., and Baker L.R. (1999). "Masonry structures: behavior and design." *The Masonry Society*, Boulder Colorado.

Duveau, G., Shao, J.F., and Henry, J.P. (1998). "Assessment of some failure criteria for strongly anisotropic geomaterials.", *Mech. Cohesive-Frict. Mater.*, **3**, 1–26.

Frunzio, G., Gesualdo, A. and Monaco, M. (2001). "Inelastic behaviour of mortar joints." In: *Computer methods in structural masonry - 5*, Computers & Geotechnics Ltd., Swansea, 84–92.

Gambarotta, L., and Lagomarsino, S. (1997). "Damage models for the seismic response of brick masonry shear walls. Part II: the continuum model and its applications." *Earth. Eng. and Struct. Dynamics*, **26**, 441–462.

Gocevski, V., and Pietruszczak, S. (2001). "Seismic analysis of brick masonry walls of the Beauharnois powerhouse in Quebec, Canada." In: *Computer methods in structural masonry - 5*. Computers & Geotechnics Ltd., 141–148.

Gocevski, V., Pietruszczak, S., and Ushaksaraei, R. (2002). "Seismic analysis of brick masonry walls of a power substation building." In: *Numerical Models in Geomechanics, NUMOG VIII*, AA Balkema Publ., 643–649.

Jirásek, M., and Bažant, Z.P. (2002). "Inelastic analysis of structures." *John Wiley & Sons, Ltd.*, England, 1st ed.

Karush, W. (1939). "Minima of Functions of Several Variables with Inequalities as Side Constraints". *M.Sc. Dissertation*. Dept. of Mathematics, University of Chicago, Chicago, Illinois.

Kawa, M., Pietruszczak, S., and Shieh-Beygi, B. (2007). "Limit states for brick masonry based on homogenization approach." *Int. J. Solids Struct.* (in print).

Kuhn, H.W., and Tucker, A.W. (1951). "Nonlinear programming." In: *Proc. of the Second Berkeley Symposium on Mathematical Statistics and Probability*. ed. J. Neyman, University of California Press, Berkeley and Los Angeles, 481–492.

Lotfi, H.R., and Shing, P.B. (1994). "Interface model applied to fracture of masonry structures.", *J. Struct. Engrg. ASCE*, **120**, 63–80.

Lourenço, P.B. and Rots, J.G. (1993). "On the use of micro-models for the analysis of masonry shear-walls." In: *Computer methods in structural masonry - 2*, eds. G.N. Pande and J. Middleton, Books & Journals International, Swansea, UK, 14–26.

Lourenço, P.B., Rots, J.G., and Blaauwendraad, J. (1994). "Implementation of an interface cap model for the analysis of masonry structures." In: *Computational modelling of Concrete structures*, Pineridge Press, Swansea, 123–134.

Lourenço, P.B., and Rots, J.G. (1997). "Multisurface interface model for analysis for analysis of masonry structures."*J. Eng. Mech.*, 660–668.

Lourenço, P.B., Rots, J.G., and Blaauwendraad, J. (1998). "Continuum model for masonry: parameter estimation and validation." *J. Struct. Eng., ASCE*, **124** (6), 642–652.

Lourenço, P.B., and Zucchini, A. (2001). "A homogenization model for stretcher bond Masonry." In: *Computer methods in structural masonry - 5*. Computers & Geotechnics Ltd., 60–67.

Luciano, R., and Sacco, E. (1997). "Homogenization technique and damage model for old masonry material." *Int. J. Solids Struct.*, **34** (24), 3191–3208.

Luciano, R., Sacco, E. (1998). "Variational methods for the homogenization of periodic heterogeneous media." *Europ. Journ. Mech.- A/Solids*, **17** (4), 599–617.

Lydzba, D., Pietruszczak, S. and Shao, J.F. (2003). "On anisotropy of stratified rocks: homogenization and fabric tensor approach." *Computers and Geotechnics*, **30**, 289–302.

Ma, G., Hao, H., and Lu, Y. (2001). "Homogenization of masonry using numerical simulations." *J. Eng. Mech. ASCE*, **127** (5), 421–431.

Maier, G., Nappi, A., Papa, E. (1991). "On damage and failure of brick masonry." In: *Experimental and numerical methods in earthquake engineering*, Balkema, Brussels, 223–245.

Masiani, R., and Trovalusci, P. (1996). "Cauchy and Cosserat materials as continuum models of brick masonry." *Meccanica*, **31**, 421–432.

Massart, T.J., Peerlings, R.H.J., Geers, M.G.D. and Gottcheiner, S. (2005). "Mesoscopic modeling of failure in brick masonry accounting for three-dimensional effects." *Engineering Fracture Mechanics*, **72**, 1238–1253.

Mohr, O. (1900). "Welche Umstände Bedingen die Elastizitätsgrenze und den Bruch eines Materials." *Zeitschrift des Vereines Deutscher Ingenieure*, **44**, 1524–1530.

Nayak, G.C., and Zienkiewicz, O.C. (1972). "Elastoplastic stress analysis. Generalization of various constitutive equations including stress softening." *Int. J. Num. Meth. Engng.*, **5**, 113–135.

Oliveira, D.V., and Lourenço, P.B. (2001). "An interface model for the cyclic loading of masonry." In: *Computer methods in structural masonry - 5*, Computers & Geotechnics Ltd., Swansea, 93–100.

Owen, D.R.J., and Hinton, E. (1980). "Finite elements in plasticity: theory and practice." *Pineridge Press*, Swansea.

Page, A.W. (1978). "Finite element model for masonry." *J. Struct. Div., ASCE*, **104** (8), 1267–1285.

Page, A.W. (1981). "The biaxial compressive strength of brick masonry." *Proc. Inst. Civil Engrs.*, **71** (2), 893–906.

Page, A.W. (1983). "The strength of brick masonry under biaxial tension-compression." *Int. J. Masonry Constr.*, **3** (1), 26–31.

Pande, G. N., and Sharma, K. G. (1983). "Multi-laminate model of clays – a numerical evaluation of the influence of rotation of the principal stress axes." *Int. J. Numer. Analyt. Meth. Geomech.*, **7**, 397–418.

Pande, G.N., Liang, J.X., and Middleton, J. (1989). "Equivalent elastic moduli for brick masonry." *Computers and Geotechnics*, **8**, 243–265.

Pietruszczak, S. and Niu, X. (1992). "A mathematical description of macroscopic behavior of brick masonry." *Int. J. Solids Struct.*, **29** (5), 531–546.

Pietruszczak, S., and Niu, X. (1993). "On the description of localized deformation." *Int. J. Numer. Analyt. Meth. Geomech.*, **17**, 791–805.

Pietruszczak, S. (1999). "On homogeneous and localized deformation in water-in filtrated soils."*Int. J. Damage Mech.,* **8**, 233–253.

Pietruszczak, S., and Oulapour, M. (1999). "Assessment of Dynamic Stability of Foundations on Saturated Sandy Soils." *J. Geotech. and Geoenvir. Engrg.*, **125** (7), 576–582.

Pietruszczak, S., and Mróz, Z. (2000), "Formulation of Anisotropic Failure Criteria Incorporating a Microstructure Tensor", *Computers and Geomechanics*, **26**, 105– 112.

Pietruszczak, S., and Mróz, Z. (2001), "On failure criteria for anisotropic cohesive-frictional materials." *Int. J. Numer. Anal. Meth. Geomech.*, **25**, 509–524.

Pietruszczak, S., and Ushaksaraei, R. (2003). "Description of inelastic behavior of structural masonry." *Int. J. Solids Struct.*, **40** (15), 4003–4019.

Piszczek, K., Szarliński, J. and Urbański, A. (2001). "Identification of orthotropic mechanical properties of brick masonry by an homogenization technique." In: *Computer methods in structural masonry - 5*, Computers & Geotechnics Ltd, Swansea, 52–59.

van der Pluijm, R. (1992). "Material properties of masonry and its components under tension and shear." In: *Proc. 6th Canadian Masonry Symposium*, eds. V. V. Neis, Saskatoon, Saskatchewan, Canada, 675–686.

van der Pluijm, R. (1993). "Shear behavior of bed joints." In: *Proc. 6th North American Masonry Conf.*, eds. A.A. Hamid and H.G. Harris, Drexel University, Philadelphia, Pennsylvania, USA, 125–136.

Raffard, D., Duveau, G., Shao, J.F. and Henry, J.P. (2001). "Numerical homogenization of a masonry volume." In: *Computer methods in structural masonry - 5*, Computers & Geotechnics Ltd., Swansea, 43–51.

Riddington, J.R., and Gambo, A.H. (1991). "A two stage analysis procedure for ultimate analysis of masonry shear structures." In: *Proceedings of the International Symposium on Computer Methods in Structural Masonry*, Swansea, UK, 84–92.

Samarasinghe, W., and Hendry, A.W. (1982). ''Strength of brickwork under biaxial tensile and compressive stress.'' *Proc. Br. Ceram. Soc.*, **30**, 129–139.

Sicilia, C., Pande, G.N. and Hughes, T.G. (2001). "Numerical modelling of masonry arch bridges." In: *Computer methods in structural masonry - 5*, Computers & Geotechnics Ltd, Swansea , 20–27.

Simo J.C., and Hughes, T.J.R. (1998). "Computational inelasticity." *Springer*, United States.

Shin, H.S. and Pande, G.N. (2001). "Intelligent finite elements in masonry research.", In: *Computer methods in structural masonry - 5*, Computers & Geotechnics Ltd, Swansea, 221–230.

Stankowski, T., Runesson, K., and Sture, S. (1993). "Fracture and slip of interfaces in cementitious composites. I - Characteristics." *J. Eng. Mech.*, **119** (2), 292–314.

Sulem, J., and Muhlhaus, H.B. (1997). "A continuum model for periodic two-dimensional block structures." *Mech. Coh. Frict. Mater.*, **2**, 31–46.

Suquet, P. (1987). "Elements of homogenization for inelastic solid mechanics. Homogenization techniques for composite media." In: *Lecture Notes in Physics 272*. Springer-Verlag, Berlin.

Ushaksaraei, R. and Pietruszczak, S. (2002), "Failure criterion for structural masonry based on critical plane approach." *J. Eng. Mech. ASCE*, **128** (7), 769–778.

Urbanski, A., Szarlinski, J., and Kordecki, Z. (1995). "Finite element modelling of the behaviour of masonry walls and columns by homogenization approach." In: *Computer methods in structural masonry - 3*, B & J Intern., 32–41.

Zienkiewicz, O.C. and Taylor R.L. (2000). "The Finite Element Method: Volume 1, The Basis." *Butterworth-Heinemann*, 5th ed.

Zhuge, Y., Thambiratnam, D., and Corderoy, J. (1998). "Nonlinear dynamic analysis of unreinforced masonry." *J. Struct. Engrg.*, **124** (3), 270–277.

Zucchini, A., and Lourenço, P.B. (2002). "A micro-mechanical model for the homogenization of masonry." *Int. J. Solids Struct.*, **39**, 3233–3255.